1988

A prior knowledge based optimal Wiener filtering approach to ultrasonic scattering amplitude estimation

Steven Phelps Neal
Iowa State University

Order Number 8909179

A prior knowledge based optimal Wiener filtering approach to ultrasonic scattering amplitude estimation

Neal, Steven Phelps, Ph.D.

Iowa State University, 1988

U·M·I
300 N. Zeeb Rd.
Ann Arbor, MI 48106

A prior knowledge based optimal Wiener filtering approach to ultrasonic scattering amplitude estimation

by

Steven Phelps Neal

A Dissertation Submitted to the
Graduate Faculty in Partial Fulfillment of the
Requirements for the Degree of
DOCTOR OF PHILOSOPHY

Department: Engineering Science and Mechanics
Major: Engineering Mechanics

Approved:

Signature was redacted for privacy.

In Charge of Major Work

Signature was redacted for privacy.

For the Major Department

Signature was redacted for privacy.

For the Graduate College

Iowa State University
Ames, Iowa

1988

TABLE OF CONTENTS

LIST OF SYMBOLS AND ABBREVIATIONS

ASTM	American Society for Testing and Materials
a	effective flaw radius
A	flaw scattering amplitude (far field)
A_a	effective scattering amplitude for acoustic noise
al	a subscript or superscript indicating aluminum
c_L	longitudinal wave speed
c_T	shear wave speed
c_L^f	longitudinal wave speed in a flaw
c_L^h	longitudinal wave speed in a host material
c_L^w	longitudinal wave speed in water
cc	cubic centimeters
cm	centimeters
dB	decibels
div	division
$\hat{e}_i$	incident direction unit vector
$\hat{e}_s$	scattered direction unit vector
e_a	flaw radius estimate error
e_{Im}	scattering amplitude estimation error (imaginary part)
e_{Re}	scattering amplitude estimation error (real part)
e_T	scattering amplitude estimation error total
f	frequency
f_{min}	lower limit of the measurement system bandwidth
f_{max}	upper limit of the measurement system bandwidth
F	flaw signal

F_R	reference signal
g	grams
H	measurement system response
H_a	effective measurement system response for acoustic noise
IBA	inverse Born approximation
IFT	inverse Fourier transform
k	magnitude of the wave vector
K	acoustic noise scaling factor
m	mean value (E[.])
mil	0.001 inches
MHz	megahertz (10^6 cycles/second)
n	total noise
n_a	acoustic noise
n_e	electronic noise
n_h	electronic noise associated with the estimation of H
n_r	ringing noise
n^r	total noise prior to the subtraction of n_r
ns	nanosecond (10^{-9} seconds)
NDE	nondestructive evaluation
P_a	effective propagation effects associated with acoustic noise
P_f	propagation effects associated with flaw signal measurement
P_R	propagation effects associated with reference signal measurement
ps	a subscript or superscript indicating polystyrene
Q^2	desensitization constant
R	flaw impulse response function (far field)
$\underline{R}$	acoustic reflection coefficient

ss	a subscript or superscript indicating stainless steel
S/N	signal to noise ratio
SN_K	average signal to noise ratio for noise corrupted flaw signals
t	time
T	a parameter representing a particular time
tp	a subscript or superscript indicating thermoplastic
$W(\omega)$	filter term
$W_1(\omega)$	first weighting term in the optimal Wiener filter
$W_2(\omega)$	second weighting term in the optimal Wiener filter
z	acoustic impedance
z_f	flaw acoustic impedance
z_h	host acoustic impedance
f	probability density function
λ	wavelength
λ^2	constraining term
μm	micrometer (10^{-6} meters)
μs	microsecond (10^{-6} seconds)
ζ	a parameter
ρ	correlation coefficient
$\rho_t(\tau)$	time domain correlation function
ρ_f	flaw density
ρ_h	host density
τ	time shift
σ	standard deviation
σ^2	variance
ω	circular frequency ($2\pi f$)

$\lvert\ \rvert$	magnitude
$*$	a superscript star indicates a complex conjugate
$\hat{}$	a caret over a parameter indicates an estimate of the parameter
$\bar{}$	a bar over a quantity indicates a sample average
E[ ]	expected value
Im[ ]	imaginary part
Re[ ]	real part

CHAPTER I. INTRODUCTION

Nondestructive evaluation (NDE) is an interdisciplinary field whose primary task is to measure material and flaw parameters and relate these parameters to information which is useful in an engineering context. The classical perception of NDE is that it involves the detection and characterization of flaws. In recent years, NDE has grown to include the estimation of material parameters associated with residual stress, texture, fracture toughness, plastic deformation, etc. Measurement of material and flaw parameters involves a variety of techniques including those which utilize x-rays, eddy currents, thermal waves, and ultrasonic waves.

The work reported here is associated with flaw characterization. This work is motivated from an engineering perspective by considering two fundamentally different approaches to life prediction that can be found in fatigue of materials and structures. In a simplistic sense, a "safe life" or "zero defects" fatigue life prediction approach (Coffin and Tiffany 1976) assumes that once a flaw is macroscopic, i.e., once a flaw has grown to a size which can be detected by NDE techniques, failure is imminent and the component must be taken out of service. With this approach, qualitative NDE indicating the presence or absence of a flaw provides sufficient information to determine if a component should be retired. An alternative approach, which is sometimes referred to as a "damage tolerance" approach, is based on a fracture mechanics methodology (Coffin and Tiffany 1976, Rolfe and Barsom 1977). With this approach, instead of assuming that all flawed components must be taken out of service, the

severity of the flaw is assessed and a more rational determination of the remaining life of the component is made. To implement this approach, quantitative flaw characterization is required. As a minimum input from NDE, an estimate of the size of the flaw is needed. Given an estimate of the flaw size, an engineering approach can be taken in which a worst case is assumed relative to the remaining unknown flaw related parameters (e.g., flaw type, shape, orientation, extent of closure in the case of a crack, etc.) and a conservative estimate can be made of the remaining component life. When more flaw characterization information such as flaw type and orientation can be supplied, a less conservative estimate can be made and a greater portion of the remaining life can be utilized.

A prime example of the utility of quantitative NDE can be found in the retirement-for-cause (RFC) program administered by the Air Force which addresses the utilization of the full life capacity of individual components in F100 military jet engines (Annis et al. 1981, Cooper and Forney 1981, Harris 1987). Per the initial design concepts, engine components were to be taken out of service after an analytically determined service period in which 0.1% of the components could be expected to have a fatigue crack of approximately 0.03 inches in length. The RFC approach involves utilizing quantitative NDE techniques to inspect all components after the analytically determined service period and then return components to service if 1) no flaws are found, or 2) the conservatively predicted growth-rate of a detected flaw was such that the flaw would not grow to 0.03" prior to the next planned inspection. It has been estimated that based on life cycle cost for F100 engines alone, in

excess of $1 billion could be saved over a 15 year period by utilizing RFC procedures (Harris 1987).

The motivation for quantitative flaw characterization is clear from an engineering standpoint in terms of evaluating the integrity of a component and from an economic standpoint in terms of avoiding the costs associated with premature retirement of flawed components. Currently, flaw characterization techniques vary from industrially applied techniques which determine relatively crude flaw size estimates to inverse scattering techniques being developed in the research community which have the potential for estimating a variety of flaw characteristics for much smaller flaws. Flaw characterization techniques utilize a signature from the flaw. In ultrasonics, for example, this signature can be as basic as a peak amplitude associated with the reflected energy from a flaw or the peak spacing associated with a time domain signature. The signature can also be as complicated as the total scattering characteristics of the flaw. The experimental task of determining a flaw's signature is complicated by non-flaw related effects associated with measurement systems. In ultrasonics, frequency dependent effects associated with transducers and wave propagation (e.g., diffraction and attenuation) result in a weighting of frequency components which does not reflect the true signature of the flaw. Therefore, as a preliminary step, it is desirable to remove the effects of the measurement system and utilize the true signature to estimate the flaw's characteristics. Certain techniques utilize calibration procedures to estimate flaw sizes without determining the true flaw signature. With more advanced techniques such as inverse

scattering techniques, estimating the flaw's signature by removing measurement system effects is a virtual necessity.

The flaw signature estimation problem can be more formally defined as follows. Consider a flaw detection experiment in which an ultrasonic transducer is repeatedly pulsed while being scanned over a component and the reflected signals are analyzed for indications of the presence of a flaw. For a basic plate type geometry in a region containing no flaws the measured signal will include a reflection from the front surface of the component followed by a reflection from the back surface. If a flaw is encountered, the signal from the flaw (i.e., the flaw signal) will be evident between the front and back surface reflections. The flaw signal can be described with a linear time-invariant model (Frederick and Seydel 1973; Tittmann et al. 1977) which involves the convolution of measurement system effects with the scattering characteristics of the flaw (i.e., flaw's signature), plus noise. In the time domain the model can be written in convolution integral form as (Frederick and Seydel 1973)

$$F(t) = \int_{-\infty}^{\infty} R(\tau)H(t-\tau)d\tau + n(t) \qquad (1.1)$$

where F(t) represents the measured signal, H(t) represents the measurement system impulse response function, scattering characteristics of the flaw are represented by the flaw's impulse response function, R(t), and noise is represented by n(t). By taking the Fourier transform of Eq. (1.1), the model can be written in the frequency domain as

$$F(\omega) = H(\omega)\ A(\omega) + n(\omega) \qquad (1.2)$$

where convolution becomes simple multiplication. The Fourier transform of R(t) yields the flaw's scattering amplitude, A(ω), which represents the frequency domain scattering characteristics of the flaw (i.e., the flaw's frequency domain signature).

The estimation problem involves estimating the flaw's signature by removing the measurement system response in the presence of noise. Equations (1.1) and (1.2) represent this problem equivalently as a linear estimation problem requiring a solution by filtering techniques and as an ill-posed problem requiring a regularization solution. The ill-posedness of the problem is primarily caused by the limited bandwidth of ultrasonic systems. The problem becomes apparent by considering the solution of Eq (1.2). Assuming that the measurement system response, H(ω), is known, an estimate of A(ω) could, in principle, be determined by deconvolution (i.e., frequency domain division). The resultant estimate would be given by

$$\hat{A}(\omega) = \frac{F(\omega)}{H(\omega)} \tag{1.3}$$

where $\hat{A}(\omega)$ indicates an estimate of A(ω). As H(ω) goes to zero near the limits of the system bandwidth, the deconvolution becomes unstable. As a consequence of this instability, small changes in the measured data, due to the presence of noise, for example, can result in large changes in the estimated flaw signature. This behavior causes the flaw signature estimation problem to be ill-posed (Lee et al. 1984, Clark et al. 1986).

A common method of stabilizing the problem involves a constrained deconvolution which yields a scattering amplitude estimate of the form

$$\hat{A}(\omega) = \frac{F(\omega)\, H^{*}(\omega)}{|H(\omega)|^{2} + \lambda^{2}(\omega)} \tag{1.4}$$

where $H^{*}(\omega)$ is the complex conjugate of $H(\omega)$ and $|H(\omega)|$ is the magnitude of $H(\omega)$. This constrained deconvolution approach can be derived from a filtering approach or from a regularization approach. Depending on the approach taken, $\lambda^{2}(\omega)$ can be said to stabilize the solution, desensitize the deconvolution, or regularize the problem.

The choice of $\lambda^{2}(\omega)$ has been the focus of a great deal of study (Whalen 1971, Tikhonov and Arsenin 1977, Davies 1982, Clark et al. 1986). In general, the method used to choose $\lambda^{2}(\omega)$ is dependent on the criterion used to establish an optimal estimate and on the availability and use of prior information about the noise and the parameter to be estimated. In many cases, a constant value (i.e., a frequency independent value) is chosen in a non-optimal manner based on the satisfactory results from a limited number of estimates. This is especially common in cases where noise statistics are not known or in a research environment where a limited number of estimation problems can be considered. In the case of scattering amplitude estimation in a research environment, the most widely reported scattering amplitude estimation approach involves use of Eq. (1.4) with $\lambda^{2}(\omega)$ chosen to be a non-optimally chosen constant (Murakami et al. 1978, Elsley et al. 1980, Thompson et al. 1986). The primary deficiency of this approach is its inability to filter out noise.

An improved approach for determining $\lambda^{2}(\omega)$ results in an optimal Wiener filter. This approach can also be said to yield an optimal regularized solution of Eq. (1.1) (Tikhonov and Arsenin, 1977). As

outlined explicitly in terms of the scattering amplitude estimation problem by Elsley et al. (1980), $A(\omega)$ and $n(\omega)$ are assumed to be uncorrelated, Gaussian random variables with zero mean and known variance. The resultant optimal choice for $\lambda^2(\omega)$ is given by the ratio of the noise variance to the scattering amplitude variance. In addition to its optimal base, this approach is appealing due to its ability to filter out noise. It is the purpose of the work presented in this dissertation is to evaluate the application of the optimal Wiener filter to the ultrasonic scattering amplitude estimation problem. This work is reported in four stages: 1) derivation of the optimal Wiener filter (Chapter III); 2) experimental procedures involving the measurement of flaw and noise signals (Chapter IV); 3) analysis of the random variables involved in the estimation problem (Chapter V); and 4) evaluation of the strengths and weaknesses of the filter in determining scattering amplitude estimates from noise-corrupted flaw signals (Chapter VI). The dissertation is concluded with a summary and discussion of the results as a whole (Chapter VII).

CHAPTER II. BACKGROUND: SCATTERING AMPLITUDE ESTIMATION

The intent of this chapter it to provide background information and to establish the starting point for the work presented in the remaining chapters. Within this chapter, flaw signatures are discussed, deterministic and stochastic models describing the estimation problem are formulated, estimation problems are discussed, and flaw signature estimation techniques are reviewed.

Flaw Signature Description

Formal description

A scattering geometry involving a flaw in an otherwise isotropic, homogeneous, and unbounded solid is depicted schematically in Fig. 2.1.a. Consider the interrogation of the flaw by a unit amplitude, longitudinally polarized delta function plane wave. The displacement field associated with the incident plane wave can be written as

$$u_i = e^{j(\omega t - k\hat{e}_i \cdot \vec{r})} \tag{2.1}$$

where $\hat{e}_i$ is a unit vector in the incident direction, ω equals the circular frequency ($2\pi f$), c equals the longitudinal wave speed, and k is the magnitude of the wave vector (ω/c). Under these idealized assumptions and in the far field (at large r), spherically spreading waves resulting from scattering at the flaw can be described by the flaw's scattering amplitude

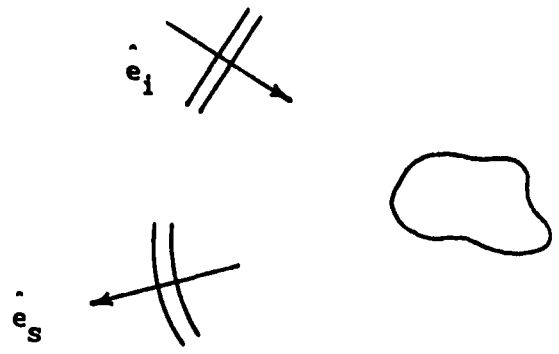

Figure 2.1. Scattering geometry

(i.e., the flaw's frequency domain signature). The scattered field can be written as (Gubernatis et al. 1977, Thompson and Gray 1983, Rose 1984)

$$u_s = \frac{A(\hat{e}_i,\hat{e}_s,\omega)}{r} \; e^{j(\omega t - k\hat{e}_s\cdot\vec{r})} \tag{2.2}$$

where $\hat{e}_s$ is a unit vector in the scattered direction and the far field scattering amplitude is given by $A(\hat{e}_i,\hat{e}_s,\omega)$. In the time domain, the incident field can be written as

$$u_i = \delta(t-\hat{e}_i\cdot\vec{r}/c) \tag{2.3}$$

and the scattered field is given by

$$u_s = \frac{R(\hat{e}_i,\hat{e}_s,t-r/c)}{r} \tag{2.4}$$

where $R(\hat{e}_i, \hat{e}_s, t-r/c)$ is the far field impulse response function of the flaw (i.e., the flaw's time domain signature).

The impulse response function and scattering amplitude represent a Fourier transform pair (Rose 1984). That is, R(t) can be determined from $A(\omega)$ by an inverse Fourier transform (IFT) as given by

$$R(t) = \frac{1}{2\pi} \int_{-\infty}^{\infty} e^{-i\omega t} A(\omega)\, d\omega \qquad (2.5)$$

and the scattering amplitude can be determined from the impulse response function by a forward Fourier transform. Therefore, frequency variations in the scattering amplitude are reflected in the shape of the impulse response function, and temporal variations in the impulse response function can be used to interpret frequency variations in the scattering amplitude.

The point to be emphasized relative to this ideal scattering problem is that the scattered field is equal to the flaw's signature only under idealized assumptions. That is, the scattered field is a true representation of the flaw's signature only for 1) an incident field which contains all frequency components equally weighted and which does not diffract while propagating, and 2) scattering in a solid which does not introduce any frequency dependent propagation effects. With these assumptions, all frequency variations which exist in the scattered field have been introduced by scattering at the flaw.

Given a flaw's physical characteristics and a knowledge of the incident wave field, the problem of determining the scattered wave field (in essence, the problem of determining the flaw's scattering amplitude or

impulse response function) is known as the forward scattering problem. In terms of the flaw signature estimation problem, forward solutions are particularly important in that they make the use of model based estimation techniques possible, they allow estimation techniques to be studied using simulated flaw signals, and they make it possible to establish a "right answer" against which estimates can be compared.

Exact forward scattering solutions have been determined for a limited number of cases. In particular, Ying and Truell (1956) solved the problem of scattering by a spherical object, and White (1958) determined a solution for scattering by a cylindrical object. A number of approximate solutions have also been determined. The Born approximation (discussed later in this section) leads to an analytical solution for weak scattering flaws (Gubernatis et al. 1977). Approximate solutions have been determined at long wave lengths (i.e., for wave lengths which are much larger than the scattering object) for a number of simple geometries (Eshelby 1957, Domany et al. 1978, Teitel 1978, Richardson 1978, Gubernatis 1979). At high frequencies (i.e., frequencies at which the wavelength is much smaller than the scattering object), approximate solutions have been determined using the Kirchhoff approximation (Adler and Achenbach 1980, Achenbach et al. 1982) and using diffracted ray methods (Achenbach and Gautesen 1977, Gautesen et al. 1978, Achenbach et al. 1979, Achenbach et al. 1982). Numerical solutions have been proposed for the solution of the general forward scattering problem, and solutions have been determined for a number of flaw shapes. A scattering matrix approach has been used to determine forward scattering solutions for cylindrical cavities (Varadan 1978), spheroidal cavities (Varadan and

Varadan 1979, Lakhtakia et al. 1985), penny shaped cracks and strips (Varadan 1979) and fluid filled non-planar cracks (Varadan 1979). Opsal and Visscher (1985) solved the forward problem numerically for spheres, circular cracks, and oblate spheroids using the method of optimal truncation (MOOT). Visscher (1981) utilized MOOT to determine the scattering from a penny-shaped crack. Varadan (1978) reported the application of a scattering matrix approach to scattering by elliptical cylinders. It is to be noted that the utility of numerical solutions in terms of the flaw signature estimation problem is a function of the computational time and cost associated with calculating a solution.

The Born approximation (Gubernatis et al. 1977) is particularly useful for discussing scattering amplitude characteristics. The Born approximation allows solution of the integral form of the wave equation by assuming that the exact displacement fields within the flaw are approximately equal to the incident displacement fields. This assumption is reasonable when the acoustic impedance (Kolsky 1963, Krautkramer and Krautkramer 1977) of a flaw, $z_f=\rho_f c_f^L$ (ρ_f=flaw density and c_f^L=longitudinal wave speed in the flaw), is nearly equal to the acoustic impedance of the host, $z_h=\rho_h c_h^L$ (ρ_h=host density and c_h^L=longitudinal wave speed in the host). The acoustic reflection coefficient (Kolsky 1963, Krautkramer and Krautkramer 1977), $\underline{R}$, can be defined as

$$\underline{R} = \frac{\rho_h c_h^L - \rho_f c_f^L}{\rho_h c_h^L + \rho_f c_f^L} = \frac{z_h - z_f}{z_h + z_f} \qquad (2.6)$$

For weak scatterers, $\underline{R}$ is small and results in only a weak scattering of

the incident waves. A flaw which satisfies the Born approximation is referred to as a Born scatterer.

In the Born approximation, the scattering amplitude for a flaw with center of inversion symmetry can be written as (Gubernatis et al. 1977)

$$A(\omega) \sim -\underline{R}\, k^2 a^3 \, \frac{\sin(2ka) - 2ka(\cos(2ka))}{(2ka)^3} \tag{2.7}$$

where a is the effective flaw radius. The simplicity of Eq. (2.7) makes it a good vehicle for identifying a number of features of scattering amplitudes which will be important in the analysis of $A(\omega)$ as a random variable in Chapter V.

Equation (2.7) demonstrates that the nature of $A(\omega)$ is controlled by ka where $k=\omega/c$. In effect, ka, which can be written $2\pi(a/\lambda)$, reflects the relationship between wavelength, λ, and a characteristic dimension, a, of the flaw (e.g., the radius for a sphere). Considering $A(\omega)$ in limiting ka ranges demonstrates the dependence of $A(\omega)$ on the flaw size/wavelength relationship. At low frequencies where the wavelength is much larger than the flaw size (i.e., $\lambda \gg a$), $ka \ll 1$. This limiting case will be referred to as the long wavelength limit. By utilizing the series expansions for sin(2ka) and cos(2ka), Eq. (2.7) reduces to

$$A(\omega) \sim \underline{R}\, k^2 a^3 \tag{2.8}$$

in the long wavelength limit. Here, the scattering amplitude is proportional to frequency squared and to the cube of the radius (the volume) of the scatterer. While based on the Born approximation here, this is a universal result for volumetric scatterers at long wavelengths (Richardson 1984, Kino 1987). In this limit, the nature of $A(\omega)$ can be

summarized as follows: 1) the sign of $A(\omega)$ is determined by $\underline{R}$; 2) at a given frequency (i.e., at a given k), $A(\omega)$ is proportional to a^3; and 3) for a given flaw size, $A(\omega)$ is proportional to ω^2. In all cases where $z_f > z_h$, $\underline{R}$ will be positive, and $A(\omega)$ will rise from zero frequency as ω^2. In all cases where $z_f > z_h$, $\underline{R}$ will be negative, and $A(\omega)$ will be negative and will decrease as ω^2.

At high frequencies where the wavelength is much smaller than the flaw size (i.e., $\lambda \ll a$), Eq. (2.7) reduces to

$$A(\omega) \sim \underline{R}\, k^2 a \cos(2ka) \qquad (2.9)$$

Here, the sign of $A(\omega)$ is not controlled simply by $\underline{R}$. At high frequencies, $A(\omega)$ oscillates about zero at a given frequency for varying flaw sizes.

Graphical description - examples of weak (Born) and strong scatterers

Characteristic scattering amplitude features just described can be demonstrated graphically. First, consider the flaw signature for a Born scatterer. The impulse response function for a 300μm radius Born scatterer is shown in Fig. 2.2.a. The magnitude, $|A(\omega)|$, and real part, $\mathrm{Re}[A(\omega)]$, of the corresponding scattering amplitude are shown in solid lines in Fig. 2.2.b and Fig. 2.2.c, respectively. Shown in dashed line in Fig. 2.2.c is $\mathrm{Re}[A(\omega)]$ for a 200μm radius Born scatterer. The scattering amplitudes were calculated using Eq. (2.7) and were then normalized to 1.0 since only the shape of the curves is important here. The host material was taken to be stainless steel (ρ_{ss}=7.9g/cc, c_{ss}^L=0.58cm/μs, and c_{ss}^T=0.31cm/μs, where c_{ss}^T is the shear wave speed in stainless steel) and the flaw was assumed to have a smaller acoustic impedance than that of the

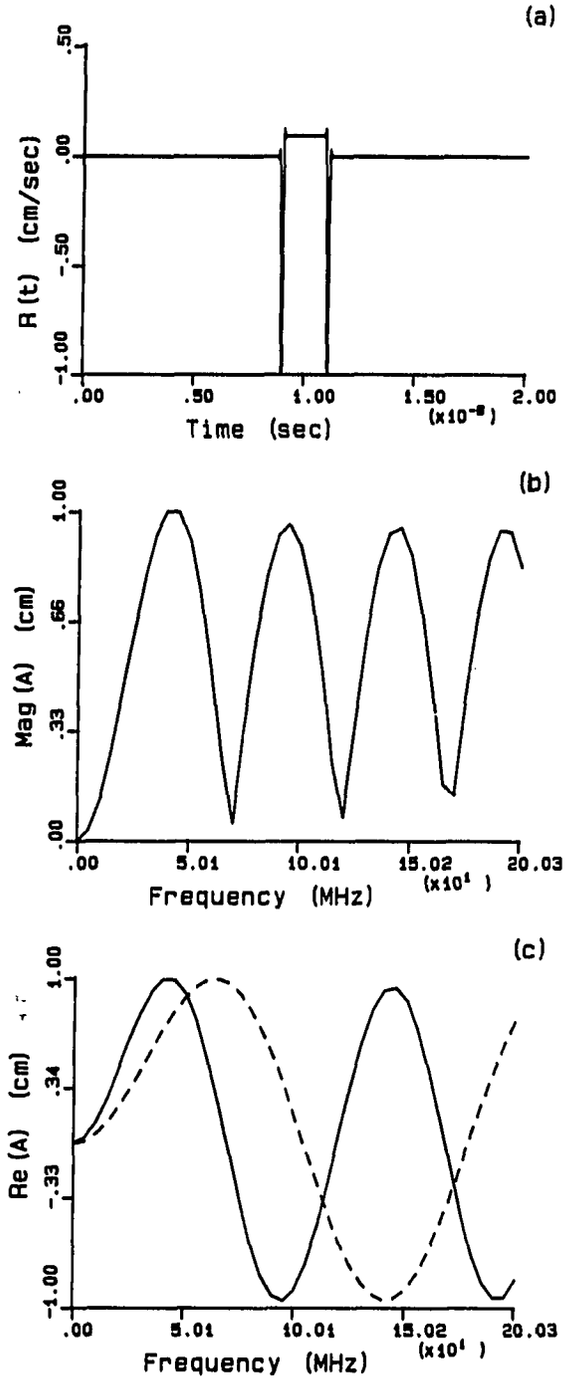

Figure 2.2. Born scatterer. a) R(t) for 300μm radius; b) $|A(\omega)|$ for 300μm radius; c) Re[$A(\omega)$] for 300μm radius (solid) and 200μm radius (dashed)

host. The impulse response function was determined by taking the IFT of the scattering amplitude. The result of the IFT is an impulse response function centered about t=0.0. The impulse response function shown in Fig. 2.2.a has been shifted such that it is centered about t=1.0μs.

For a Born scatterer, the scattered wave field is dominated by reflections at the front and back surface of the flaw (Rose and Richardson 1982). These reflections are evident in the impulse response function shown in Fig. 2.2.a. Note the symmetry associated with the impulse response function for the Born scatterer. The magnitude and real part of the scattering amplitude show the oscillatory nature represented by Eq. (2.7). The oscillations are due to the frequency dependent interference pattern caused by the interaction of the front and back surface delta function reflections in the impulse response function (Thompson 1983, Bracewell 1965). That is, at wave lengths corresponding to some frequencies, the spacing between the two delta function is such that their components at those frequencies constructively interfere; conversely, at other wave lengths, the delta functions destructively interfere.

Also shown in Fig. 2.2.c is Re[A(ω)] for a smaller flaw with a=200μm. As predicted by Eq. (2.8), the scattering amplitudes of both spheres rise from zero frequency with the same sign. In a sense, the two scattering amplitudes are initially "in phase" at low frequencies. At higher frequencies both oscillate about zero as predicted by Eq. (2.9). Here, it could be said that the two scattering amplitudes are "out of phase". Also note that variations with flaw size are much larger at high frequencies than at low frequencies.

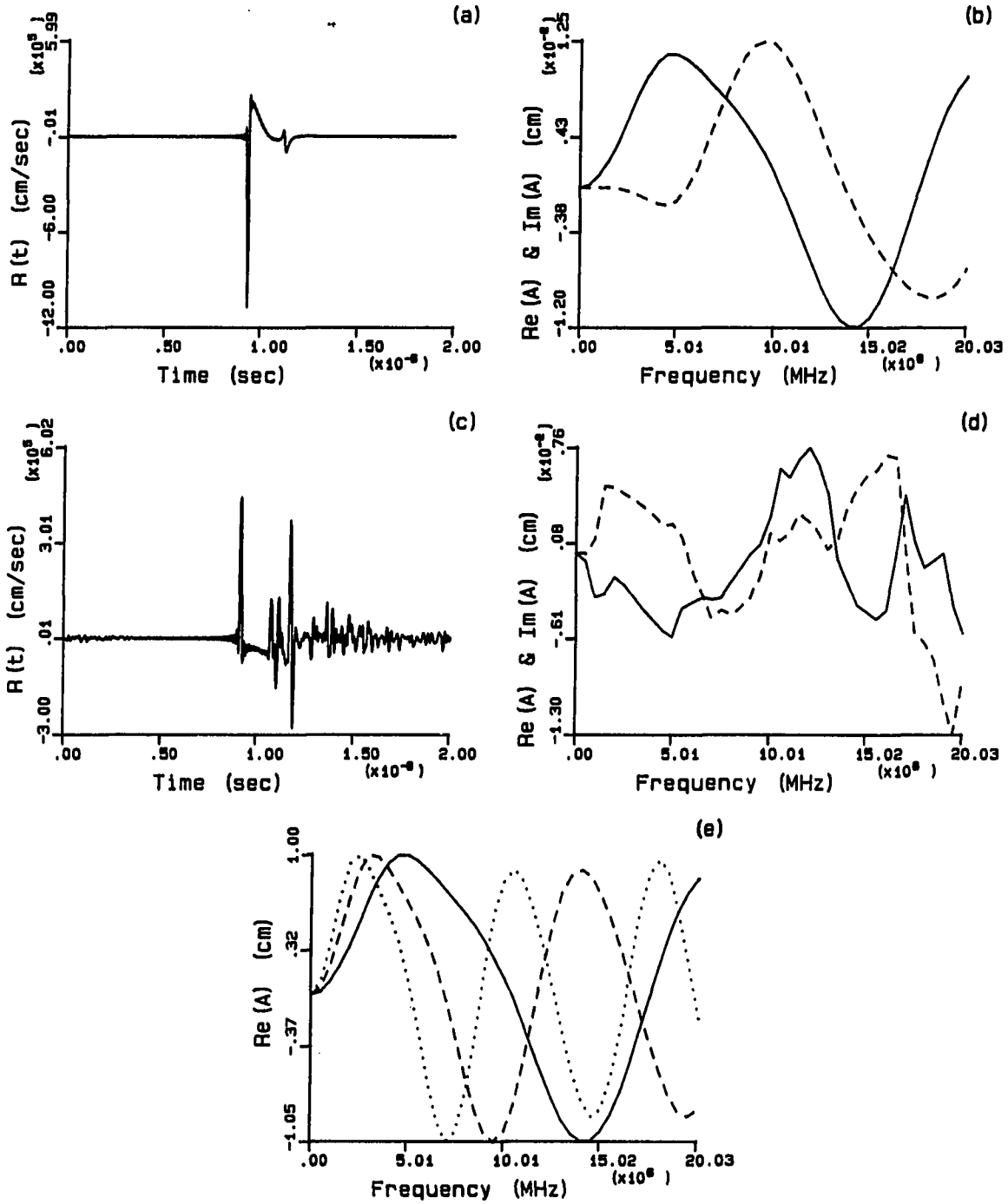

Figure 2.3. Strong scatterers. a) and b) 200μm radius spherical void in stainless steel; c) and d) 120μm radius tin-solder sphere in thermoplastic; e) 200μm, 300μm, and 400μm radius voids in stainless steel

The work of Ying and Truell (1956) was used to calculate scattering amplitudes for two strong scatterers shown in Fig. 2.3. Strong scatterers are flaws whose acoustic impedance varies significantly from the acoustic impedance of the host. In all cases, Re[A(ω)] is shown in solid lines and Im[A(ω)] is shown in dashed line. Corresponding impulse response functions were determined by taking the IFT of the scattering amplitude. Figures 2.3.a and 2.3.b represent the simulation of a 200μm radius spherical void in stainless steel. Figures 2.3.c and 2.3.d are for a 120μm radius tin-solder sphere (ρ_{ts}=8,41g/cc, c^L_{ts}=0.301cm/μs, and c^T_{ts}=0.145cm/μs (Thompson and Gray 1983)) in thermoplastic (ρ_{tp}=1.18g/cc, c^L_{tp}=0.272cm/μs, and c^T_{tp}=0.135cm/μs). These flaw/host combinations are used in later chapters.

In general, for strong scatterers, the only obviously identifiable feature in the impulse response function is the front surface reflection. The origin of the secondary peaks is related to the formation of surface waves for voids and surface waves and internal reflections for inclusions (such as the tin-solder sphere) (Chou et al. 1980, Thompson and Gray 1982, Thompson and Thompson 1985a). Regardless of the origin of the secondary peaks, the interaction between the peaks causes oscillations in the scattering amplitude for the strong scatterers in a similar fashion to the weak scattering case. In particular, for the tin-solder sphere in thermoplastic, multiple internal reflections and surface waves result in an impulse response with many secondary peaks. The interactions of these multiple peaks cause the noise-like appearance of the scattering amplitude. This case will be utilized in later chapters to study estimation of scattering amplitudes with noise-like features.

Notice that for the void in stainless steel, the reflection coefficient (Eq. (2.6)) is positive and Re[A(ω)] starts out positive. For the tin-solder sphere in thermoplastic, the reflection coefficient is negative and Re[A(ω)] starts out negative. This behavior is as expected based on Eq. (2.8). Also notice that in each case Re[A(ω)] and Im[A(ω)] start out with opposite sign. The generality of this observation is not known.

Finally, the observations based on Equations (2.8) and (2.9) are demonstrated for the void in stainless steel in Fig. 2.3.e. Here, Re[A(ω)] is shown for void sizes of 200μm radius (solid), 300μm radius (dashed), and 400μm radius (dotted). The scattering amplitudes are normalized to 1.0. This figure demonstrates that the scattering amplitudes for strong scatterers start out "in phase" and with a non-oscillatory nature at low frequencies and then become oscillatory and "out of phase" at higher frequencies.

Deterministic Models

Noise-free models

The models discussed in this section are deterministic models which represent the "outcome" of a given flaw interrogation experiment. It is to be noted at the outset that models are stated here with only the frequency dependence explicitly given. The dependence of the models on all other factors is implicit. For example, the dependence of flaw signatures on the incident and scattered directions (see Fig. 2.1 and Equations (2.1)-(2.4)) and the dependence of the measurement system

response and acoustic noise on the incident and scattering directions and on the spatial relationships between the transducer(s), host, and flaw is implicit.

The ideal scattering problem can be modeled by a linear time-invariant system (Frederick and Seydel 1973) consisting of an input (the incident wave field), a system (the flaw), and output (the scattered field). In the time domain, the model can be stated as

$$Y(t) = R(t)*X(t) \tag{2.10}$$

where X(t) represents the incident field, R(t) is the impulse response function of the flaw, Y(t) represents the measured result, and * denotes the convolution operation (see Eq. (1.1)). In the frequency domain, the model can be written as

$$Y(\omega) = A(\omega)\ X(\omega) \tag{2.11}$$

where $Y(\omega)$ and $X(\omega)$ are the Fourier transform of Y(t) and X(t), respectively, and the Fourier transform of R(t) is the flaw's scattering amplitude, $A(\omega)$.

Equation (2.11) will be used to draw out three points. First, for the idealized case where $X(\omega)$ is a frequency independent constant, Eq. (2.11) reaffirms that all of the frequency variations in the scattered field, $F(\omega)$, are due to the scattering characteristics of the flaw as represented by its scattering amplitude, $A(\omega)$. Second, it demonstrates that if the incident field has unit amplitude, then the scattered field is actually equal to the scattering amplitude. Finally, Eq. (2.11) shows that the problem of estimating a flaw's signature is a system identification problem. That is, given knowledge of the incident wave

field, $X(\omega)$, and knowledge of the scattered wave field, $Y(\omega)$, estimate the system operator, $A(\omega)$.

In practice, ultrasonic measurement systems introduce frequency dependent variations into the problem which are not related to scattering at the flaw. For example, typical piston source transducers and associated electronics generate waves which are bandlimited, have non-flat frequency response within the bandwidth, and which attenuate and diffract while propagating. A more realistic model of the output of a flaw experiment can be written as (Frederick and Seydel 1973, Fitting and Adler 1981, Tittmann et al. 1977)

$$F(t) = X(t)*E_1(t)*T_1(t)*P_1(t)*R(t)*P_2(t)*T_2(t)*E_2(t) \qquad (2.12)$$

where the output signal (i.e., the measured signal) is denoted $F(t)$, the input signal, $X(t)$, represents the electrical excitation sent to the sending transducer, and $R(t)$ represents the flaw's impulse response function. The remaining terms represent components of the measurement system. The subscript 1 indicates the period prior to scattering at the flaw (i.e., the sending step where the waves travel in the incident direction, $\hat{e}_i$, (see Fig. 2.1)), and 2 indicates the period following scattering at the flaw (i.e., the receiving step where the waves travel in the scattered direction, $\hat{e}_s$). All electronic effects including those associated with the pulser/receiver and digitizing device are represented by $E(t)$. The response of the transducer(s) is given by $T(t)$. Propagation effects such as beam divergence due to diffraction, attenuation primarily due to scattering at grain boundaries, dislocations, porosity, etc.,

within the host material, and interfacial effects such as reflection and refraction at the front surface of the part are represented by P(t).

Equation (2.12) can be simplified in two steps by combining the non-flaw responses. The model is first rewritten in the time domain as

$$F(t) = M(t)*P_f(t)*R(t) \tag{2.13}$$

and in the frequency domain as

$$F(\omega) = M(\omega)\ P_f(\omega)\ A(\omega) \tag{2.14}$$

where $M(\omega)=X(\omega)E_1(\omega)T_1(\omega)T_2(\omega)E_2(\omega)$, $P_f(\omega)=P_1(\omega)P_2(\omega)$, and the subscript, f, indicates association with waves scattered at the flaw. Thus, $M(\omega)$ represents all electronic and transducer related system effects, and $P(\omega)$ represents all propagation effects (Frederick and Seydel 1973, Tittman et al. 1977). The non-flaw contributions can be further combined to yield

$$F(t) = H(t)*R(t) \tag{2.15}$$

in the time domain and

$$F(\omega) = H(\omega)\ A(\omega) \tag{2.16}$$

in the frequency domain where $H(\omega)=M(\omega)P_f(\omega)$. All non-flaw related effects including the input signal and all measurement system components are now represented by $H(\omega)$.

Noise-corrupted models

Noise will be classified as either acoustic noise, n_a, or electronic noise, n_e. Acoustic noise results from non-flaw related scattering or reflection of the incident waves. Possible acoustic noise sources include

scattering from internal sources such as porosity, grain boundaries, dislocations, impurities within the grain structure, weld interfaces, and adjacent surfaces within the flawed component. Acoustic noise is a convolution type noise, that is, it involves the convolution of measurement system effects with a noise related operator (Fertig and Richardson 1983). Therefore, acoustic noise can be modeled in the time domain as

$$n_a(t) = M(t)*P_a(t)*R_a(t) = H_a(t)*R_a(t) \tag{2.17}$$

and in the frequency domain as

$$n_a(\omega) = M(\omega)\ P_a(\omega)\ A_a(\omega) = H_a(\omega)\ A_a(\omega) \tag{2.18}$$

where $M(t)$ and $M(\omega)$ are as defined relative to Equations (2.13) and (2.14), P_a is an effective propagation effects term and $R_a(t)$ and $A_a(\omega)$ represent an effective impulse response function and an effective scattering amplitude, respectively, associated with the dominate source of the acoustic noise. These terms are said to be "effective" since $P_a(\omega)$ and $A_a(\omega)$ are average or effective operators associated with scattering at a distribution of scattering sites (e.g., scattering from a large number of grains) rather than scattering from a single target (Fertig and Richardson 1983).

With the addition of noise, the time domain model for the flaw signal can be written as

$$F(t) = H(t)*R(t) + n_a(t) + n_e(t) \tag{2.19}$$

and the frequency domain model can be written as

$$F(\omega) = H(\omega)\, A(\omega) + n_a(\omega) + n_e(\omega) \tag{2.20}$$

By combining the noise terms, the final form of the model can be written in the time domain as

$$F(t) = H(t)*R(t) + n(t) \tag{2.21}$$

where $n(t)=n_a(t)+n_e(t)$ and in the frequency domain as

$$F(\omega) = H(\omega)\, A(\omega) + n(\omega) \tag{2.22}$$

where $n(\omega)=n_a(\omega)+n_e(\omega)$.

The flaw signal model can be written in a form which explicitly represents acoustic noise as convolution noise. Combining Equations (2.18) and (2.20), the model can be written as

$$F(\omega) = H(\omega)\, A(\omega) + H_a(\omega)\, A_a(\omega) + n_e(\omega) \tag{2.23}$$

If it is assumed that $H_a(\omega)=H(\omega)$, $H(\omega)$ can be factored out and the model can be written as

$$F(\omega) = H(\omega)\, [A(\omega) + A_a(\omega)] + n_e(\omega) \tag{2.24}$$

Note that assuming $H_a(\omega)=H(\omega)$ is equivalent to assuming $P_a(\omega)=P_f(\omega)$. In principle, since $P_a(\omega)$ must take into account both scattering over a distribution of scattering sites and multiple scattering, it is more complicated (and more difficult to determine) than $P_f(\omega)$. However, as a first approximation, it could be assumed that $P_a(\omega)=P_f(\omega)$ provided first that acoustic noise which lie within the same time window as the signal from the flaw comes primarily from scattering at sites closely surrounding the flaw, and second that contributions due to multiple scattering are negligible.

Stochastic Models

Random processes and random variables

In this section, conceptual experiments are used to discuss the components of the flaw signal model (see Eq. 2.19) in a random processes context. The components of the flaw signal will be dealt with individually by utilizing three conceptual experiments involving no material samples (electronic noise), stainless steel plates containing no flaws (acoustic noise), and homogeneous plates containing flaws (flaw scattering). These concepts are then combined to establich a stochastic model for a noise-corrupted flaw signal.

Consider a conceptual experiment involving the measurement of a family of electronic noise signals. As a part of this conceptual experiment, assume that a large number of nominally identical ultrasonic systems are set up in a pulse-echo mode with no material sample present. The systems are switched on simultaneously and the output signal for each system is recorded as a function of time. With no sample present, there will be no reflected ultrasonic signal and the measured signals will involve only electronic noise. As a whole, the signals represent a family or, as the number of systems goes to infinity, an ensemble of electronic noise signals.

Following the notational concept of Papoulis (1965), $n_e(t,\zeta)$ can be used to denote the random process associated with electronic noise (Assefi 1979). Here, ζ is a parameter which represents all possible outcomes (equivalently, all possible samples or signals) associated with the random

process. Thus, ζ_i indicates the i^{th} outcome. Using this notation, $n_e(t,\zeta)$ can represent four things: 1) for a particular outcome, ζ_i, $n_e(t,\zeta_i)$ represents the electronic noise signal as a function of time associated with the i^{th} ultrasonic system; 2) at a particular time, t_i, $n_e(t_i,\zeta)$ is a random variable whose amplitude varies over the family of electronic noise signal; 3) at a particular time and for a particular signal, $n_e(t_i,\zeta_j)$ is simply a number which represents one outcome or sample of the random variable $n_e(t_i,\zeta)$; and 4) the general notation, $n_e(t,\zeta)$, represents a family or ensemble of electronic noise signals.

Continuing the conceptual experiment, consider the measurement of acoustic noise, specifically, acoustic noise due to grain scattering. Assume that a large number of nominally similar metallic plates are available and that one plate is placed in each system. Also, assume that 1) each plate is interrogated in a pulse-echo mode at normal incidence; 2) electronic noise is negligible due to averaging; and 3) the backscattered signal from each plate is recorded with t=0 taken to be the center of the plate. Between the front and back surface reflection for each signal, the signal will be made up of acoustic noise caused by the superposition of backscattered waves from a large number of grains. The acoustic noise signals form a family of signals as represented by $n_a(t,\zeta)$. In analogy with the notation for electronic noise, $n_a(t,\zeta_i)$ represents a single acoustic noise signal, $n_a(t_i,\zeta)$ is a random variable, $n_a(t_i,\zeta_j)$ represents one outcome of the random variable, and $n_a(t,\zeta)$ represents an ensemble of acoustic noise signals.

Finally, consider a similar conceptual experiment involving homogeneous plates (e.g., glass or plastic plates) each with thickness, d,

and each containing a spherical void with the centroid of the void at the center of the plate. The void radius is assumed to vary randomly from plate to plate. In analogy with the previous example, each flaw is to be interrogated at normal incidence, electronic noise is assumed to be negligible, and the backscattered signals are to be recorded with t=0 taken to be at the centroid of each flaw. Since the plates are assumed to be homogeneous, there will be no acoustic noise and each backscattered signal will be made up of a front surface reflection, the scattered signal from the flaw, and a back surface reflection (plus multiple reflections). The flaw signals represent a family of signals resulting from the interrogation of a family of flaws. At a particular time, t_i, $R(t_i,\zeta)$ is a random variable representing the variations in flaw signatures associated with the family of flaws.

Models

Stochastic simply means random; therefore, a stochastic model is a model which involves random variables. Utilizing the conceptual experiment concepts, the measurement of a family of noise-corrupted flaw signals resulting from the interrogation of a large number of metallic plates with a spherical void at the center of each plate could be described by a model written as

$$F(t,\zeta) = H(t)*R(t,\zeta) + n_a(t,\zeta) + n_e(t,\zeta) \qquad (2.25)$$

where $F(t,\zeta)$ represents an ensemble of noise-corrupted flaw signals. For a particular outcome, ζ_i, associated with the interrogation of the i^{th} flaw, Eq. (2.25) is equivalent to the deterministic model given by Eq. (2.19).

Analogous notation can be used to represent the random processes, random variables, and stochastic models in the frequency domain. In the frequency domain, Eq. (2.25) can be written as

$$F(\omega, \zeta) = H(\omega)\, A(\omega, \zeta) + n_a(\omega, \zeta) + n_e(\omega, \zeta) \tag{2.27}$$

For a particular outcome, ζ_i, associated with the interrogation of the i^{th} flaw, Eq. (2.27) is equivalent to the deterministic model given by Eq. (2.20). At a particular frequency, ω_i, Eq. (2.27) becomes a stochastic model involving random variables and can be written as

$$F(\omega_i, \zeta) = H(\omega_i)\, A(\omega_i, \zeta) + n_a(\omega_i, \zeta) + n_e(\omega_i, \zeta) \tag{2.28}$$

where ω is now a parameter representing a particular frequency. Consistent with the simplification made in going from Eq. (2.20) to (2.22), the noise terms in Eq. (2.28) can be combined yielding

$$F(\omega_i, \zeta) = H(\omega_i)\, A(\omega_i, \zeta) + n(\omega_i, \zeta) \tag{2.29}$$

where $n(\omega_i, \zeta) = n_a(\omega_i, \zeta) + n_e(\omega_i, \zeta)$.

The stochastic concepts and models developed in this section will be utilized in deriving the optimal Wiener filter in Chapter III and in analyzing noise and scattering amplitude as random variables in Chapter V.

Estimation Problems

In this section, problems associated with scattering amplitude estimation are discussed in the frequency domain using deterministic concepts.

Ill-posedness

In an informal sense, an ill-posed question can be thought of as an ambiguously stated question or a question which cannot be answered based on available information. In terms of the scattering amplitude estimation problem, the general question can be stated as: "given a measured flaw signal, what is the flaw's scattering amplitude at all frequencies?" In a simplistic sense, this question can be separated into a well-posed question which can be stated as: "at frequencies where the system response is strong, what is the flaw's scattering amplitude?", and an ill-posed question which can be stated as: "outside of the bandwidth where the system response goes to zero, what is the flaw's scattering amplitude?"

These questions can be restated with the aid of equations as follows. In order to estimate a scattering amplitude by removing the measurement system response, the system response, $H(\omega)$, must be known. As discussed in more detail in Chapter IV, scattering amplitude estimation is carried out based on an estimate of $H(\omega)$. Typically, $H(\omega)$ is estimated by a combination of experimental and analytical procedures (Frederick and Seydel 1973, Tittman et al. 1977, Tittman and Thompson 1977, Thompson and

Gray 1982). For discussion purposes, consider an estimate of $H(\omega)$ as given by

$$\hat{H}(\omega) = H(\omega) + n_h(\omega) \tag{2.30}$$

where the error term, $n_h(\omega)$, is experimentally derived electronic noise. The subscript, h, is used here (instead of "e" for electronic noise) in order to create a distinction between the electronic noise associated with the measurement system response, $n_h(\omega)$, and the electronic noise associated with the flaw signal, $n_e(\omega)$. Combining Equations (2.20) and (2.30), a scattering amplitude estimate determined by deconvolution can be written as

$$\hat{A}(\omega) = \frac{F(\omega)}{\hat{H}(\omega)} = \frac{H(\omega)\ A(\omega) + n_a(\omega)}{H(\omega) + n_h(\omega)} + \frac{n_e(\omega)}{H(\omega) + n_h(\omega)} \tag{2.31}$$

Now, the well-posed question can be stated as: "at frequencies where $H(\omega)$ is much greater than $n_h(\omega)$, what is the flaw's scattering amplitude?" At such frequencies, the electronic noise terms ($n_e(\omega)$ and $n_h(\omega)$) are negligible due to averaging, and $\hat{A}(\omega)$ reduces to

$$\hat{A}(\omega) = A(\omega) + \frac{n_a(\omega)}{H(\omega)} \tag{2.32}$$

where the estimate is essentially equal to the true scattering amplitude plus an acoustic noise term. The ill-posed question can now be stated as: "at frequencies outside of the bandwidth (i.e., at frequencies where $\hat{H}(\omega)$ is dominated by $n_h(\omega)$), what is the flaw's scattering amplitude?" Outside of the bandwidth, all acoustic responses are zero and $\hat{A}(\omega)$ reduces to noise divided by noise and can be written as

$$\hat{A}(\omega) = \frac{n_e(\omega)}{n_h(\omega)} \tag{2.33}$$

Here, the deconvolution is clearly unstable and the scattering amplitude estimate in this range is meaningless. Since $n_h(\omega)$ and $n_e(\omega)$ are uncorrelated, near zero values in $n_h(\omega)$ may result in arbitrarily large values for $\hat{A}(\omega)$. Because the data in this region contain no useful information, the instability can essentially be ignored by not utilizing the experimental data outside of the bandwidth. However, in general, a scattering amplitude estimate must still be determined at frequencies outside of the bandwidth. This can be as basic as setting the estimate to zero or as complicated as extrapolation (Addison et al. 1982, Cohen-Tenoudji et al. 1984, Clark et al. 1985b, Clark et al. 1986, Koo 1988).

The dependence of the stability of the deconvolution on the relative strengths of $H(\omega)$ and $n_h(\omega)$ suggests that it would be conceptually useful to deal with a signal to noise ratio (S/N) based on Eq. (2.30) which is frequency dependent. Such a S/N will be denoted $SN_h(\omega)$ and is defined as

$$SN_h(\omega) = \frac{|H(\omega)|}{|n_h(\omega)|} \tag{2.34}$$

Note that when a signal to noise ratio is referred to in a generic sense, the common notation, S/N, will be used. At frequencies where $H(\omega)$ is much greater than $n_h(\omega)$, $SN_h(\omega)$ is large, and the deconvolution is stable (i.e., the problem is well-posed). Outside of the bandwidth where $H(\omega)$ goes to zero, $SN_h(\omega)$ goes to zero, and the deconvolution becomes unstable (i.e., the problem is ill-posed). The most problematic frequencies are

those for which $SN_h(\omega)$ is moderate and the deconvolution is potentially unstable.

Now consider ill-posedness more formally. For a problem to be well-posed, three conditions must be satisfied (Tikhonov and Arsenin 1977, Clark et al. 1986). In terms of the scattering amplitude estimation problem, these conditions are: 1) a scattering amplitude estimate exists, 2) the estimate is unique, and 3) small changes in the measured data result in small changes in the corresponding scattering amplitude estimate. If any of these conditions are violated, the problem becomes ill-posed.

Due to the instability of the deconvolution, one or more of these conditions can be violated causing the problem to be ill-posed. Consider measuring the backscattered signal from a given flaw twice without changing the experimental setup between measurements. Under these conditions, the two signals will differ only slightly where the difference will be due to the differences in electronic noise contributions. Here, due to the instability of the deconvolution, even though there is only one flaw and signals which are only slightly different, the corresponding flaw signature estimates may be drastically different (Lee et al. 1984, Clark et al. 1986). This situation violates the third condition. In addition, if the deconvolution as represented by Eq. (2.33) is carried out on a digital computer, the potential exists for $n_h(\omega)$ to be so close to zero that the division would result in values of $\hat{A}(\omega)$ which are too large for the computer to handle. Thus, in digital computer implementation, it may not be possible to calculate $\hat{A}(\omega)$ at certain frequencies. In essence, this is a violation of the first criterion stated above.

General estimation problems

Both the instability of the deconvolution and estimation in the presence of acoustic noise (Eq. (2.32)) are addressed by $SN_f(\omega)$ which is defined based on Eq. (2.22) as the ratio of the noise-free portion of the measured flaw signal, $|H(\omega)||A(\omega)|$, to the noise, $|n(\omega)|$ (Neal and Thompson 1986). That is, $SN_f(\omega)$ can be defined as

$$SN_f(\omega) = \frac{|H(\omega)|\ |A(\omega)|}{|n(\omega)|} \tag{2.35}$$

where the subscript "f" indicates association with the flaw signal. Outside of the bandwidth, $H(\omega)$ goes to zero, $SN_f(\omega)$ goes to zero, and the deconvolution is unstable. Within the bandwidth, the deconvolution is stable and $\hat{A}(\omega)$ (Eq. (2.32)) equals the true scattering amplitude plus an acoustic noise term. Here, $SN_f(\omega)$ is a measure of the relative strength of the contributions of the true scattering amplitude, $A(\omega)$, and noise to $\hat{A}(\omega)$. In fact, if a frequency dependent S/N were defined for Eq. (2.32), it would be equivalent to $SN_f(\omega)$. That is,

$$\frac{|A(\omega)|}{\frac{|n_a(\omega)|}{|H(\omega)|}} = \frac{|H(\omega)|\ |A(\omega)|}{|n(\omega)|} = SN_f(\omega) \tag{2.36}$$

where, if $n(\omega)$ is significant it is dominated by acoustic noise. Thus, $SN_f(\omega)$ addresses the stability of the deconvolution and is also an indication of the significance of acoustic noise within the bandwidth.

Review of Estimation Techniques

Various authors have addressed the flaw signature estimation problem with either explicit or implicit reference to the stable removal of measurement system effects. In 1978, Murakami et al. explicitly addressed the problem of flaw signature distortion caused by frequency dependent measurement system effects. They considered a time domain technique for flaw sizing based on the time delay between the front and back surface echoes from inclusions in silicone nitride (Si_3N_4) ceramics. In order to get the true time domain signature from the flaw which could be compared with theory, the system response was to be deconvolved out of the measured signal from the flaw. They stated that ideally, the system response could be removed by taking the fast Fourier transform (FFT) of the measured signal from the flaw and then multiplying it by an inverse filter of the form $1/H(\omega)$ where $H(\omega)$ represents the system frequency response. The ill-posedness of the problem was implicitly noted by stating that as $H(\omega) \rightarrow 0$ the filter would not be realizable. As a method of stabilizing the deconvolution, they proposed a Wiener filter, denoted by $W(\omega)$, of the form

$$W(\omega) = \frac{H^*(\omega)}{|H(\omega)|^2 + N^2} \tag{2.37}$$

where N^2 is added to "desensitize" the deconvolution. This technique, which is also known as constrained deconvolution, is stable (well-posed) since the positive constant, N^2, keeps the denominator from going to zero as $H(\omega)$ goes to zero. According to Murakami et al. N^2 was intended to be

the noise level in the system but for simplicity was set equal to an "arbitrary" constant. The value chosen for N^2 was not indicated.

Furgason et al. (1978) also reported the use of a constrained deconvolution in removing measurement system effects. Their work is particularly interesting in that it was derived as a time domain regularization approach and was then applied as constrained deconvolution in the frequency domain. Here, prior information is utilized to stabilize the problem. Specifically, the noise energy is assumed to be bounded and all signals are assumed to exist only in a finite time interval. It was then stated that a time domain flaw signature (i.e., a flaw's impulse response function) could be estimated by selecting the impulse response function, $\hat{R}(t)$, from the set, S, of all possible impulse response functions such that the following expression would be minimized.

$$\int_{-\infty}^{\infty} [c(t)\ \hat{R}_S(t)]^2\ dt \tag{2.38}$$

In Eq. (2.38), c(t) is a constraint operator which forces the impulse response estimate to meet some smoothness criterion and $\hat{R}_S(t)$ is the estimate which minimizes the expresion. Perhaps the most commonly used criterion in this type of approach is to look for the estimate which minimizes the second derivative by letting c(t) equal a second difference operator, $\delta''(t)$. This choice for the constraint operator tends to be too restrictive for the problem of estimating the impulse response function from a flaw since it does not allow the occurrence of delta function like features in the estimate. Furgason et al. employed a weaker smoothness

constraint by utilizing the identity operator, $\delta(t)$, as the constraint operator. The estimate which is sought therefore simply minimizes

$$\int_{-\infty}^{\infty} [\hat{R}_S(t)]^2 \, dt \tag{2.39}$$

For the discrete case, the Lagrangian multiplier approach (Phillips 1962, Twomey 1965) can be used to show that finding the estimate which minimizes Eq. (2.38) is equivalent to solving

$$\frac{\partial}{\partial \hat{R}} \left[\, |\hat{HR} - F|^2 + \gamma \, \hat{R}^* \hat{CR} \, \right] = 0 \tag{2.40}$$

where γ is a Lagrangian multiplier. They then stated that the solution of Eq. (2.40) could be written in the frequency domain as

$$\hat{A}(\omega) = \frac{F(\omega) \, H^*(\omega)}{|H(\omega)|^2 + \gamma \, |C(\omega)|^2} \tag{2.41}$$

where $C(\omega)$ is the Fourier transform of $c(t)$. They indicated that the choice of γ could essentially be related to the average noise power. The choice of γ was not dealt with further and it was not clear that Eq. (2.41) had actually been applied with γ determined in a formal manner.

Furgason et al. demonstrated the technique by considering the reflections resulting from two parallel plane surfaces. Both simulation and experimental results were shown. Experimentally, two parallel surfaces were created by utilizing stepped aluminum blocks. The ultrasonic interrogation of such a geometry would result in a measured signal dominated by the reflections at the two surfaces. The reflections would be separated in time by 2d/c were d is the step height and c is the longitudinal wave speed. They showed that the effect of the measurement

system was that the received signals were dominated by ringing at frequencies within the bandwidth to the extent that for small step size, the reflections from the two surfaces could not be distinguished. The signals were virtually noise free. The constrained deconvolution approach was then used to remove the distortion within the bandwidth. The system response, $H(\omega)$, was determined by the reflection off of the front surface of a planar aluminum blocks (i.e., a block without steps). The results showed improvement as the time domain signatures from all stepped aluminum blocks showed the anticipated reflections; however, bandlimitation effects were still evident. They also showed the results corresponding to deconvolution with no constraint ($F(\omega)/H(\omega)$). The resultant time domain signatures were dominated be high frequency variations and thus demonstrated the need to handle the ill-posedness of the problem. The dominant high frequency variations correspond to frequencies at which the deconvolution has "blown up" (see Eq. (2.33)).

Poe and Opsal also considered the case where prior information about the target was available. They assumed knowledge of the form of the true time domain signature from the stepped blocks and employed a non-linear pattern recognition routine to identify the undistorted signature from the distorted measured signal. The resultant signature is essentially a modeled version of the true signature were the parameters in the model are determined by the measured signal. In this manner, the bandlimitations were overcome since the bandlimited measured signal was only used to set the parameters in the ideal signature. Estimates of the signatures from the same blocks as considered by constrained deconvolution were given. These estimates showed dramatic improvements over the bandlimited results

determined by constrained deconvolution. Each signal was composed of two delta function like reflections with the appropriate time separation.

Elsley et al. (1980, 1981) formulated an optimal Wiener filter for the scattering amplitude estimation problem. The formulation explicitly accounts for the existence of acoustic noise; however, actual estimation in the presence of acoustic noise was not considered. Estimation outside of the bandwidth was implicitly considered by proposing a technique for combining the results for transducers with complementary bandwidths. Following the general digital filtering derivation given by Whalen (1971), Elsley et al. outlined the derivation of the optimal Wiener filter in terms of the scattering amplitude estimation problem. They used a stochastic model to describe the scattering amplitude estimation problem. In this approach, scattering amplitude and noise are assumed to be uncorrelated, Gaussian random variables with zero mean and known variance. Using the notation of Elsley et al., the model is given by

$$f(\omega) = p(\omega)\left[A(\omega) + \nu_1(\omega) + \nu_2(\omega)\right] + \nu_3(\omega) \qquad (2.42)$$

where $p(\omega)$=transducer and system response, $\nu_1(\omega)$=coherent clutter, $\nu_2(\omega)$=grain scattering, and $\nu_3(\omega)$=electronic noise. This model is of the same form as the deterministic model stated in Eq. 2.24 where the measurement system response is assumed to be the same for scattering at the flaw and at acoustic noise sources. Elsley et al. stated, relative to the noise terms, that "an important aspect of each is: what is its frequency dependence?". They went on to indicate that the frequency dependence of the noise sources is used by the optimal Wiener filter to determine an optimum estimate.

Derivation of the filter proceeds by maximizing the probability that the scattering amplitude estimate, $\hat{A}(\omega)$, is equal to the true scattering amplitude, $A(\omega)$, given that $f(\omega)$ has been measured in the presence of noise. The result of the derivation is a maximum likelihood estimate of the scattering amplitude which is optimal in the sense that it is the most probable (the "most likely") estimate. The resultant optimal filter can be written in the form of a constrained deconvolution where the constraining term, $\lambda^2(\omega)$, is determined optimally (see Eq. (1.4)). They gave the resultant scattering amplitude estimate for the case of additive noise only (i.e., $v_3(\omega)$ only)

$$\hat{A}(\omega) = \frac{f(\omega)\, p^*(\omega)}{|p(\omega)|^2 + \dfrac{C_v(\omega)}{C_A(\omega)}} \tag{2.43}$$

and for the case of acoustic noise only

$$\hat{A}(\omega) = \frac{f(\omega)\, p^*(\omega)}{|p(\omega)|^2 \left[1 + \dfrac{C_v(\omega)}{C_A(\omega)} \right]} \tag{2.44}$$

where $C_v(\omega)$ = expected value of $|v(\omega)|^2$ over the noise ensemble, $C_A(\omega)$ = expected value of $|A(\omega)|^2$ over the flaw ensemble, and the remaining terms are as defined relative to Eq. (2.42).

Elsley et al. described the behavior of the filter by noting that for good S/N (i.e., $C_v \ll |p|^2 C_A$) the scattering amplitude estimate reduces to the ideal result, $f(\omega)/p(\omega)$. For poor S/N (i.e., $C_v \gg |p|^2 C_A$) the scattering amplitude estimate is "desensitized" by the ratio $C_v(\omega)/C_A(\omega)$. Elsley et al. went on to note that among the advantages of the approach

are: a) noise with any frequency dependence is optimally handled, and b) noise which has passed through the transducer (i.e., acoustic noise) and which is not random in time like electronic noise is treated in the same manner as electronic noise.

Elsley et al. reported that they had not used the filter in its optimal form. They indicated that they had used the filter successfully by taking the ratio $C_V(\omega)/C_A(\omega)$ (i.e., $\lambda^2(\omega)$) to be equal to a constant and cited Murakami et al. (1978) as a reference. As an example of the application of constrained deconvolution with λ arbitrarily chosen, they considered the magnitude of the scattering amplitude for a 1200μm diameter spherical void in titanium. A backscattered signal from an actual void in titanium was used to demonstrate the effect of the choice of λ on the stability of the deconvolution outside of the bandwidth. The graphical results demonstrated that too little desensitization results in wild variations in $|\hat{A}(\omega)|$ at frequencies where the S/N was not favorable (i.e., near and outside of the system bandwidth where $SN_h(\omega)$ is not favorable). The distortion associated with the measured signal was not shown, so the improvements due to constrained deconvolution were not demonstrated. They indicated that one of the scattering amplitude estimates represented the optimum estimate. However, they did not indicate how the optimum estimated was determined, what value of λ corresponded to optimal constraint, or what criterion was used to establish the optimum estimate.

The most commonly used scattering amplitude estimation technique (Elsley and Addison 1981, Addison et al. 1982, Thompson and Gray 1982, Gray 1982, Thompson et al. 1986) has grown out of the work of Murakami et al. (1978) and Elsley et al. (1980, 1981). This technique involves a

constrained or desensitized deconvolution (referred to here as the desensitization filter) with a non-optimally chosen contraining term. Application of the desensitization filter plus estimation outside of the bandwidth will be referred to as the desensitization filter algorithm (Elsley and Addison 1981, Addison et al. 1982, Thompson and Gray 1982, Gray 1982). The algorithm as defined here follows explicitly the algorithm that was established by Gray (1982) as part of an inverse Born sizing algorithm. The algorithm can be defined in terms of three distinct steps: 1) application of the desensitization filter, 2) low frequency extrapolation, and 3) high frequency windowing.

The functional definition of the upper and lower limits of the bandwidth as used in the algorithm is given first. The magnitude of a typical ultrasonic measurement system response, $|H(\omega)|$, is shown in Fig. 2.4.a. Also shown on the graph is a horizontal line which has been drawn at a level equal to 10% of the maximum value of $|H(\omega)|$. The intersection of this horizontal line with $|H(\omega)|$ determines the lower limit of the bandwidth, f_{min}, and the upper limit, f_{max}.

Step 1 of the algorithm involves application of the desensitization filter. Through common usage (perhaps following the lead of Elsley and Addison (1981)) λ is set equal to 10% of the maximum value of $|H(\omega)|$. The scattering amplitude estimate which results from the application of the desensitization filter can therefore be written as

$$\hat{A}(\omega) = \frac{F(\omega)\, H^{*}(\omega)}{|H(\omega)|^{2} + \lambda^{2}} \qquad (2.45)$$

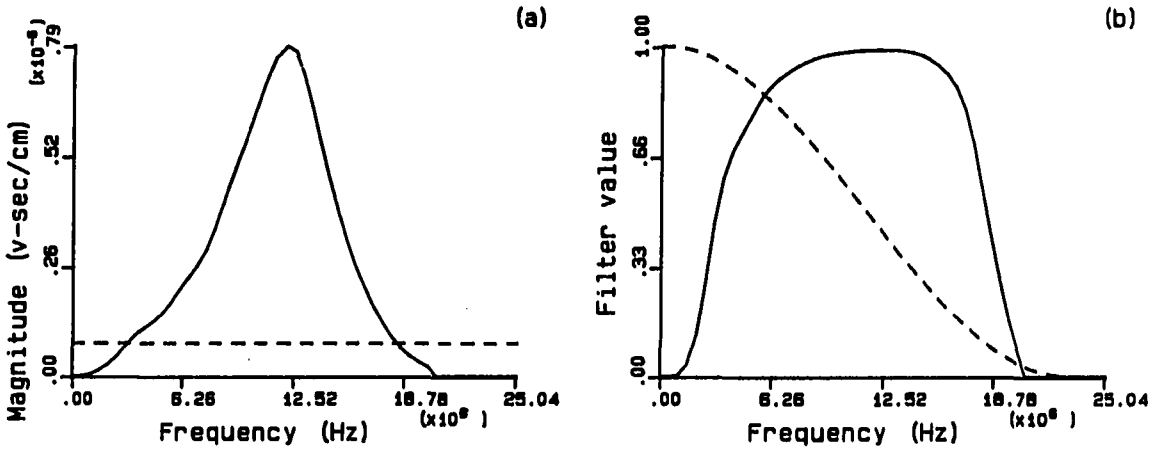

Figure 2.4. Desensitization filter. a) typical $|H(\omega)|$ (solid) and a line (dashed) at 10% of the maximum value of $|H(\omega)|$; b) filter term, $W(\omega)$, (solid) and cosine-squared window (dashed)

where $\lambda=0.1\,|H(\omega)|_{max}$. Through algebraic manipulation, Eq. (2.45) can be rewritten in the form of a filter term, $W(\omega)$, times the unconstrained deconvolution, $F(\omega)/H(\omega)$. The resultant form is given by

$$\hat{A}(\omega) = W(\omega)\left[\frac{F(\omega)}{H(\omega)}\right] \tag{2.46}$$

where the filter term can be written as

$$W(\omega) = \frac{\dfrac{|H(\omega)|^2}{\lambda^2}}{\dfrac{|H(\omega)|^2}{\lambda^2} + 1} \tag{2.47}$$

Note that $W(\omega)$ is a real-valued filter term which takes on values between zero and one. The solid line in Fig. 2.4.b shows $W(\omega)$ with $\lambda=0.1\,|H(\omega)|_{max}$

for the system repsonse given in Fig. 2.4.a. Notice that the filter essentially acts as a bandpass filter.

Step 2 involves low frequency extrapolation. Below f_{min}, the estimate determined in step 1 is assumed to contain no useful information. Thus, from zero frequency to f_{min}, the estimate determined in step 1 is replaced by an estimate determined via extrapolation. Extrapolation is achieved by first doing a least-square error fit of a polynomial to $\hat{A}(\omega)$ (from step 1) at frequencies just above f_{min}. From zero frequency to f_{min}, $\hat{A}(\omega)$ from step 1 is then replaced with an estimate determined with the polynomial. The polynomial is of the form (Gray 1982, Thompson and Gray 1982)

$$A_2\omega^2 + A_4\omega^4 + A_6\omega^6 + i\left[A_3\omega^3 + A_5\omega^5 + A_7\omega^7\right] \tag{2.48}$$

Use of the polynomial is justified by noting that for a flaw with center of inversion symmetry, $A(\omega)$ has the power series expansion (Richardson 1984)

$$A(\omega) = A_2\omega^2 + iA_3\omega^3 + A_4\omega^4 + iA_5\omega^5 + \ldots \tag{2.49}$$

where the coefficients A_i are real.

Step 3 involves high frequency windowing. Above f_{max}, it is also assumed that the estimate determined in step 1 contains no useful information. In order to force the scattering amplitude estimate to zero at high frequencies, the estimate is multiplied by a cosine-squared window which is centered at zero frequency and decreases to zero at 25% above f_{max} (Addison et al. 1982). The window for the system response shown in Fig. 2.4.a is given by the dashed line in Fig. 2.4.b.

Lee (1981) explicitly considered the impulse response estimation problem as an ill-posed problem. A time domain regularizing approach was described which utilizes basic splines. Time domain regularization approaches, in essence, establish a rational way for determining the estimate, $\hat{R}(t)$, which minimizes $[F(t)-\hat{R}(t)*H(t)]^2$. The approach described by Lee first approximates F(t) and H(t) with best least-square smoothing splines. These spline representations will be denoted, $\tilde{F}(t)$ and $\tilde{H}(t)$, respectively. A third spline which represents $\hat{R}(t)$ is then sought such that $[\tilde{F}(t)-\hat{R}(t)*\tilde{H}(t)]^2$ is minimized. Lee gave one example where the F(t) and H(t) were shown along with $\tilde{F}(t)$, $\tilde{H}(t)$, and the resultant estimate $\hat{R}(t)$. While the results demonstrate the concept, since only one example was given and comparisons with theoretical results were not given, the results did not demonstrate improvements due to the removal of measurement system effects. Noise and estimation outside of the bandwidth were not considered.

Poe and Opsal (1982) also utilized a time domain technique which looks for an estimate, $\hat{R}(t)$, such that $[F(t)-\hat{R}(t)*H(t)]^2$ is minimized. Like the approach of Furgason et al. (1978) for the known target case, Poe and Opsal assume that the flaw to be characterized comes from a set of known scatterers. For example, it may be known that the flaw is a spherical void with unknown radius which comes from the set of scatterers made up of all possible sizes of spherical voids. A model for the impulse response functions for the flaws in the known set of scatterers is assumed to be known such that all flaws in the set can be represented by some $\hat{R}(t,\Theta)$. Here, Θ is a parameter vector (simply the radius for the spherical void case) which defines a one-to-one correspondence between

flaws in the set and impulse response functions. Corresponding to each impulse response function in the set, an output signal, $\hat{F}(t,\theta)$, can be calculated as $\hat{R}(t,\theta)*H(t)$. The problem thus reduces to finding the θ which minimizes $[F(t)-\hat{F}(t,\theta)]^2$. In implementing the technique, the possibility of a phase error and a scaling error between $F(t)$ and $\hat{F}(t,\theta)$ is accounted for. That is, as implemented, $[F(t)-b\hat{F}(t-\tau,\theta)]^2$ is minimized where b is included to account for unknown scaling and τ is determined such that the cross-correlation between $F(t)$ and $\hat{F}(t,\theta)$ is a maximum. This technique not only attempts to overcome distortion and bandlimitation effects by utilizing a model for the response of the flaw, but it also yields a characterization of the flaw as defined by the parameter vector, θ. In addition, a time shift, τ, is determined which can be used in simulation studies to establish the position of the actual centroid of the flaw versus the position of the perceived centroid as defined by τ.

Simulation results were generated by Poe and Opsal assuming a set of spherical voids. The presence of electronic noise was simulated by adding uncorrelated white Gaussian noise. They showed that the method defined above for determining θ yields an unbiased estimate in the presence of this type of noise. The impulse response functions, $\hat{R}(t,\theta)$, were determined by first generating scattering amplitudes followed by an IFT. Results were given for a nearly noise-free case (S/N=120dB) and for a highly noise corrupted case (S/N=-3dB). The error, $[F(t)-b\hat{F}(t-\tau,\theta)]^2$, was plotted versus θ/a, where "a" equals the actual sphere radius. The best solution was determined by looking for the minimum in the curve. For the 120dB case, the minimum occurred at the correct flaw size, that is, at $\theta/a=1.0$. For the -3dB case, the minimum was at $\theta/a=0.988$. This result

was taken as an indication of the robustness of the technique in the presence of electronic noise.

Poe and Opsal also considered the case where the flaw to be characterized is not actually contained within the assumed set of known scatterers. They considered the case of a spherical void with an attached hemispherical bubble. Results were given for three interrogation directions. For each case, the cross section of the actual flaw shape and the best spherical approximation to the actual shape were plotted. The results were reasonably good. Since the technique also yields the time shift, τ, it was possible to graphically depict the position of the spherical approximation to the actual flaw. The expected result was achieved for two of the three interrogation directions, i.e., the best spherical estimate was a sphere larger than the base sphere of the actual flaw, and the position of the centroid of the best spherical estimate was offset toward the side of the actual sphere containing the hemispherical bubble. In both cases, the results essentially demonstrate the ability of the technique to size the scatterer. Since this is a model based approach, it yields an impulse response estimate which contains no distortion and is not bandlimited by any experimental system. Since examples of the estimated impulse response functions were not shown, the removal of distortion and bandlimitation effects could not be evaluated.

Bhagat and Shimmin (1984) proposed the use of homomorphic processing (Oppenheim and Schafer 1975) to remove distortion effects in the presence of noise. They referred to the problem of estimating the flaw's signature as an ill-posed system identification problem. The measured signal from a flaw was modeled in a similar fashion to the model of Eq. (2.24) with both

acoustic noise and electronic noise included. They identified acoustic noise as being the most problematic noise since it occupies the same frequency band as the scattered field from the flaw. Results for simulated acoustic noise were given; however, it was not clear that the simulated acoustic noise had been given any inherent frequency dependence (e.g., it may have been simulated by convolving white noise with a system response, $H(\omega)$). The only explanatory comment made about homomorphic processing was that "the complex cepstra of ultrasonic pulses and impulse response will occupy disjointed spaces in the cepstral domain due to the bandlimited nature of the ultrasonic pulses." The complex cepstra (Oppenheim and Schafer 1975) was defined as the "inverse Fourier transform of the complex logarithm of a Fourier transformed signal." The processing steps used were not defined or discussed. It was stated that routines were adapted from the literature. Comments about improvements over conventional deconvolution techniques and comments about actual material samples were made; however, it did not appear that results pertaining to either conventional deconvolution or actual material samples had been presented.

Bhagat et al. (1984) gave a comparison of impulse response estimates and corresponding flaw radius estimates (determined via the inverse Born) as determined by cepstral processing, constrained deconvolution (Furgason et al. 1978), and by the time domain spline technique of Lee (1981). Again, the cepstral technique was not defined. Results at a variety of signal to noise ratios were given for the case of simulated acoustic noise. For each technique, impulse response estimates, characteristic function estimates, and flaw radius estimates were given. The manner in

which the techniques were applied was not defined. Therefore, interpretation of the results is not possible.

Clark et al. (1986) explicitly addressed the problem of restoring true impulse response functions from distorted data. They indicated that the problem is a system identification problem which is, in general, ill-posed. They outlined a time domain regularization approach based on energy constraints. The technique was also stated in the frequency domain as a constrained deconvolution. The techniques were referred to as time domain and frequency domain Wiener identification algorithms, respectively. It was said that the constraining term could be determined by a variety of methods including trial and error and a number of more exotic methods. They indicated that they had found that the simple Wiener schemes with non-optimally chosen constraint perform as well as more sophisticated schemes. Experimental results were shown which demonstrated the performance of the technique. The backscattered signal from a crack was simulated by interrogating a machined slot in a block of aluminum. The measured signal was shown with distortion effect evident. The signal was then shown after distortion effects had been removed via constrained deconvolution (Clark et al. 1985a). Some improvement was evident; however, bandlimitation effects were still evident. Estimation outside of the bandwidth was then considered. A constrained extrapolation algorithm was used (Clark et al. 1985b). With distortion effects removed and extrapolation performed, the signal showed dramatic improvement.

They also showed the ability of the technique to work in a detection environment by considering a time domain signal which included both the back surface reflection from the aluminum block and the signal from the

simulated crack. The distortion in the measured signal obscured the crack signal. With distortion effects removed but without extrapolation, the crack signal was still masked by the low frequency errors due to bandlimitation effects. With the extrapolation complete, low frequency errors were removed, and the crack signal was drawn out.

Clark et al. summarized by stating that the removal of distortion effects alone or extrapolation alone yielded moderate improvements. However, the removal of distortion effects followed by extrapolation yielded dramatically improved impulse response estimates.

The techniques summarized above have utilized different types and amounts of prior information. Little attention was paid to estimation outside of the bandwidth or acoustic noise. The characterization of neither acoustic noise nor electronic noise was reported even when average noise characteristics were required for the optimal implementation of a technique. A very limited number of examples was considered and no consideration was given to the performance of any technique over a distribution of scatterers or noise signals. The impact of the removal of measurement system effects on flaw sizing results received little attention. Reports of the continued investigation of any of the techniques have not been found in the literature.

CHAPTER III. FILTER DERIVATION

This chapter deals with the derivation of the optimal Wiener filter for the general case where $A(\omega)$ and $n(\omega)$ are assumed to have known mean and variance (Neal and Thompson 1987). The derivation presented here differs significantly from the derivation outlined by Elsley et al. (1980) in that they assumed $A(\omega)$ and $n(\omega)$ had zero mean. It is thought that the mathematics of the derivation for the non-zero mean case may have been done; however, after an exhaustive literature search the derivation has not been found. Given this situation and since Elsley et al. (1980) gave only a brief outline the derivation for the zero mean case, the derivation for the general case is presented below in some detail. The zero mean cases will then be treated as special cases whose filter forms can be reached directly from the general result. The chapter is concluded with a comparison between the model, assumptions, and filter forms presented here and those of Elsley et al. (1980).

General Case Derivation

The stochastic model and assumptions on which the derivation is based are first explicitly stated. Using shorthand notation, the model given in Eq. (2.29) can be written as

$$F(\omega) = H(\omega)\, A(\omega) + n(\omega) \tag{3.1}$$

where $n(\omega)=n_a(\omega)+n_e(\omega)$. Associated with this model, it is assumed that at each frequency 1) $A(\omega)$, $n_a(\omega)$, and $n_e(\omega)$ are uncorrelated, Gaussian random

variables; 2) the mean and variance associated with $A(\omega)$ and $n(\omega)$, respectively, are known; and 3) $H(\omega)$ is not a random variable. As a consequence of these assumptions, $F(\omega)$ and $n(\omega)$ must also be Gaussian random variables. This is clear by noting that a) the product of a constant and a Gaussian random variable is also a Gaussian random variable, and b) the sum of Gaussian random variables yields a Gaussian random variable (Papoulis 1965).

The random variables in Eq. (3.1) are complex random variables of the general form $z(\omega_i, \zeta)$. Goodman (1963) states that if $z(\omega_i, \zeta)$ is Gaussian, it is a univariate complex random variable whose real and imaginary parts are bivariate Gaussian distributed. Using the shorthand notation, z, for the complex random variable, $z(\omega_i, \zeta)$, the mean, m_z, can be defined in the usual way in terms of the expectation operator, $E[\cdot]$, as

$$m_z = E[z] = E[x] + iE[y] = \int_{-\infty}^{\infty} xf(x)dx + i\int_{-\infty}^{\infty} yf(y)dy \tag{3.2}$$

where $f(x)$ and $f(y)$ are the probability density functions for x and y, respectively (Papoulis 1965). The variance, σ_z^2, can be defined as

$$\sigma_z^2 = E\left[|z - E[z]|^2\right] = E\left[(x-m_x)^2 + (y-m_y)^2\right] = \sigma_x^2 + \sigma_y^2 \tag{3.3}$$

For a complex random variable to be uncorrelated, its real and imaginary parts must by uncorrelated (Papoulis 1965, Goodman 1963, Whalen 1972). This means that the correlation coefficient, ρ_z, defined as

$$\rho_z = \frac{E[(x-m_x)(y-m_y)]}{\sigma_x \sigma_y} \tag{3.4}$$

must be equal to zero (i.e., $E[(x-m_x)(y-m_y)]=0$). In addition, assuming that scattering amplitude and noise are uncorrelated, means that $A(\omega)$ is uncorrelated, $n(\omega)$ is uncorrelated, and $A(\omega)$ is uncorrelated with $n(\omega)$. The first two requirements were addressed above relative to Eq. (3.4). The later requirement means that all combination of the real and imaginary parts of $A(\omega)$ and $n(\omega)$ must be uncorrelated. The correlation between $A(\omega)$ and $n(\omega)$ will be discussed further in Chapter V.

The derivation presented here is carried out at a particular frequency (Elsley et al. 1980). This approach is thought to be more transparent than a matrix based approach (Whalen 1971). For simplicity, the parameter ω is not explicitly represented during the derivation; therefore, it will be implicit that the derivation is done at a particular frequency.

The estimation problem is to find the "best" scattering amplitude estimate, $\hat{A}$, given a noise-corrupted measured flaw signal, F. A common criterion for establishing the "best" estimate is to minimize the squared error between $\hat{A}$ and the actual scattering amplitude, A. It can be shown (Whalen 1971) that the estimate which minimizes $|\hat{A} - A|^2$ is the mean value, E[A/F], of the <u>a posteriori</u> probability density function, $f(A/F)$ (Whalen 1971, Mendel 1983). If $f(A/F)$ is Gaussian, then the mean corresponds to the value at which $f(A/F)$ is maximum. Thus, if $f(A/F)$ is Gaussian, maximizing $f(A/F)$ is equivalent to minimizing the squared error. The value of A at which $f(A/F)$ is maximum will be denoted $\hat{A}$ and is known as the maximum <u>a posteriori</u> estimate (Whalen 1971, Mendel 1983).

In equation form, the problem is to find the value of A at which $f(A/F)$ is maximum by solving

$$\frac{\partial}{\partial A} f(A/F) = 0 \tag{3.5}$$

where the solution is $\hat{A}$. Using Bayes rule, $f(A/F)$ can be expressed as

$$f(A/F) = \frac{f(F/A)\ f(A)}{f(F)} \tag{3.6}$$

Since $f(F)$ acts as a normalization factor and does not depend on A, maximizing $f(A/F)$ is equivalent to maximizing the product $f(F/A)f(A)$ (Whalen 1971, Fertig and Richardson 1980). Thus, $\hat{A}$ is the value of A which satifies

$$\frac{\partial}{\partial A} f(A/F) = \frac{\partial}{\partial A} [f(F/A)\ f(A)] = 0 \tag{3.7}$$

Since Gaussian probability density functions involve exponentials, it will prove convenient to maximize Log $f(A/F)$ which is equivalent to maximizing $f(A/F)$ (Whalen 1971, Mendel 1983). The problem thus reduces to solving

$$0 = \frac{\partial}{\partial A} \text{Log } f(F/A) + \frac{\partial}{\partial A} \text{Log } f(A) \tag{3.8}$$

Assuming that the real and imaginary parts of A are uncorrelated, the complex Gaussian probability density function $f(A)$ can be written as (Goodman 1963)

$$f(A) = \Theta \exp\left[\frac{-|A - m_A|^2}{2\sigma_A^2} \right] \tag{3.9}$$

where $\Theta = 1/(\pi\sigma_A^2)$. This is the <u>a priori</u> probability density function for A (Whalen 1971). Note that this is the point at which prior information

about the flaw distribution enters the derivation. The second term in Eq. (3.8) can now be expressed as

$$\frac{\partial}{\partial A} \text{Log } f(A) = \frac{\partial}{\partial A}[\text{Log } \Theta] + \frac{\partial}{\partial A}\left[\frac{-|A - m_A|^2}{2\sigma_A^2}\right] = \frac{-1}{2\sigma_A^2}\frac{\partial}{\partial A}|A - m_A|^2 \quad (3.10)$$

where $\partial/\partial A[\text{Log } \Theta]=0$. In order to carry out the differentiation, the squared term is written out using complex conjugates as

$$\frac{\partial}{\partial A} \text{Log } f(A) = \frac{-1}{2\sigma_A^2}\frac{\partial}{\partial A}\left[(A - m_A)(A^* - m_A^*)\right] \quad (3.11)$$

The differentiation can now be carried out utilizing the rule for differentiation of the product of complex functions (Hille 1959) yielding

$$\frac{\partial}{\partial A} \text{Log } f(A) = \frac{-1}{2\sigma_A^2}\left[(1 - 0)(A^* - m_A^*) + (A - m_A)(0 - 0)\right] \quad (3.12)$$

where it is noted that while the total derivative of A^* with respect to A is not defined (Saff and Snider 1976), the partial derivative, $\partial A^*/\partial A$, is equal to zero (Hille 1959). Finally, Eq. (3.12) is rearranged as

$$\frac{\partial}{\partial A} \text{Log } f(A) = -\frac{A^*}{2\sigma_A^2} + \frac{m_A^*}{2\sigma_A^2} \quad (3.13)$$

In a similar fashion, the first term in Eq. (3.8) can be evaluated (some intermediate steps will not be shown). Assuming that the real and imaginary parts of n are uncorrelated and assuming that n and A are uncorrelated, the density function $f(F/A)$ can be written as (Whalen 1971, Elsley et al. 1980)

$$f(F/A) = \Theta \exp\left[\frac{-|F - (HA + m_n)|^2}{2\sigma_n^2}\right] \tag{3.14}$$

where $\Theta = 1/(\pi\sigma_F^2)$. The function $f(F/A)$ is an a posteriori probability density function for F. That is, it describes F after the value of A is known. Therefore, noting that A and n are uncorrelated and referring to Eq. (3.6), the distribution has a mean equal to H times the value of A, plus the mean of the noise. The distribution variance is given solely by the variance of the noise since A is given (Whalen 1971). This is the point at which prior information about the noise distribution enters the derviation. Substituting $f(F/A)$ into the first term in Eq. (3.8), setting $\partial/\partial A[\text{Log } \Theta]=0$, and writing out the squared term yields

$$\frac{\partial}{\partial A} \text{Log } f(F/A) = \frac{-1}{2\sigma_n^2} \frac{\partial}{\partial A}\left[(F - HA - m_n)(F^* - H^*A^* - m_n^*)\right] \tag{3.15}$$

Carrying out the differentiation (see Eq. (3.12)) results in

$$\frac{\partial}{\partial A} \text{Log } f(F/A) = \frac{-1}{2\sigma_n^2}\left[(-H)(F^* - H^*A^* - m_n^*) + (F - HA - m_n)(0)\right] \tag{3.16}$$

which can be rearranged to give

$$\frac{\partial}{\partial A} \text{Log } f(F/A) = \frac{F^*H}{2\sigma_n^2} - \frac{A^*|H|^2}{2\sigma_n^2} - \frac{m_n^* H}{2\sigma_n^2} \tag{3.17}$$

Having evaluated the two terms in Eq. (3.8), the results can now be combined by substituting Equations (3.13) and (3.17) into Eq. (3.8). As stated by Whalen (1971), since the solution represents the maximum

a posteriori estimate, $\hat{A}$ is substituted for A. The resultant equation is given by

$$0 = \left[\frac{FH^*}{2\sigma_n^2} - \frac{\hat{A}|H|^2}{2\sigma_n^2} - \frac{m_n H^*}{2\sigma_n^2} \right] + \left[- \frac{\hat{A}}{2\sigma_A^2} + \frac{m_A}{2\sigma_A^2} \right] \tag{3.18}$$

where the complex conjugate has been taken of both sides of the equation. Taking terms involving $\hat{A}$ to the left side and rearranging yields

$$\hat{A} \left[\frac{|H|^2}{\sigma_n^2} + \frac{1}{\sigma_A^2} \right] = \frac{H^*}{\sigma_n^2} \left[F - m_n \right] + \frac{1}{\sigma_A^2} \left[m_A \right] \tag{3.19}$$

The terms in the bracket on the left side of the equation are now placed over a common denominator, the left hand side of the equation is multiplied by $\sigma_n^2(\omega)/\sigma_n^2(\omega)$, and both sides are multiplied by $1/|H|^2$. The result is

$$\hat{A} \left[\frac{\frac{|H|^2\sigma_A^2}{\sigma_n^2} + 1}{\frac{|H|^2}{\sigma_A^2}} \right] = \frac{1}{\sigma_n^2} \left[\frac{(F - m_n)H^*}{|H|^2} \right] + \frac{1}{|H|^2\sigma_A^2} \left[m_A \right] \tag{3.20}$$

Finally, solving for $\hat{A}$ yields the final result

$$\hat{A} = \frac{\frac{|H|^2\sigma_A^2}{\sigma_n^2}}{\frac{|H|^2\sigma_A^2}{\sigma_n^2} + 1} \left[\frac{(F - m_n)H^*}{|H|^2} \right] + \frac{1}{\frac{|H|^2\sigma_A^2}{\sigma_n^2} + 1} \left[m_A \right] \tag{3.21}$$

This is the resultant scattering amplitude estimate for the general case determined by the optimal Wiener filter.

In order to avoid confusion, full random variable notation is now re-introduced. Equation (3.21) can be written in the form of a weighting term, W_1, times the first bracketed term, plus a second weighting term, W_2, times the second bracketed term (Neal and Thompson 1987). Using this format and based on Eq. (3.21), the optimal Wiener filter determines a scattering amplitude estimate at the i^{th} frequency for the k^{th} flaw as

$$\hat{A}(\omega_i, \zeta_k) = W_1(\omega_i) \left[\frac{(F(\omega_i, \zeta_k) - m_n(\omega_i))\, H^*(\omega_i)}{|H(\omega_i)|^2} \right] + W_2(\omega_i) \left[m_A(\omega_i) \right] \quad (3.22)$$

where the weighting terms are

$$W_1(\omega_i) = \frac{\dfrac{|H(\omega_i)|^2\, \sigma_A^2(\omega_i)}{\sigma_n^2(\omega_i)}}{\dfrac{|H(\omega_i)|^2\, \sigma_A^2(\omega_i)}{\sigma_n^2(\omega_i)} + 1} \qquad W_2(\omega_i) = \frac{1}{\dfrac{|H(\omega_i)|^2\, \sigma_A^2(\omega_i)}{\sigma_n^2(\omega_i)} + 1} \quad (3.23)$$

Note that only the measured flaw signal and the scattering amplitude estimate are a function of the flaw being considered (ζ_k). All other quantities are fixed once the flaw and noise distributions are defined.

Special Case Results

Based on the discussions in Chapter II relative to Figures 2.2 and 2.3, it is perhaps most realistic to assume that $m_n(\omega)=0$ and $m_a(\omega)$ is known but not equal to zero at all frequencies. Therefore, the optimal Wiener filter is analyzed in the remaining chapters based on these

assumptions. For completeness, the filter form for this case and the case when both variables are zero mean are given below.

The result for zero mean noise can be determined directly from the general result by setting $m_n(\omega)=0$. The result is

$$\hat{A}(\omega_i,\zeta_k) = W_1(\omega_i)\left[\frac{F(\omega_i,\zeta_k)\,H^*(\omega_i)}{|H(\omega_i)|^2}\right] + W_2(\omega_i)\left[m_A(\omega_i)\right] \qquad (3.24)$$

where the weighting terms are

$$W_1(\omega_i) = \frac{\dfrac{|H(\omega_i)|^2\,\sigma_A^2(\omega_i)}{E[n^2(\omega_i)]}}{\dfrac{|H(\omega_i)|^2\,\sigma_A^2(\omega_i)}{E[n^2(\omega_i)]}+1} \qquad W_2(\omega_i) = \frac{1}{\dfrac{|H(\omega_i)|^2\,\sigma_A^2(\omega_i)}{E[n^2(\omega_i)]}+1} \qquad (3.25)$$

Note that the noise variance is written as $E[n^2(\omega_i)]$ to emphasize that for zero mean, the variance becomes the mean square value or average noise power.

The result for both zero mean noise and zero mean scattering amplitude can also be determined directly from the general result by setting $m_n(\omega)=0$ and $m_A(\omega)=0$. The resultant estimate is given by

$$\hat{A}(\omega_i,\zeta_k) = W_1(\omega_i)\left[\frac{F(\omega_i,\zeta_k)\,H^*(\omega_i)}{|H(\omega_i)|^2}\right] + W_2(\omega_i)\left[0\right] \qquad (3.26)$$

The second weighting term and the 0 are left in the filter to emphasize that the scattering amplitude mean is still involved in determing the estimate, the mean just happens to be equal to zero. The first weighting term can be written as

$$W_1(\omega_i) = \frac{\frac{|H(\omega_i)|^2 \, E[A^2(\omega_i)]}{E[n^2(\omega_i)]}}{\frac{|H(\omega_i)|^2 \, E[A^2(\omega_i)]}{E[n^2(\omega_i)]} + 1} \tag{3.27}$$

where both the scattering amplitude and noise variance are now written in terms of the expected value of the square of the variable.

Comparison with Previous Results

The zero mean results presented above will now be compared with the results given by Elsley et al. (1980). It will be shown (again using shorthand notation) that there is no loss in generality by combining $H_a(\omega)$ and $A_a(\omega)$ into $n_a(\omega)$, and by combining $n_a(\omega)$ and $n_e(\omega)$ into $n(\omega)$. First, implications relative to scattering amplitude mean assumptions will be discussed.

The most critical difference between this derivation and that of Elsley et al. lies in the assumption relative to the scattering amplitude mean. As is evident from the filter forms stated above, eliminating the assumption that $m_A(\omega)=0$ results in a second term involving the scattering amplitude mean. Notice the implications of assuming $m_A(\omega)=0$ in terms of the flaw ensemble. From Eq. (3.2), assuming that $m_A(\omega)=0$ means that $\mathrm{Re}[m_A(\omega)]=0$ and $\mathrm{Im}[m_A(\omega)]=0$. Considering the real part for discussion purposes, assuming $\mathrm{Re}[m_A(\omega)]=0$ is essentially equivalent to assuming that (at each frequency) the $\mathrm{Re}[A(\omega)]$ for half of the flaws in the flaw ensemble is positive and $\mathrm{Re}[A(\omega)]$ for the other half of the flaws in

negative. Based on the discussions of Chapters II, at low frequencies, this would mean that the reflection coefficient (Eq. (2.6)) is positive for half of the flaws ($z_h > z_f$) and negative for the other half ($z_h < z_f$). Except for the weak scattering case in which $z_h \approx z_f$, the implication is that if $m_A(\omega)=0$, the flaw ensemble is not well defined. It is important to reemphasize that model based techniques (of which the optimal Wiener filter is one) require a significant amount of prior information. Therefore, if enough prior information is available to estimate $m_A(\omega)$ and $\sigma_A^2(\omega)$, then $m_A(\omega)$ will not be equal to zero at all frequencies. It will be shown in Chapter V that for a reasonably well defined flaw ensemble, $E[A(\omega)]$ is not equal to zero at each frequency.

Now consider the equivalence of the zero mean results given above with the results given by Elsley et al. The derivation outlined by Elsley et al. was based on a model of the form

$$F(\omega) = H(\omega)\,[A(\omega) + A_a(\omega)] + n_e(\omega) \tag{3.28}$$

where it is assumed that $H_a(\omega)=H(\omega)$. They reported optimal Wiener filter forms for acoustic noise only (based on the model $F(\omega)=H(\omega)[A(\omega)+A_a(\omega)]$), and for electronic noise only (based on the model $F(\omega)=H(\omega)A(\omega)+n_e(\omega)$).

Before proceeding, the following relationships are needed. Since $H_a(\omega)$ is not a random variable (i.e., it is assumed to be a constant over ζ at a each frequency), the mean associated with acoustic noise can be written as

$$m_{n_a}(\omega) = E[n_a(\omega)] = E[H_a(\omega)A_a(\omega)] = H_a(\omega)E[A_a(\omega)] \tag{3.29}$$

and the variance can be written as

$$\sigma^2_{n_a}(\omega) = E[n_a^2(\omega)] = E[H_a^2(\omega)A_a^2(\omega)] = |H_a(\omega)|^2 E[A_a^2(\omega)] \tag{3.30}$$

Also, since $n_a(\omega)$ and $n_e(\omega)$ are uncorrelated, and the mean and variance associated with $n(\omega)$ can be written as

$$m_n(\omega) = m_{n_a}(\omega) + m_{n_e}(\omega) \tag{3.31}$$

$$\sigma^2_n(\omega) = \sigma^2_{n_a}(\omega) + \sigma^2_{n_e}(\omega) \tag{3.32}$$

The equivalence of filter forms can now be shown by first rewriting Equations (3.26) and (3.27) in a constrained deconvolution form as

$$\hat{A}(\omega) = \frac{F(\omega)\, H^*(\omega)}{|H(\omega)|^2 + \dfrac{E[n^2(\omega)]}{E[A^2(\omega)]}} \tag{3.33}$$

Utilizing Equations (3.30) and (3.32), Eq. (3.33) can be written as

$$\hat{A}(\omega) = \frac{F(\omega)\, H^*(\omega)}{|H(\omega)|^2 + \dfrac{|H_a(\omega)|^2 E[A_a^2(\omega)] + E[n_e^2(\omega)]}{E[A^2(\omega)]}} \tag{3.34}$$

If only electronic noise is present, then Eq. (3.34) reduces to

$$\hat{A}(\omega) = \frac{F(\omega)\, H^*(\omega)}{|H(\omega)|^2 + \dfrac{E[n_e^2(\omega)]}{E[A^2(\omega)]}} \tag{3.35}$$

which is equivalent to Eq. (2.43) as stated by Elsley et al. For the case of acoustic noise only and assuming $H_a(\omega)=H(\omega)$, Eq. (3.34) reduces to

$$\hat{A}(\omega) = \frac{F(\omega)\, H^*(\omega)}{|H(\omega)|^2 \left[1 + \dfrac{E[A_a^2(\omega)]}{E[A^2(\omega)]} \right]} \tag{3.36}$$

which is equivalent to Eq. (2.44). As expected, the filter forms determined by using $n(\omega)$ are equivalent to the filter forms stated by Elsley et al. (1980).

Finally, notice that the manner in which the noise terms are represented is also important in terms of the prior information required to apply the filter. For acoustic noise only, Eq. (3.33) can be written as

$$\hat{A}(\omega) = \frac{F(\omega)\, H^*(\omega)}{|H(\omega)|^2 + \dfrac{E[n_a^2(\omega)]}{E[A^2(\omega)]}} \tag{3.37}$$

There is a subtle distinction between Eq. (3.36) and Eq. (3.37). The implication of Eq. (3.36) is that $E[A_a^2(\omega)]$ must be determined in order to apply the filter. Since general procedures for determining $H_a(\omega)$ have not been established, application of the filter as stated in Eq. (3.36) would very difficult. Equation (3.37) shows that the filter can be applied with knowledge of the average power, $E[n_a^2(\omega)]$, associated with acoustic noise in its measured form.

CHAPTER IV. EXPERIMENTAL PROCEDURES

With the derivation of the optimal Wiener filter complete, the task reduces to evaluation of scattering amplitude and noise as random variables in Chapter V and evaluation of the application of the optimal Wiener filter in Chapter VI. The current chapter deals with the acquisition and preliminary treatment of the flaw signals and noise signals on which the work presented in Chapters V and VI is based. This chapter is organized into three sections which involve 1) choice and preparation of samples, 2) measurement of signals, and 3) processing and presentation of the data.

In order to study the optimal Wiener filter under a variety of conditions (i.e., for different noise types, signal to noise ratios, flaw distribution breadths, etc.), families of noise-corrupted flaw signals must be available. A number of practical considerations prohibit using realistic flaws in acoustically noisy engineering materials in order to create families of noise-corrupted flaw signals. These factors include: 1) difficulties associated with the fabrication of known flaws in engineering materials (Hsu and Thompson 1988); 2) inability to vary the frequency dependence of the acoustic noise without changing the host material; and 3) inability to vary the S/N without changing the host or flaw material. In order to overcome these problems, a novel approach was adopted in which flaw signals (essentially noise-free flaw signals) and noise signals were measured separately and then digitally superimposed in the computer to create noise-corrupted flaw signals. This approach allows: 1) the simulation of any number of noise-corrupted flaw signals

using experimentally measured acoustic noise; 2) studying the filter for flaw distributions with various means and breadths, respectively; 3) studying the filter for flaw signals corrupted with different types of noise; and 4) studying the filter for various signal to noise ratios for each type of noise.

Samples

Flawed samples

A limited set of samples were fabricated using polystyrene spheres (ρ_{ps}=1.05g/cc, c^L_{ps}=0.235cm/μs, and c^T_{ps}=0.118cm/μs) as the flaw material and thermoplastic (Buehler's transoptic: ρ_{tp}=1.18g/cc, c^L_{tp}=0.272cm/μs, and c^T_{tp}=0.135cm/μs) as the host material. This represents a weak scattering combination with a reflection coefficient (Eq. (2.6)) of 0.13. The primary reasons that this flaw/host combination was chosen were: 1) thermoplastic is acoustically isotropic and homogeneous (i.e., there are no internal scattering sites which would yield acoustic noise); 2) a forward solution can be determined for a polystyrene sphere in thermoplastic; 3) flawed samples can be economically fabricated in a reasonable length of time; 4) the position of the flaw in each sample can be approximately controlled; 5) the flaws can be optically located and sized after fabrication; and 6) flaw scattering details can be estimated with some confidence.

A set of 10 flawed samples was fabricated with flaw diameters in the range from 100μm to 350μm. The samples were disks (diameter~1.25" and thickness~0.5") with the flaw placement at an approximate depth of 0.25".

Due to the difficulties associated with handling elastic objects in the 200μm size range, approximately 30 polystyrene spheres were cast in thermoplastic samples in order to get the final 10 flaws. Three blanks (i.e., samples without flaws) were also cast. General procedures for casting thermoplastic samples are described in section 3 of the "Buehler Analyst" which is published by Buehler. The basic concept is that under heat and pressure (in a Buehler pneumatic mounting press), transoptic powder becomes a transparent plastic. Casting a thermoplastic sample with an embedded polystyrene sphere involved special procedural steps including: 1) the casting equipment was carefully cleaned (any contaminant would represent an acoustic inhomogeneity in the sample and could cause scattering when interrogating a polystyrene sphere); 2) the first half of the powder was placed in the casting cylinder and the powder was then compressed to establish an even surface on which the sphere could be placed; 3) the sphere was carefully placed in the cylinder in approximately the desired location; and 4) the second half of the powder was placed in the cylinder without allowing the added powder to dislodge the sphere.

It was desirable to have the flaw depth (i.e., the distance between the front surface of the sample and the flaw) approximately the same for each flaw so that the measurement system response, $H(\omega)$, would be the same for each flaw. Therefore, the initial depth of each flaw was estimated ultrasonically, and the samples were then machined so that the flaw depth was approximately the same for each of the 10 flaws. The depth of each flaw was estimated by utilizing the longitudinal wave speed in thermoplastic (c_{tp}^{L}=0.272cm/μs) and the time of flight from the leading

edge of the reflection at the front surface of the sample to the leading edge of the signal from the flaw. In order to remove machining marks, each sample was sanded and then polished on the lathe using a polishing cloth and Linde A polishing powder. For reasons discussed later in this chapter, one of the blank samples was machined (and polished) to a thickness approximately equal to the average depth of the 10 flaws. This sample will be referred to as the reference disk.

Noise samples

Samples were chosen in order to allow the measurement of backscattered noise from samples with different internal scattering sites (i.e., grains versus pores) and in order to attain noise signals with differing power spectra (i.e., low frequency versus high frequency noise). The noise measured from the samples will be referred to as case 1 acoustic noise, case 2 acoustic noise, and case 3 acoustic noise, respectively. The nature of the material sample associated with each case is as follows:

case 1 acoustic noise sample - stainless steel with an average grain size of 22.5μm (ASTM 8);

case 2 acoustic noise sample - stainless steel with an average grain size of 62.5μm (ASTM 5); and

case 3 acoustic noise sample - aluminum with approximately 2% porosity (average pore radius ≈ 164μm (Hsu et al. 1986)).

As indicated below in the measurement procedures section, case 1 acoustic noise and case 3 acoustic noise were measured with a planar transducer while case 2 acoustic noise was measured with a focused transducer.

Therefore, each acoustic noise case is unique due to the difference in scattering phenomenon associated with grain scattering (Mason and McSkimin 1947, Papadakis 1968, Goebbels 1980, Stanke 1983, Stanke and Kino 1984) versus pore scattering (Gubernatis and Domany 1983, Thompson et al. 1983a, Thompson et al. 1983b, Rose 1985) and due to the difference in the interrogating wave fields for a planar transducer and a focused transducer.

Measurement Procedures

General measurement considerations

Figure 4.1 shows a schematic representation of the system used to make ultrasonic measurements (Hsu et al. 1986). Standard pulse/echo measurement techniques were used in making ultrasonic measurements (Krautkramer and Krautkramer 1977, Fitting and Adler 1981). The operation of the digitizer and the digital signal processing steps which immediately follow the digitization of a time domain wave are given in the following paragraph.

The time interval over which a signal is digitized will be referred to as the measurement interval. The measurement interval length and starting time relative to the initial excitation of the transducer can be set so that the desired portion of a signal is digitized. Within the measurement interval, the Textronix 7912AD digitizer (Fig. 4.1) determines the signal with a 512x512 resolution. For all measurements discussed here, the measurement interval length, T, was chosen as 2μs. At T=2μs and with 512 points of resolution, the time between points, ΔT, equals 3.9ns

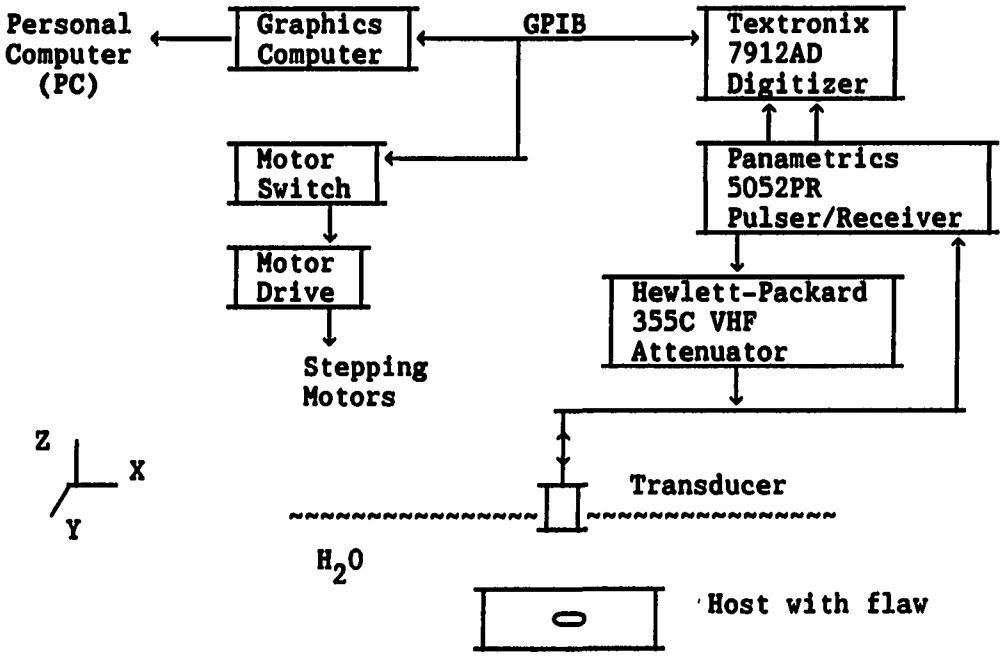

Figure 4.1. Measurement system schematic.

and the Nyquist frequency (Beauchamp and Yuen 1979) equals 128MHz ($1/2\Delta T$). In order to reduce electronic noise contributions, as a general procedure the digitizer determines the output as the average over 64 pulses. The resultant output can be written as

$$D(t_i) = \frac{1}{64} \sum_{k=1}^{64} D(t_i, T_k) \qquad (4.1)$$

where the parameter T_k represents the k^{th} pulsing of the transducer and $D(t_i, T_k)$ is the integral value between 1 and 512 at the i^{th} time for the k^{th} pulsing of the transducer. In order to create a zero-mean output signal in units of volts, the following signal processing steps are then carried out in the graphics computer (Fig. 4.1): 1) the average of the

512 amplitudes is determined; 2) this average is subtracted from the value at each of the 512 positions; and 3) the result is scaled to convert the signal amplitude into volts. In equation form, the output voltage at the i^{th} time, $V_o(t_i)$, can be written as

$$V_o(t_i) = C \left[D(t_i) - \frac{1}{512} \sum_{i=1}^{512} D(t_i) \right] \qquad (4.2)$$

where C is the scale factor used to convert the output to volts. The operation of the digitizer as represented by Eq. (4.1) and the signal processing steps as represented by Eq. (4.2) will be referenced later. It is to be emphasized that these steps are specific to the ultrasonic measurement system and procedures used in this work.

Reference signal measurement

In association with the measurement of flaw signals, a reference signal was measured. The reference signal was used in estimating the measurement system response as discussed later in this chapter. The reference experiment and flaw experiment measurements were made with a 15MHz focused transducer (1/2" diameter, 3" focal length in water). Use of a focused transducer was necessitated due to the weak scattering nature of polystyrene in thermoplastic. Pulser/receiver and attenuator (Fig. 4.1) settings for the reference experiment and flaw experiment were the same as the settings given in Table 4.1 on page 76 for electronic noise.

The reference experiment involves measuring the back surface reflection from the thermoplastic reference disk. Experimental measurement procedures are as follows:

1. Place the reference disk on spacer blocks in the water tank with the water path at ~7cm. The spacer blocks are used in order to assure that the disk is surrounded by water over the areas which will be interrogated.
2. Set the time scale at 10μs/div so that both the trigger signal sent form the pulser/receiver to the digitizer and the front surface reflection are within the measurement interval.
3. Approximately normalize the transducer axis to the face of the disk by maximizing the front surface reflection. Note that after the transducer is focused on the back surface of the disk (step 4), the transducer will be normalized based on the back surface reflection.
4. Using the time delay between the front surface reflection and the trigger signal along with the longitudinal wave speed in water (c_w^L=0.148cm/μs), set the water path at 6.74cm. Per Eq. (4.3) stated below, this water path approximately focuses the transducer on the back surface of the disk.
5. Set the time scale at 50ns/div and set the measurement interval starting time so that only the back surface reflection is within the interval. Adjust the receiver attenuation to assure that the receiver amplifier is not saturated. This was achieved at a 10dB attenuation setting.
6. Set the time scale at 200ns/div and normalize the transducer by maximizing the back surface reflection.
7. Center the back surface reflection within the measurement interval, digitize the back surface reflection at 64 averages

(Eq. (4.1)), and transfer the signal to the PC (Fig. 4.1). This measured reference signal will be denoted $F_R^a(t)$ where the superscript indicates that the received signal was attenuated at the pulser/receiver.

8. Set the time scale at 500ns/div and set the measurement interval starting time so that both the front and back surface reflections are within the interval. Using the time delay between the two reflections along with c_{tp}^L, estimate the thickness of the disk. The recorded thickness was 0.48cm.

The required water path to focus the transducer at a given depth in thermoplastic was approximated as

$$d_w = f_w - \frac{c_s}{c_w} d_s \tag{4.3}$$

where d_w=water path, f_w=focal length in water, c_s^L=longitudinal wave speed in the solid (thermoplastic), c_w^L=longitudinal wave speed in water, and d_s=solid path. Equation (4.3) is determined based on geometric consideration and does not account for diffraction effects; therefore, the true focal point is slightly closer to the transducer than predicted.

In principle, the reference signal could be corrected for the 10dB attenuation introduced at the receiver by simply multiplying the measured signal by 3.16 ($10dB=20Log_{10}(3.16)$). That is, the corrected reference signal in the frequency domain, $F_R(\omega)$, would be equal to $3.16F_R^a(\omega)$. In practice, for the system used, the attenuation introduced at the 10dB setting on the pulser/receiver is frequency dependent. In order to determine a frequency dependent attenuation correction, the signal from

one of the flaws was measured (per the general procedures stated below) with the pulser/receiver attenuation set at 0dB and also at 10dB. A straight line was then fit through the ratio of $|F(\omega)|_{0dB}$ to $|F(\omega)|_{10dB}$. The result of this procedure was essentially a filter, denoted $W_a(\omega)$, which increases linearly with frequency and has a value of 3.16 at approximately 7MHz. The corrected reference signal was determined as

$$F_R(\omega) = W_a(\omega)\ F_R^a(\omega) \tag{4.4}$$

where $F_R(\omega)$ is used later in estimating the measurement system response.

Flaw signal measurement

Flaw signals were measured immediately following the reference experiment. Flaw signal measurement procedures are as follows:

1. Place the flawed disk on the spacer blocks with the flaw approximately under the transducer.
2. Set the time scale at 10μs/div. Using the time delay between the trigger signal and the front surface reflection and c_w^L, set the water path at 6.74cm.
3. Set the time scale at 1μs/div, the vertical scale at maximum sensitivity, and the receiver attenuation at zero. Set the measurement interval starting time so that both the front and back surface reflections are within the interval. Turn the threaded rods which control the x-y position of the transducer in order to scan the disk until the flaw signal is visible between the front and back surface reflections.

4. Set the time scale at 200ns/div and center the flaw signal with the measurement interval. Carefully turning the threaded rods by hand, maximize the flaw signal. A maximized flaw signal has a maximum amplitude of approximately 1/3 of full scale and a time duration of approximately 1/3 of the measurement interval length. Note that the x-y stepper motors are not used since the step size, 2.5mil (63.5μm), is too large relative to the flaw size.
5. With the receiver attenuation at zero, digitize the flaw signal at 64 averages (Eq. (4.1)) and transfer the signal to the PC (Fig. 4.1).
6. Set the time scale at 500ns/div and set the measurement interval starting time so that both the front surface reflection and the flaw signal are within the interval. Using the time delay between the signals and c_{tp}^{L}, estimate the flaw depth.

These steps were followed for each flaw resulting in a set of 10 measured flaw signals.

Noise signal measurement

Electronic noise Electronic noise was measured following the measurement of the last flaw signal. In order to measure electronic noise which is representative of that noise which corrupts flaw signals, all acoustic signals must be eliminated from the measurement interval while not changing any of the measurement conditions. This was done by moving the transducer horizontally until the transducer was off of the sample, thus eliminating all reflected and scattered signals from the sample. Thirty-six (36) signals were then digitized and transferred to the PC

(Fig. 4.1). Instrument settings are summarized in Table 4.1 on page 76. Each signal was determined at 64 averages (Eq. (4.1)) and can be represented as

$$n_e(t,\zeta_1,T) = \frac{1}{64} \sum_{k=1}^{64} n_e(t,\zeta_1,T_k) \qquad (4.5)$$

where 1) T_k represents the k^{th} pulsing of the transducer; 2) ζ_1 is used to emphasize that the signals were measured from only one ultrasonic system (see the stochastic model discussion section in Chapter II); and 3) the parameter, T, is included in $n_e(t,\zeta_1,T)$ to emphasize that the signals vary over pulses of the transducer.

Acoustic noise Measurement of acoustic noise is now considered starting with general procedures which are independent of the type of acoustic noise to be measured. In measuring acoustic noise, unflawed samples were utilized and backscattered noise signals were measured at a number of locations representing a grid pattern for each type of acoustic noise considered. At each grid position, the backscattered signal contains all of the components of a flaw signal except contributions due to scattering at the flaw. Therefore, the measured signals will include electronic noise and may also contain a contribution due to the front surface reflection (Elsley and Addison 1981, Addison et al. 1982). This late arriving portion of the front surface reflection is thought to be due primarily to ringing of the transducer. In the system used here, the ringing noise is a low frequency noise with its greatest strength near the lower limit of the bandwidth (i.e., in the 2MHz range). Given the importance of low frequency information in some flaw characterization

approaches (Richardson and Elsley 1979, Richardson 1980, Richardson and Elsley 1980, Elsley et al. 1981, Richardson 1984) and in scattering amplitude estimation outside of the bandwidth at low frequencies (Addison et al. 1982, Gray 1982, Thompson and Gray 1982, Cohen-Tenoudji et al. 1984, Clark et al. 1986, Neal and Thompson 1987, Koo 1988), successful elimination of the ringing noise can be critical. However, the significance of this component depends on a number of factors including the pulser/receiver (and the settings used), transducer, host material, flaw depth, and flaw signal strength. General procedures for handling front surface reflection contributions are outlined below in the signal processing section.

For simplicity, the transducer ringing noise will be referred to as ringing noise and will be denoted by $n_r(t)$. With the ringing component included, the backscattered noise signal measured at the i^{th} grid position can be represented as

$$n^r(t,\zeta_i) = n_a(t,\zeta_i) + \bar{n}_e(t,\zeta_i) + n_r(t) \qquad (4.6)$$

where the measured signal is written with the superscript, r, to indicate that the signal includes ringing noise, and $\bar{n}_e(t,\zeta_i)$ is used to indicated that electronic noise has been reduced by averaging over 64 pulses (Eq. (4.1)). The measured signal is written without a subscript since it involves more than just acoustic noise. Note that the ringing component is independent of the grid position, ζ_i.

Table 4.1 summarizes pertinent experimental conditions for each noise type. Note that case 1 acoustic noise and case 3 acoustic noise were measured using a 1/2" diameter, 15MHz, planar transducer while case 2

Table 4.1. Noise measurement condition summary

	Electronic noise	Acoustic noise		
		Case 1	Case 2	Case 3
Number of signals measured	36	49	36	27
Transducer type planar	-	planar	focused	
Host material aluminum	-	stainless (ASTM 8)	stainless (ASTM 5)	
Host density (g/cc)	-	7.9	7.9	2.6
Host L-wave speed (cm/μs)	-	0.58	0.58	0.63
Host T-wave speed (cm/μs)	-	0.31	0.31	0.30
Measurement (grid) spacing (cm)	-	0.63	0.13	0.30
Water path (cm)	-	9.01	2.2	8.95
Measurement depth (cm)	-	~1.1	~0.58	~1.2
HP attenuator:				
in/out of circuit	in	out	in	out
attenuation setting (dB)	6	-	6	-
Panametrics settings:				
energy	2	1	2	1
attenuation (dB)	0	50	0	14

Panametrics settings for all measurements:

damping: 0 high pass filter: 1.0 gain: 40 repetition rate: minimum

acoustic noise was measured with the same transducer used to measure the reference signal and the flaw signals (i.e., a 1/2" diameter, 15MHz, focused transducer with a 3" focal length in water). The measurement depth indicates the approximate depth into the plate for the start of the measurement interval. Case 1 acoustic noise and case 3 acoustic noise were measured using one Panametrics pulser/receiver and electronic noise and case 2 acoustic noise were measured at later date using a different Panametrics pulser/receiver. Also, case 1 acoustic noise and case 3 acoustic noise were measured without the HP attenuator in the transmit side of the circuit. The electronic noise and case 2 acoustic noise were measured with the HP attenuator in the circuit.

Processing and Presentation of Data

Flaw signals

Time domain gating One of the first signal processing steps associated with flaw signature estimation is to eliminate noise within the measurement interval which does not occur at the same time as the flaw signal (Addison et al. 1982). This procedure involves estimating the duration of the flaw signal in time and then gating or windowing out all noise within the measurement interval which occurs before or after the flaw signal. Here, the flaw signal duration is estimated and the signal is truncated (i.e., set equal to zero) at all times outside of the flaw signal. This is equivalent to multiplying the signal by a rectangular window (Addison et al. 1982). The truncation is started at the nearest zero-crossings to the beginning and end, respectively, of the flaw signal.

Truncation was started at zero-crossings in order to avoid introducing abrupt changes in the time domain signal which would result in artifacts in the frequency domain. Time domain windowing procedures were also considered but were not found to be superior to the zero-crossing truncation approach.

Measurement system response estimation Regardless of the flaw signature estimation technique to be utilized, a necessary preliminary step involves estimation of the measurement system response, $H(\omega)$ (see the review of estimation techniques given in Chapter II). For the flaw experiments described above, $H(\omega)$ was estimated following the work of Thompson and Gray (1983). An alternative approach to that of Thompson and Gray has recently been proposed by Koo (1988).

In order to avoid explicitly determining the individual terms which make up $M(\omega)$ (see Eq. (2.14)), the output of the reference experiment described above was utilized to estimate $M(\omega)$ as a whole. By utilizing the same instrument settings and transducer for the reference experiment and flaw experiment, $M(\omega)$ will be the same for both experiments. The output of the reference experiment, $F_R(\omega)$, can be represented by the convolution of $M(\omega)$ with propagation effects associated with the reference experiment, $P_R(\omega)$, plus noise

$$F_R(\omega) = M(\omega)\, P_R(\omega) + n(\omega) \tag{4.7}$$

Given an estimate, $\hat{P}_R(\omega)$, of the reference experiment propagation effects, an estimate of $M(\omega)$ could be determined as

$$\hat{M}(\omega) = \frac{F_R(\omega)}{\hat{P}_R(\omega)} \tag{4.8}$$

Combining this estimate with an estimate of the flaw experiment propagation effects, $\hat{P}_f(\omega)$, an estimate of the measurement system response could be determined as

$$\hat{H}(\omega) = \hat{M}(\omega)\ \hat{P}_f(\omega) = F_R(\omega) \left[\frac{\hat{P}_f(\omega)}{\hat{P}_R(\omega)} \right] \tag{4.9}$$

where the estimate involves errors due to estimation of the propagation effects and reference experiment noise.

As demonstrated by Eq. (4.10), given the reference signal, $F_R(\omega)$, the problem of estimating $H(\omega)$ reduces to estimating the ratio of the propagation effects associated with the flaw experiment to the those associated with the reference experiment. Performing the reference and flaw experiments as described above with the same transducer, instrument settings, water paths, and with a reference disk at a thickness equal to the flaw depth, reduces the problem to finding the ratio of the diffraction terms (Thompson and Gray 1982, Thompson and Gray 1983).

Origin of time estimation In order to explain the origin of time concept, reconsider a Born scatterer as discussed in Chapter II. Referring to Fig. 2.2.a, when the origin of time is taken to be coincident with the centroid of the flaw (i.e., midway between the front and back surface reflections), the impulse function, R(t), is an even function of time and the Fourier transform of R(t) yields a purely real scattering amplitude, $A(\omega)$, as shown in Fig. 2.2.c. If the origin of time is

displaced by an amount τ, then R(t) contains a time-shift error, as represented by $R(t+\tau)$, and is no longer an even function of time. Consequently, the Fourier transform of $R(t+\tau)$ yields a scattering amplitude which contains a phase error as represented by $A(\omega)\exp(i\omega\tau)$. Since many flaw characterization techniques are sensitive to time-shift or phase errors, the correct origin of time must be estimated either prior to or as a part of the flaw signature estimation process. Therefore, as a preliminary step in studying the application of the optimal Wiener filter to measured flaw signals, the measured signals must be shifted to the estimated origin of time.

A variety of methods for estimating the origin of time have been investigated (Richardson and Elsley 1980, Chaloner and Bond 1987, Bond et al. 1987, Bond et al. 1988). Weak scatterers (a polystyrene sphere in thermoplastic is a weak scatterer) lend themselves to a number of origin of time estimation approaches. In particular, the area function method (Thompson and Gray 1982, Gray 1982) can be correctly applied only to weak scatterers. In addition, a method for estimating the origin of time for weak scatterers which utilizes an inverse Born radius versus time shift domain (Addison et al. 1982) has been recently introduced by Bond et al. (1988). Both of these methods were investigated and gave virtually identical results to the method which was actually applied. This method is described below.

The method of estimating the origin of time used here relies on the prior knowledge which was available having fabricated the flawed samples under controlled conditions. The basic idea is to shift the measured flaw signal to be in alignment with a calculated flaw signal for the same size

flaw. This was actually done in the impulse response domain by shifting an estimate of the impulse response function, $\hat{R}(t+\tau)$, determined from the measured flaw signal until it aligned with the calculated impulse response function, R(t). Since polystyrene spheres in thermoplastic are weak scatterers, the impulse response functions show two dominant peaks which correspond to the front and back surface reflection from the flaw (as an example of $\hat{R}(t)$ after shifting and R(t), see Fig. 4.1.a on page 89). Therefore, it was possible to align the estimated impulse response functions with calculated impulse response functions with the same spacing between dominant peaks.

The first step in the procedure was to generate a table, based on calculated impulse response functions, which contains flaw radii, the time between dominant peaks (i.e., the time between front and back surface reflections), denoted Δt here for discussion purposes, and the time corresponding to the maximum peak, t_{max}. This was done for flaw radii from 55μm to 165μm in 1μm increments as follows:

1. Calculate $A(\omega)$ using the Ying and Truell (1956) solution approach.
2. Apply the desensitization filter algorithm (as defined in Chapter II, pp. 43-46) to $A(\omega)$. That is, multiply $A(\omega)$ by the filter term, $W(\omega)$, extrapolate at low frequencies, and window at high frequencies. Note that $\hat{H}(\omega)$ determined as described above was used in $W(\omega)$.
3. Take the IFT of the result to determine a calculated impulse response function, R(t), which reflects the limitations of the desensitization filter algorithm.

4. Determine Δt (the spacing between the front and back surface reflections).
5. Determine t_{max} (the time corresponding to the maximum peak).
6. Store the flaw radius, Δt, and t_{max}.

For each of the 10 flaws, the time shift, τ, was then estimated as follows:

7. Apply the desensitization filter algorithm to the measured flaw signal. The result of the algorithm is a scattering amplitude estimate with a phase error as represented by $\hat{A}(\omega)\exp(i\omega\tau)$.
8. Take the IFT of $\hat{A}(\omega)\exp(i\omega\tau)$ to determine an impulse response estimate, $\hat{R}(t+\tau)$.
9. Determine Δt (see step 4).
10. Determine t_{max} (see step 5).
11. Search through the table generated as described above for the flaw radius whose Δt is equal to Δt for $\hat{R}(t+\tau)$.
12. Estimate τ as the difference between t_{max} for $\hat{R}(t+\tau)$ and t_{max} for $R(t)$ corresponding to the radius determined in step 11.
13. Apply this time shift to the measured flaw signal to position the measured signal such that it has approximately the correct origin of time.

Note that in step 11 an estimate of the flaw radius has been determined.

Sizing The goal here is to determine a size for each flaw which will be used as the "right answer" in studying the optimal Wiener filter. A number of sizing approaches were utilized as described below.

Each flaw was optically sized by viewing through the polished side of the sample. The flaws were sized using a Zeiss microscope at a nominal

Table 4.2 Flaw size data

Flaw #	Optical radius (um)	Acoustic radius (um)	Inverse Born Approximation radius (um)
1	65	62	52
2	85	77	76
3	95	90	91
4	103	97	98
5	113	109	107
6	125	118	118
7	140	130	131
8	143	135	136
9	164	144	149
10	171	156	161

magnification of 256X. The scope was calibrated by adjusting the magnification until the scale embedding in the scope was at 4μm/div according to a stage micrometer. At 4μm/div and given the difficulties associated with focusing on the central plane of a spherical object, it was estimated that the optical sizes were accurate to ±4μm. Under high magnification, it was apparent that some of the flaws were not perfectly spherical. The largest out-of-roundness optically measured was approximately 3%. The "optical size" of each flaw is given in Table 4.2. Where an out-of-roundness was observed, an average size is stated. Note

that since the ultrasonic flaw signal is dominated by a front surface reflection followed by a back surface reflection, the signal is indicative of the size of the flaw along the direction of interrogation. Conversely, the optical size represents the radius of a circle which is normal to the direction of ultrasonic interrogation. Therefore, since the flaws are not perfectly spherical, the optical size may not be representative of that size which would be sensed by an ultrasonic experiment.

The size was also determined acoustically based on matching the Δt between dominant peaks in $\hat{R}(t)$ with that for $R(t)$. This was done automatically as part of the origin of time estimation procedure described above (step 11). The basic idea was to determine the size of flaw whose calculated impulse response function showed a spacing between the front and back surface reflection at the flaw which was equal to the spacing in the impulse response function estimated from the measured flaw signal. The estimated size resulting from this procedure will be referred to as the "acoustic size". The acoustic size of each flaw is given in Table 4.2. This size essentially determines the size of polystyrene sphere in thermoplastic whose calculated impulse response function "best" approximates $\hat{R}(t)$ for the flaw being considered (given that there are numerous errors involved including ultrasonic measurement errors, errors in $\hat{H}(\omega)$, and given that the flaws are not perfectly spherical).

The size was also estimated using the inverse Born approximation (IBA) (Rose and Krumhansl 1979). Radius estimates determined via the IBA are also used in Chapter VI as a filter analysis tool. Application of the IBA, involves estimation of the characteristic function, $\gamma(r)$, of the flaw which is defined such that $\gamma(r)=0$ inside the flaw and $\gamma(r)=1$ outside the

flaw. For flaws with spherical symmetry, the IBA determines the characteristic function as (Rose and Krumhansl 1979)

$$\gamma(r) = \text{constant} \int_0^\infty \text{Re}(A(k)) \frac{\sin(2kr)}{2kr} dk \qquad (4.10)$$

where $k=\omega/c$. Given an estimate of $\gamma(r)$ determined from bandlimited data, an estimate of the flaw radius is commonly determined either 1) as the value of r at which $\gamma(r)$ is equal to half of its peak value, or 2) by integrating the estimate of $\gamma(r)$ over r and then dividing the result by the peak value of $\gamma(r)$.

As is typically done (Gray 1982, Thompson and Gray 1982, Thompson et al. 1986), $\hat{A}(\omega)$ determined via the desensitization algorithm (see Chapter II, pp. 43-46) was used as a basis for estimating the characteristic function, and radius estimates were determined via the first method stated above. Using this approach, the "IBA size" of each flaw was determined. These sizes are given in Table 4.2.

Comparison with calculated results The acoustic size was taken to be the most representative estimate of size of each sphere. Again, this size represents the flaw whose calculated signature "best" represents the experimental result. In this section, scattering amplitude and impulse response estimates determined via the desensitization algorithm (see steps 7 and 8 in the origin of time estimation section) are compared to calculated results which have been identically processed (see steps 1-3 in the origin of time estimation section). By bandlimiting, extrapolating, and windowing the calculated scattering amplitude, the difference between the scattering amplitudes represents experimental and modeling errors.

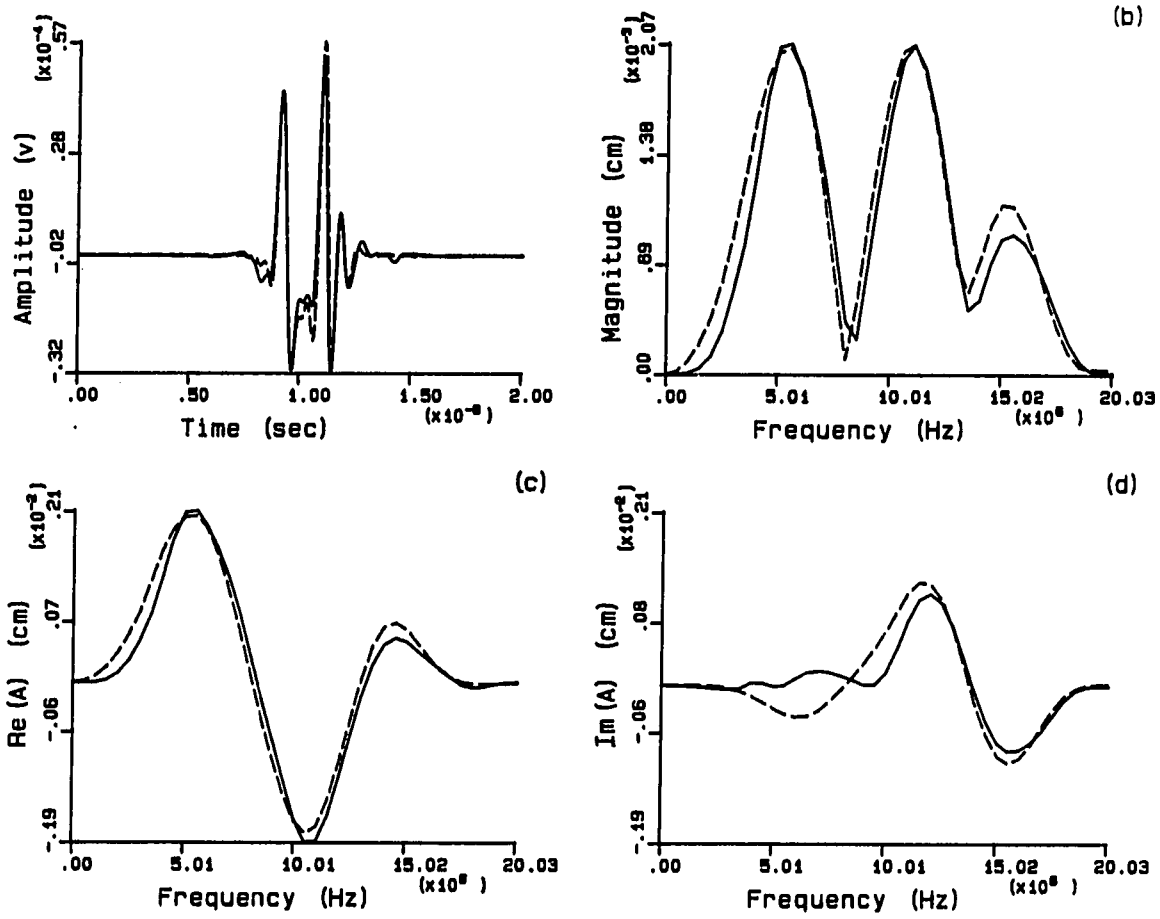

Figure 4.2. Comparison: estimated versus calculated R(t) and A(ω). a) R(t) (dashed), $\hat{R}(t)$ (solid); b) $|A(\omega))|$ (dashed), $|\hat{A}(\omega)|$ (solid); c) Re[A(ω)] (dashed), Re[$\hat{A}(\omega)$] (solid); d) Im[A(ω)] (dashed), Im[$\hat{A}(\omega)$] (solid)

Table 4.3 Error summary: estimated versus calculated $A(\omega)$

Flaw #	Acoustic radius (cm)	e_{Re}	e_{Im}	$e_{Re,Im}$
1	62	0.13	1.25	0.69
2	77	0.08	1.21	0.65
3	90	0.13	0.65	0.39
4	97	0.08	0.66	0.37
5	109	0.17	0.43	0.30
6	118	0.21	0.19	0.20
7	130	0.25	0.19	0.22
8	135	0.36	0.35	0.35
9	144	0.23	0.35	0.29
10	156	0.22	0.32	0.27

Figure 4.2 shows a typical comparison between flaw signature estimates determined via the desensitization filter algorithm (solid lines) and calculated flaw signatures (dashed lines) identically processed. This example is for the 109μm radius flaw. A quantitative comparison for all 10 flaws is given in Table 4.3 in terms of a normalized average squared-error. For the k^{th} flaw, the error is defined for the real part of the scattering amplitude as

$$e_{Re}(\zeta_k) = \frac{\frac{1}{M}\sum_{i=1}^{M}\left[\,Re[\hat{A}(\omega_i,\zeta_k)]-Re[A(\omega_i,\zeta_k)]\,\right]^2}{\frac{1}{M}\sum_{i=1}^{M}\left[\,Re[A(\omega_i,\zeta_k)]\,\right]^2} \qquad (4.11)$$

where M was chosen such that the error was calculated over the frequency range from 0 to f_{max} (the upper bandlimit as defined in Chapter II relative to the desensitization filter algorithm). Errors for the imaginary part, e_{Im}, were similarly calculated. The error $e_{Re,Im}$ is defined as

$$e_{Re,Im} = \frac{1}{2}\left[\, e_{Re} + e_{Im} \,\right] \qquad (4.12)$$

and represents the average of e_{Re} and e_{Im}.

Noise signals

Ringing estimation In this section, procedures for estimating and subtracting the ringing noise are stated. Since this component does not change with grid position, it represents a coherent noise source which, in principle, can be estimated and then subtracted from the measured signal (Elsley and Addison 1981, Addison et al. 1982, Gray 1982). In order to remove the ringing component from the noise signals, the ringing component is estimated by averaging the measured signals over the grid positions and the estiamte is then subtracted from each signal. This procedure is complicated due to phase errors in the measurement process. The phase error exists since the distance from the transducer face to the front surface of the plate (the water path) will be different for each grid position (Gray 1982). This water path difference exists since the

transducer cannot be moved exactly parallel to the front surface of the plate. In the measurement procedure used here, the phase error was minimized by carefully leveling the plate and by using the z-motor (Fig. 4.1) to correct for the water path differences at each position.

The ringing component estimate is determined by averaging over the grid positions and can be represented as

$$\hat{n}_r(t) = \frac{1}{N} \sum_{i=1}^{N} [n_a(t,\zeta_i) + \bar{n}_e(t,\zeta_i) + n_r(t)] \tag{4.13}$$

where N is the number of grid positions (denoted the number of signals measured in Table 4.1). This estimate reduces to the sum of the ringing component and sample averages of acoustic and electronic noise and can be written as

$$\hat{n}_r(t) = \bar{n}_a(t) + \bar{n}_e(t) + n_r(t) \tag{4.14}$$

where electronic noise has been averaged over time intervals (Eq. (4.1)) and over grid positions (Eq. (4.13)). The final noise signal which is stored for analysis is determined by subtracting $\hat{n}_r(t)$ from the measured signal (Eq. (4.6)) yielding

$$n(t,\zeta_i) = n_a(t,\zeta_i) + \bar{n}_e(t,\zeta_i) + n_r(t) - \hat{n}_r(t) \tag{4.15}$$

With electronic noise significantly reduced by averaging and with the ringing elimination procedure followed, the final signal is essentially equal to the backscattered acoustic noise associated with a given grid position.

Example noise signals and power spectra Shown in Fig. 4.3.a is a typical measured electronic noise signal as represented by Eq. (4.5). The rapidly varying signal in Fig. 4.3.b represents case 1 acoustic noise as measured ($n^r(t,\zeta_i)$ as given in Eq. (4.6)). The low frequency trace running through the noise signal in Fig. 4.3.b is the estimated ringing component ($\hat{n}_r(t)$ as given in Eq. (4.14)) for case 1 acoustic noise. Figure 4.3.c shows the signal with the ringing component subtracted out as given in Eq. (4.15). This example represents a case where the ringing component is significant. The figures clearly show the ringing and the improvement associated with subtraction of the ringing. Figures 4.3.d and 4.3.e are typical noise signals for case 2 acoustic noise and case 3 acoustic noise, respectively. Note that the noise signals shown in Figures 4.3.b-e are dominated by acoustic noise and the high frequency contributions typical of electronic noise (Fig. 4.3.a) are minimal.

The average power at each frequency for each type of acoustic noise is shown in Fig. 4.4 (Neal and Thompson 1986). Figure 4.4.a demonstrates the effect of ringing noise subtraction for case 1 acoustic noise. The dashed line in the figure represents the average noise power without subtraction of the ringing noise, and the solid line shows the average power with the ringing subtracted. As previously indicated (Fig. 4.3), the ringing component is strong at low frequencies, and it is quite significant for this case. Figures 4.4.b, 4.4.c, and 4.4.d show the average power for case 1 acoustic noise, case 2 acoustic noise, and case 3 acoustic noise, respectively. In each case the curves have been smoothed via a three point running average. The shape of each plot is influenced by both the effective measurement system response, $H_a(\omega)$, and by the

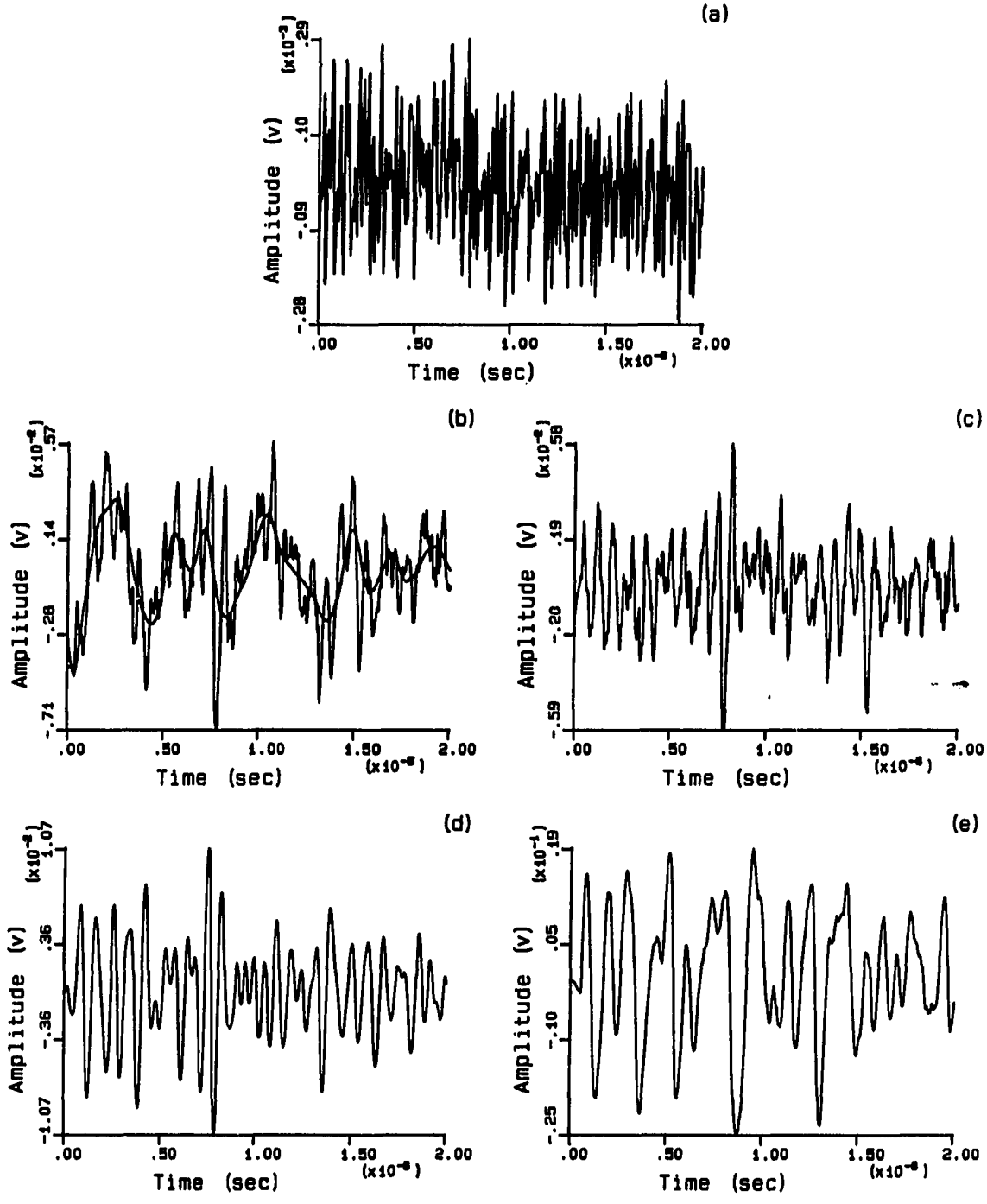

Figure 4.3. Time domain noise signals. a) electronic noise; b)-e) acoustic noise: b) case 1 prior to ringing noise subtraction and ringing component; c) case 1 after subtraction; d) and e) case 2 and case 3, respectively, after ringing subtraction

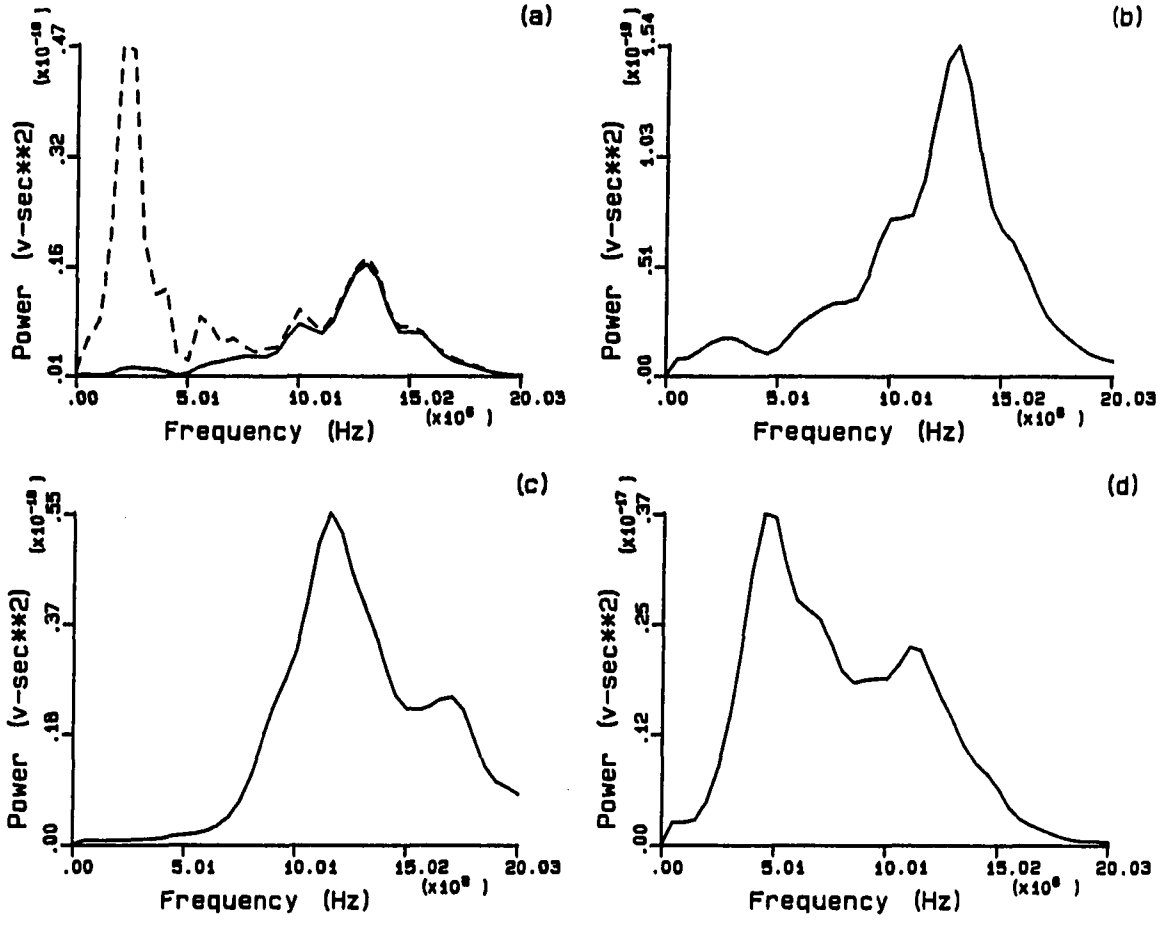

Figure 4.4. Acoustic noise average power. a) effect of ringing noise subtraction (case 1); b)-d) average power spectra for case 1, case 2, and case 3, respectively

effective scattering amplitude associated with the dominant scattering source, $A_a(\omega)$. In particular, the measurement system response is evident as it forces case 1 acoustic noise and case 2 acoustic noise to fall off at high frequency. The rise at low frequency for case 3 acoustic noise is also indicative of the measurement system response. As can be seen, case 1 and case 2 acoustic noise have strength at intermediate to high frequencies within the bandwidth while case 3 acoustic noise has its

strength at low to intermediate frequencies. The average power for the porous aluminum (case 3 acoustic noise) was used by Hsu et al. (1986) to estimate the percent porosity associated with the aluminum specimen.

CHAPTER V. RANDOM VARIABLE ANALYSIS

This chapter deals with the analysis of scattering amplitude and noise as random variables. Well established random variable analysis techniques are utilized to evaluate the assumptions made in the derivation of the filter (Chapter III) and to establish noise and scattering amplitude means and variances which are used in applying the filter (Chapter VI). Note that while the random variables were assumed to be uncorrelated, Gaussian random variables to facilitate the derivation, only estimates of the mean and variance associated with $A(\omega)$ and $n(\omega)$, respectively, are required in order to apply the filter. The assumptions are considered here in order to better understand the random variables involved in the flaw signature estimation problem and the range of applicability of the filter.

Electronic Noise

Time domain analysis

The impact of the measurement procedures and initial signal processing steps described above must be established. Each digitized signal represents one outcome associated with each of 512 different random variables. By averaging the signals from 64 intervals (Eq. (4.1)), the amplitude at each time is determined as the average outcome associated with 64 different random variables. By subtracting the average value (Eq. (4.2)), the mean associated with each stored signal is necessarily equal to zero.

In characterizing electronic noise which has been measured as described above, it is assumed that the random process is essentially ergodic (time-invariant). In strict terms, a random process is ergodic if one long time signal contains all possible statistical variations that would be encountered if an ensemble of signals were considered (Mix 1969, Brown 1983). Here, strict ergodicy is not required; however, time-invariance is required to the extent that signals determined over a number of segments from one long time signal can be used to examine the complex random variables which describe the random process in the frequency domain. The time-invariance of electronic noise can be demonstrated by considering the variations in the mean and variance associated with the 36 measured electronic noise signals (see Table 4.1) (Bendat and Persal 1971). The mean and variance of each signal is determined by calculating the mean and variance associated with the 512 amplitudes (Eq. (4.2)) which make up each signal. Figures 5.1.a and 5.1.b show plots of the signal mean and signal variance, respectively, for the 36 signals where the horizontal axis is displayed in chronological order from left to right. As expected, no trend in apparent in either plot as the data points seem to oscillates about a horizontal line in each case.

In analyzing noise, it is important that the signals to be analyzed are uncorrelated. It will be shown that the electronic noise signals are uncorrelated by utilizing a temporal correlation function. In terms of electronic noise signals, this function can be written for the k^{th} signal shifted to the left relative to the i^{th} signal as

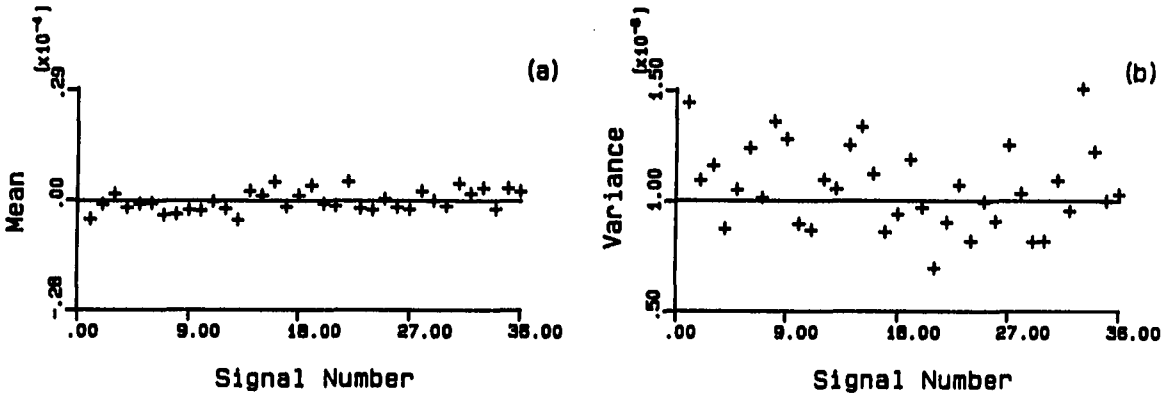

Figure 5.1. Electronic noise time-invariance. a) signal mean versus signal number; b) signal variance versus signal number

$$\rho_t(\tau,T_i,T_k) = \frac{\sum_{j=1}^{512-\tau} n_e(t_j,\zeta_1,T_i)\, n_e(t_{j+\tau},\zeta_1,T_k)}{\sqrt{\sum_{j=1}^{512-\tau} n_e^2(t_j,\zeta_1,T_i) \sum_{j=1}^{512-\tau} n_e^2(t_{j+\tau},\zeta_1,T_k)}} \qquad (5.1)$$

where the parameters T_i and T_k are included in $\rho_t(\tau,T_i,T_k)$ to indicate that it represents the correlation between the i^{th} signal and the k^{th} signal. The opposite shift direction is similarly defined. All results shown here are for 100 shifts in each direction. As defined here, $\rho_t(\tau,T_i,T_k)$ can be thought of as a normalized time-autocorrelation function. It is normalized in the sense that $\rho_t(\tau,T_i,T_k)$ ranges from 1.0 for perfectly correlated data to -1.0 for negatively correlated data (Whalen 1971, Beauchamp and Yuen 1979). It is a time-autocorrelation function (Whalen 1971, Brown 1983) in the sense that it involves temporal

summations (i.e., summations over t) as opposed to ensemble summations (i.e., summations over ζ). Further, note that $\rho_t(\tau,T_i,T_k)$ indicates that the resultant correlation is a function of which two signals are correlated; however, it does not indicated a dependence on the starting time, t_j, of the correlation. Thus, there is an implicit time-invariance based assumption behind Eq. (5.1) which says that the correlation is a function only of the time shift, τ, and not the absolute time, t_j (Whalen 1071, Brown 1983).

As given by Eq. (5.1), $\rho_t(\tau,T_i,T_k)$ will vary depending on which two signals are chosen and thus represents one sample of the correlation between signals. A sample average, $\bar{\rho}_t(\tau)$, can be determined by averaging $\rho_t(\tau,T_i,T_k)$ over a number of signal combinations (Bendat and Persal 1971). This average correlation can be determined for N noise signals as

$$\bar{\rho}_t(\tau) = \frac{1}{N-c} \sum_{i=1}^{N-c} \rho_t(\tau,T_i,T_{i+c}) \qquad (5.2)$$

where c=0 specifies the average correlation of a signal with itself (i.e., the average correlation of 1 with 1, 2 with 2, ...), and c=1 specifies the average correlation between successive signals (i.e., 1 with 2, 2 with 3, ...).

Shown in Fig. 5.2.a is $\rho_t(\tau,T_1,T_1)$ (Eq. (5.1) with i=k) which represents one sample of the correlation of an electronic noise signal with itself. Shown in Fig. 5.2.b is $\bar{\rho}_t(\tau)$ (Eq. (5.2) with c=0). In both cases, for τ=0, the correlation equals 1.0. Due to the high frequency content associated with electronic noise, the correlation quickly drops off as a signal is shifted relative to itself. The relationship between

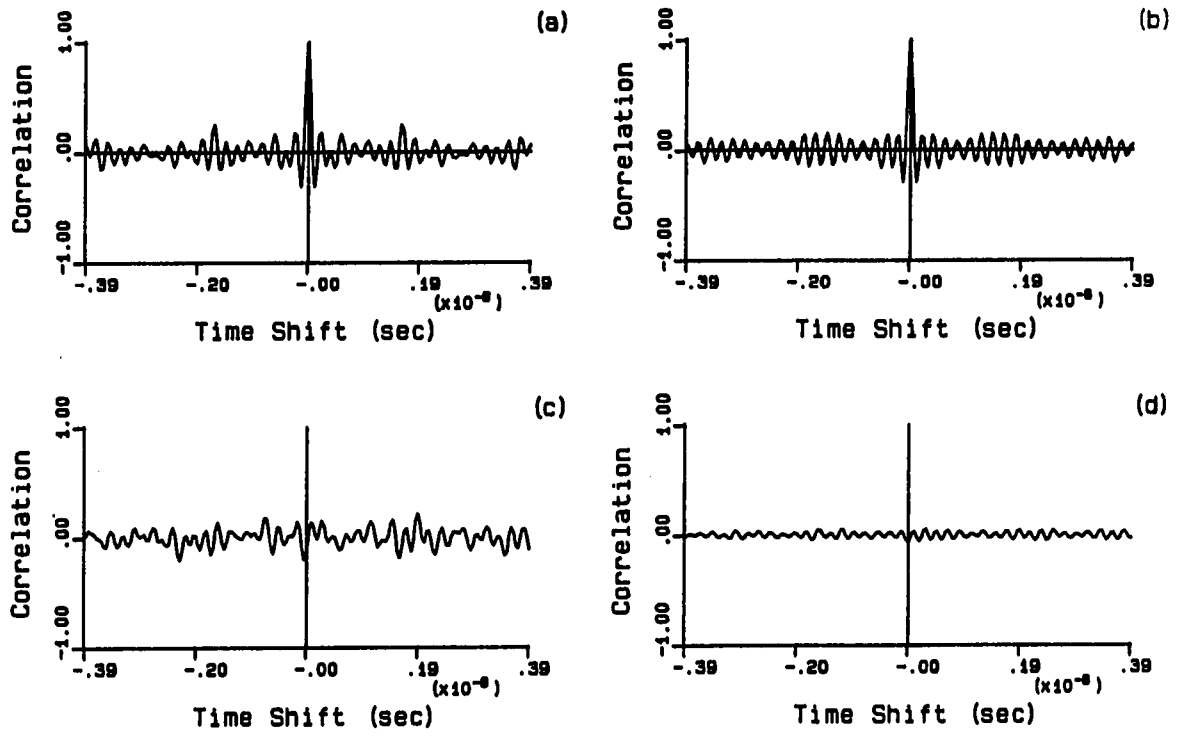

Figure 5.2. Electronic time domain correlation. a) single autocorrelation; b) average autocorrelation; c) single crosscorrelation; d) average crosscorrelation

autocorrelation functions and frequency content (Whalen 1971, Beauchamp and Yuen 1979) is evident in these figures. Specifically, the period of the oscillations in Fig. 5.2.b indicates a dominant frequency component at approximately 49MHz. This is in fact the case as presumably a 49MHz radio signal was picked up and digitized. This frequency component is clearly evident in the average power spectrum for the electronic noise shown in Fig. 4.4.a. Plots for the correlation between signals are also shown in Fig. 5.1. Figure 5.2.c is $\rho_t(\tau,T_1,T_1)$ (Eq. (5.1) with $i \neq k$) and Fig. 5.2.d

is $\bar{\rho}_t(\tau)$ (Eq. (5.2) with c=1). Both plots oscillate about zero, indicating that the electronic noise signals are uncorrelated as expected.

As a final time domain analysis of electronic noise, consider the distribution associated with electronic noise. If electronic noise is Gaussian and if variations in one time signal are representative of variations associated with the random process, a single noise signal should show a Gaussian distribution of amplitudes. One method of comparing a distribution of amplitudes with a Gaussian distribution is via a probability plot (Hahn and Shapiro 1967, Shapiro 1980). A probability plot is particularly useful since it provides a visual comparison tool which may indicate what type of deviations from a Gaussian exist. The basic idea of a probability plot (Hahn and Shapiro 1967) is to plot ordered observations, x_i's, versus the expected value of the ordered observation, $E[x_{i,n}]$, where the expected value is a function of the sample size, n, and the assumed distribution. If the sample size is very large and the assumed distribution is correct, the plot of x_i versus $E[x_{i,n}]$ (i.e., the probability plot) will be a straight line. As the sample size decreases, still for the correct distribution, the plot of x_i versus $E[x_{i,n}]$ will show some deviation from a straight line due to sampling fluctuations.

A probability plot for the amplitude distribution ($n_e(t_i, \zeta_1, T)$ i=170,340) associated with a segment one of the electronic noise signals is shown in Fig. 5.3. The data follow the straight line extremely well, especially in the central portions of the distribution. As expected, it is concluded that electronic noise is reasonably Gaussian in the time

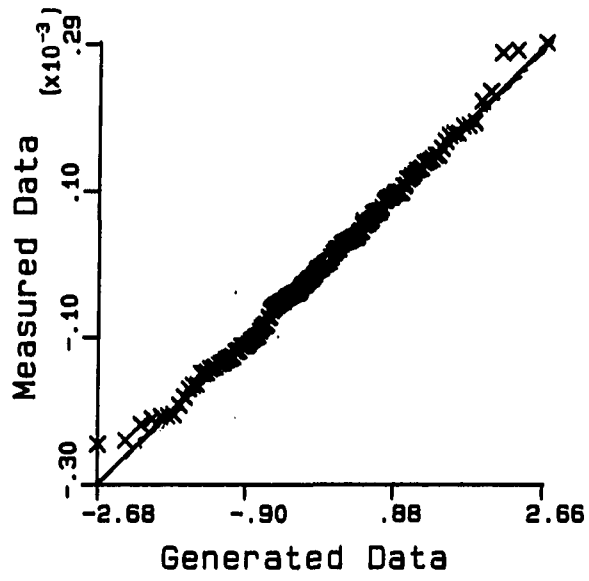

Figure 5.3. Electronic noise probability plot (time domain).

domain. Note that the central limit theorem (Papoulis 1965, Larson 1974) says that the distribution associated with the sum of independent random variables will tend to be Gaussian. In the case of electronic noise, it is likely that the voltage at any given time could be represented as the sum of a number of (unknown) independently occurring random events in the electronics of the ultrasonic system. Thus, it is not surprising that electronic noise tends to be Gaussian.

Frequency domain analysis

Frequency domain signals were determined by first truncating each signal at the first zero-crossing (see Chapter V) outside of the middle third of the signal (i.e., outside of the range from t_{170} to t_{340}), followed by a Fourier transform. The frequency domain analysis is begun by considering the ensemble mean and ensemble variance at each frequency. Estimates of the ensemble mean and ensemble variance can be determined by calculating the sample mean and sample variance for the available data (Chernoff and Moses 1959, Mendel 1983). Written in electronic noise terms, the real part of the sample mean (equivalently, the sample mean for the real part) at the i^{th} frequency can be defined as

$$\mathrm{Re}[\bar{m}_{n_e}(\omega_i)] = \frac{1}{36}\sum_{k=1}^{36}\mathrm{Re}[n_e(\omega_i,\zeta_1,T_k)] \qquad (5.3)$$

where $n_e(\omega,\zeta_1,T_k)$ is the Fourier transform of the truncated version of the k^{th} time domain electronic noise signal, $n_e(t,\zeta_1,T_k)$. The sample mean for the imaginary part can be similarly defined. The sample mean for the real and imaginary parts for electronic noise are not shown here since they are so small relative to a single sample of electronic noise that they appear to be zero lines. Sample means for case 3 acoustic noise are shown in Fig. 5.10 and will serve as representative examples of the oscillations about zero typical of the sample means for the electronic noise.

Given that electronic noise has zero mean at each frequency, the sample variance at the i^{th} frequency can be written in electronic noise terms as

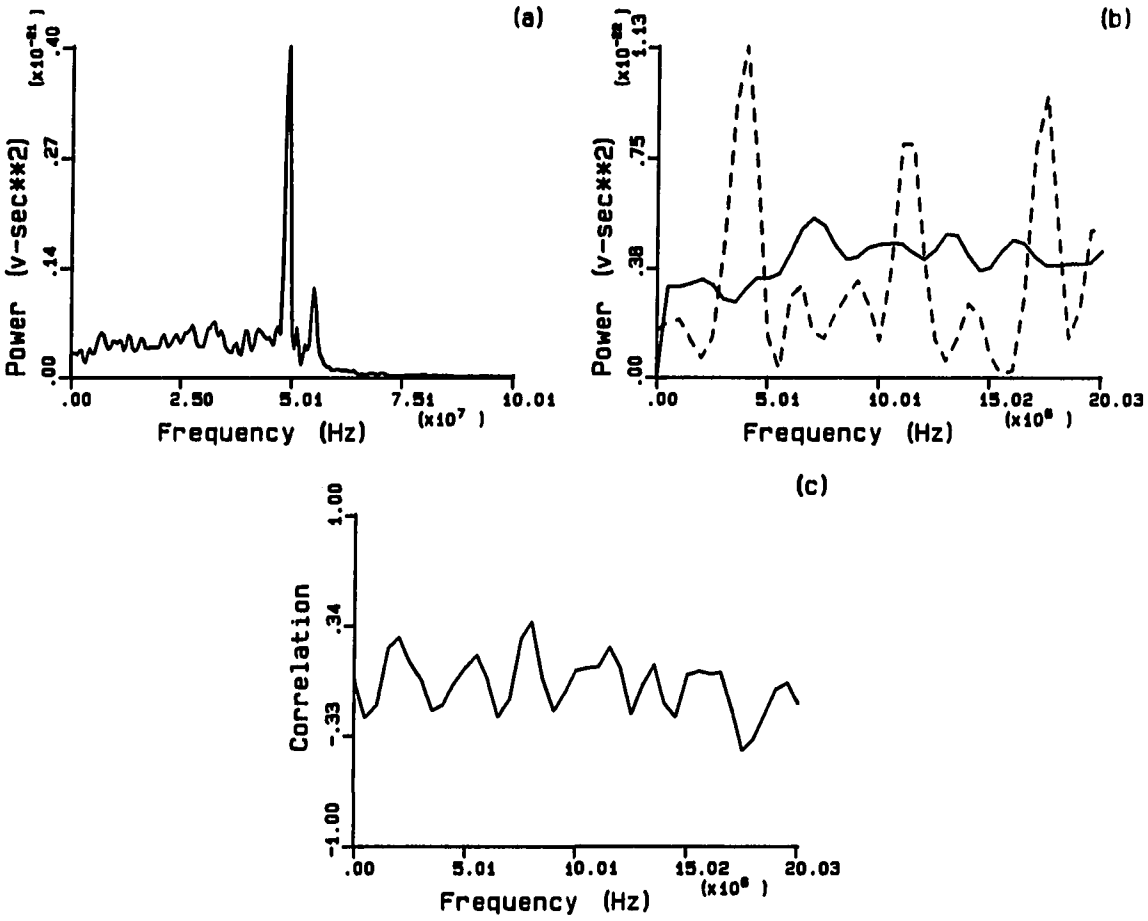

Figure 5.4. Electronic noise frequency domain analysis. a) average power; b) smoothed average power (solid) and single signal power (dashed); c) sample correlation coefficient

$$\bar{\sigma}^2_{n_e}(\omega_i) = \frac{1}{36} \sum_{k=1}^{36} \mathrm{Re}[n_e(\omega_i, \zeta_1, T_k)]^2 + \mathrm{Im}[n_e(\omega_i, \zeta_1, T_k)]^2 \qquad (5.4)$$

With the mean equal to zero, this becomes the mean square value or average power at each frequency. Since electronic is typically white noise, it is expected that the sample variance (average power) will oscillate about some constant value, independent of frequency (Mix 1969). Figure 5.4.a

shows the average power at each frequency from 0 to 100MHz. As expected, the average power tends to oscillate about a nearly horizontal line. The figure also shows the dominant radio frequency at approximately 49MHz. The dashed line in Fig 5.4.b shows the power at each frequency (0-20MHz) associated with a single noise signal. The solid line in Fig 5.4.b shows the average power (Fig. 5.4.a) smoothed via a 3 point running average. While sample size effects are still evident, the average power approaches a constant value, independent of frequency.

Electronic noise is assumed to be uncorrelated. As previously discussed, for a complex random variable to be uncorrelated, both the real and imaginary parts must be uncorrelated (Goodman 1963, Whalen 1972). In order to evaluate this assumption, the ensemble correlation coefficient as defined in Eq. (3.4) was estimated at each frequency with a sample correlation coefficient. In electronic noise terms with the mean at each frequency equal to zero, the sample correlation coefficient at the i^{th} frequency can be written as

$$\bar{\rho}(\omega_i) = \frac{\sum_{k=1}^{36} \mathrm{Re}[n_e(\omega_i,\zeta_1,T_k)]\ \mathrm{Im}[n_e(\omega_i,\zeta_1,T_k)]}{\sqrt{\sum_{k=1}^{36} \mathrm{Re}[n_e^2(\omega_i,\zeta_1,T_k)] \sum_{k=1}^{36} \mathrm{Im}[n_e^2(\omega_i,\zeta_1,T_k)]}} \qquad (5.5)$$

Figure 5.4.c shows the sample correlation coefficient at each frequency for the 36 electronic noise signals. Again, while the effects of the small sample size are evident, the correlation coefficient oscillates about zero, indicating that the real and imaginary parts of electronic noise are uncorrelated.

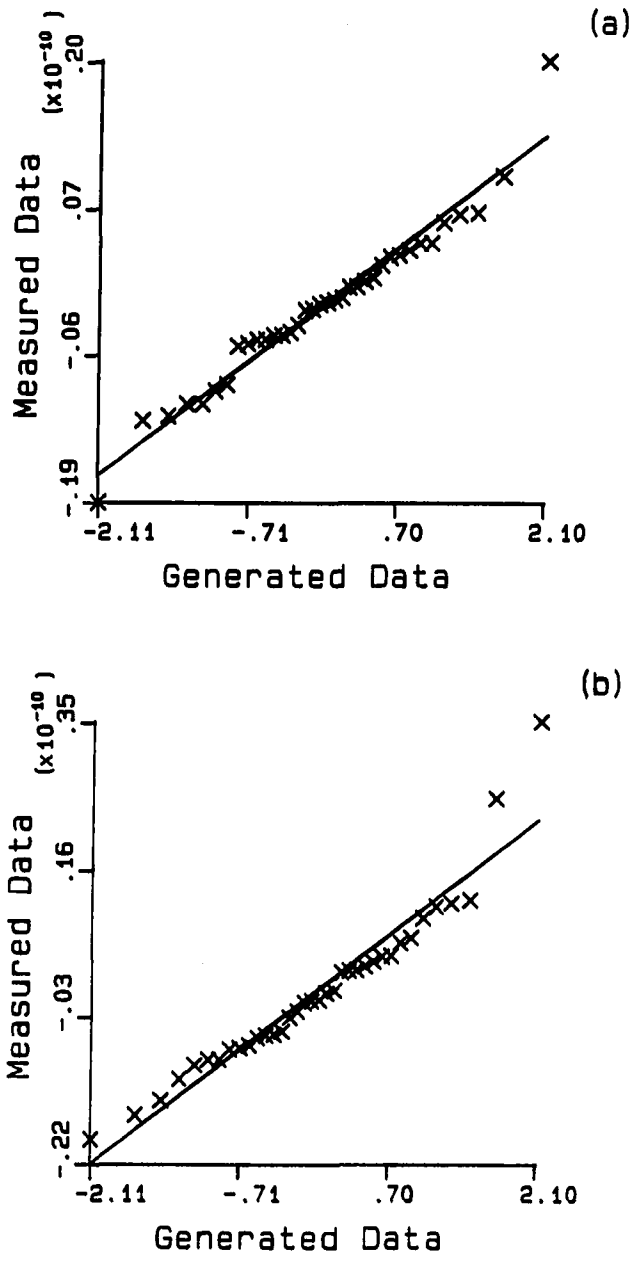

Figure 5.5. Electronic noise probability plots (frequency domain). a) and b) real and imaginary parts, respectively, at 10MHz

For a complex random variable to be Gaussian, its real part an imaginary parts must be Gaussian (Goodman 1963, Whalen 1972). Therefore, the amplitude distribution for the real part ($Re[n_e(\omega_1,\zeta_1,T_k)]$ k=1,36) and the imaginary part ($Im[n_e(\omega_1,\zeta_1,T_k)]$ k=1,36) is considered at a particular frequency. Probability plots are shown in Figures 5.5.a and 5.5.b for the real and imaginary parts, respectively, at 10MHz. In both cases, the distributions appear to be reasonably Gaussian especially in the middle range. There is no evidence that the electronic noise distribution should depend on frequency, therefore, only the distribution at 10MHz is considered here.

Summarizing, random variable analysis procedures have been established and used to analyze electronic noise in the time domain and in the frequency domain. It has been shown that electronic noise is uncorrelated and reasonably Gaussian, and that it has zero mean and an average power spectrum which is characteristic of white noise.

Acoustic Noise

Time domain analysis

A similar approach as that used in the analysis of electronic noise will be used to analyze acoustic noise. Measurement conditions associated with each of the three types of acoustic noise considered are summarized in Table 4.1. The noise analyzed in this section will be referred to as acoustic noise where it is noted, as given by Eq. (4.6), that the noise signals include small amounts of electronic noise and some errors due to imperfect subtraction of the ringing noise.

First, it is necessary to establish what each signal represents. Unlike electronic noise, the signals measured at the grid positions represent a family of acoustic noise signals. The signal corresponding to the i^{th} grid position, $n(t,\zeta_i)$, represents the i^{th} outcome or sample of the acoustic noise random process. At a particular time, $n(t_i,\zeta)$ is a random variable whose amplitude varies over the grid positions. Similarly, at a particular frequency, $n(\omega_i,\zeta)$ is a complex random variable whose real and imaginary parts vary over the grid positions. Further, the process of determining the average of 64 pulses (Eq. (4.2)) has no effect on the acoustic noise contribution to the measured noise signal. Since the measurement setup is not changed between pulses, at a given grid position the scattering which occurs is the same with each pulse. Only electronic noise which varies with time is effected by the averaging. Subtracting the mean (Eq. (4.2)) creates noise signals with zero mean, and, as with electronic noise, dictates that acoustic noise has zero mean in both the time and frequency domain.

In general, acoustic noise decays with time, primarily due to attenuation and diffraction, and is therefore not time-invariant (Mason and NcSkimin 1947, Papadakis 1968, Goebbels 1980, Stanke 1983, Stanke and Kino 1984). This can be shown by considering the mean and variance as a function of time for the 36 signals (Bendat and Persal 1971). Each signal was divided into 9 segments containing 50 points each with the first segment beginning at t_{30}. The mean for the j^{th} segment can be written as

$$\bar{m}_j = \frac{1}{N} \sum_{k=1}^{N} \left[\frac{1}{50} \sum_{i=1}^{50} n(t_i,\zeta_k) \right] \tag{5.6}$$

where N is the total number of grid positions. Assuming that the mean of each segment is zero, the variance for the j^{th} segment can be written as

$$\bar{\sigma}_j^2 = \frac{1}{N} \sum_{k=1}^{N} \left[\frac{1}{50} \sum_{i=1}^{50} n^2(t_i, \zeta_k) \right] \tag{5.7}$$

Figure 5.6 shows the average mean for each segment as a function of the central time of each segment for case 1 acoustic noise (Fig. 5.6.a), case 2 acoustic noise (Fig. 5.6.c), and case 3 acoustic noise (Fig. 5.6.e). The plots oscillate about zero and show no trend, indicating that the mean is time-invariant. The average variance for each segment as a function of the central time of each segment is shown for case 1 acoustic noise in Fig. 5.6.b, for case 2 acoustic noise in Fig. 5.6.d, and for case 3 acoustic noise in Fig. 5.6.f. The straight lines are shown only for reference purposes. Case 1 acoustic noise and case 3 acoustic noise which involve interrogation with a planar transducer show the decaying nature as expected, indicating that in general acoustic noise is not time-invariant. Case 2 acoustic noise which involves interrogation with a focussed transducer does not show an obvious decaying trend; however, this is not surprising since the noise was measured near the focal point of the interrogating field. In all cases, the variance is relatively stable over a few segments. The practical implication of this is that over the relatively short time period occupied by a flaw signal, acoustic noise can be treated as time-invariant (Beauchamp and Yuen 1979).

A temporal correlation function (Eq. (5.1)) was used to show that the electronic noise signals are uncorrelated. Assuring that the acoustic noise signals measured at adjacent grid positions are uncorrelated must be

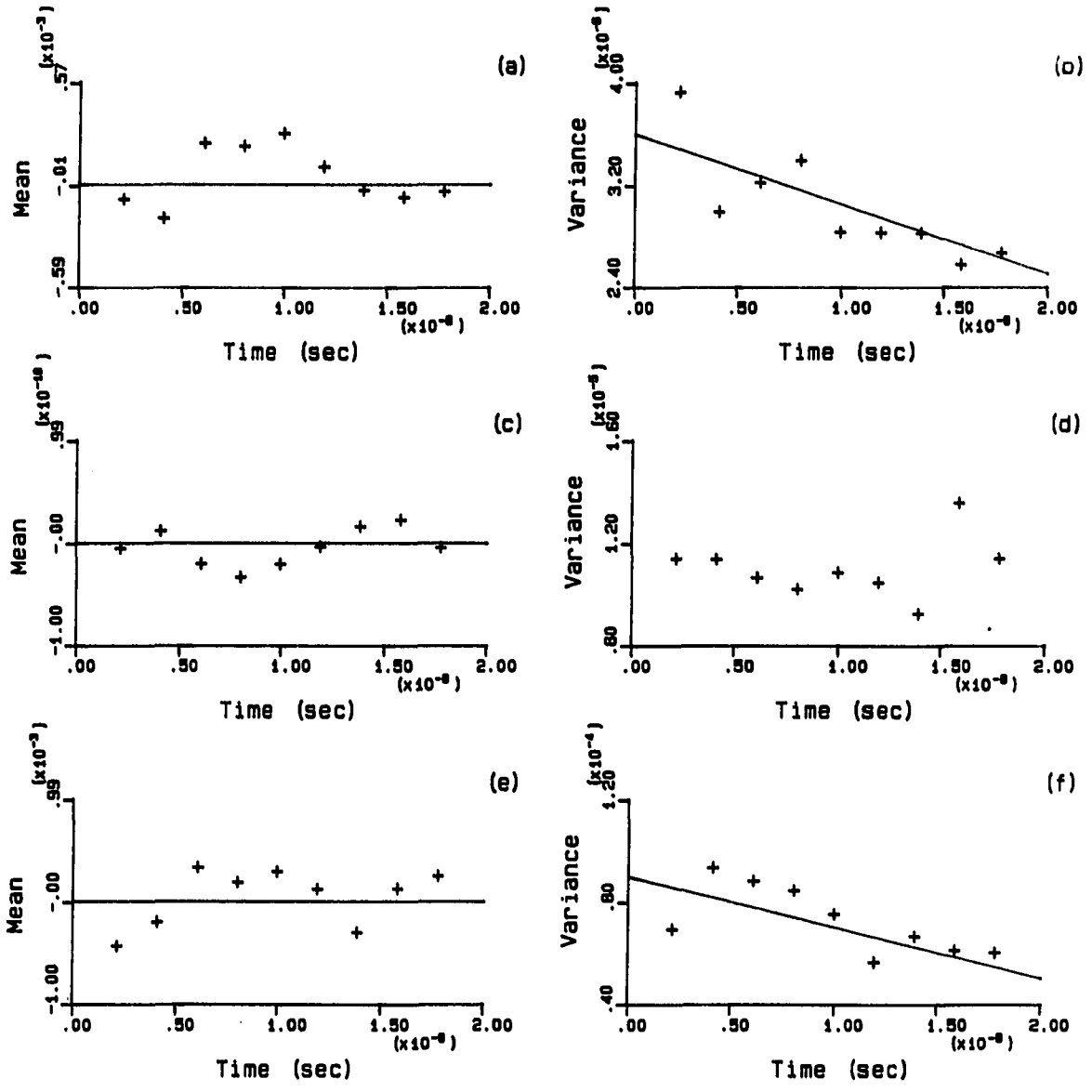

Figure 5.6. Acoustic noise time-invariance. a) and b) case 1; c) and d) case 2; e) and f) case 3

considered (Fertig et al. 1985). In terms of acoustic noise, the correlation function will be denoted $\rho_t(\tau, \zeta_i, \zeta_k)$ and can be written for the k^{th} signal shifted to the left relative to the i^{th} signal as

$$\rho_t(\tau, \zeta_i, \zeta_k) = \frac{\sum_{j=1}^{512-\tau} n(t_j, \zeta_i)\, n(t_{j+\tau}, \zeta_k)}{\sqrt{\sum_{j=1}^{512-\tau} n^2(t_j, \zeta_i) \sum_{j=1}^{512-\tau} n^2(t_{j+\tau}, \zeta_k)}} \tag{5.8}$$

The opposite shift direction is similarly defined. An average correlation function can be defined in analogy with Eq. (5.2) as

$$\bar{\rho}_t(\tau) = \frac{1}{N-c} \sum_{i=1}^{N-c} \rho_t(\tau, \zeta_i, \zeta_{i+c}) \tag{5.9}$$

where the averaging now takes place over combinations of grid positions. Here, the correlation is between samples of the acoustic noise random process. Therefore, the correlation function can be thought of as normalized time-autocorrelation function when c=0, and a normalized time-crosscorrelation function when c=1. In the crosscorrelation case, the correlation between samples of one random process is considered as opposed to the correlation between different random processes.

Full results for case 3 acoustic noise are given in Figure 5.7.a-d. Figure 5.7.a shows the time-autocorrelation function for a single signal (Eq. (5.8) with i=j) for 100 shifts in each direction. The plot has definite structure, showing two distinct periodicities. The strongest period shows a cycle from 0 to a shift of approximately 0.18μs. This indicates a strong frequency component at approximately 5.5MHz. The second periodicity shows smaller peaks at approximately half the period

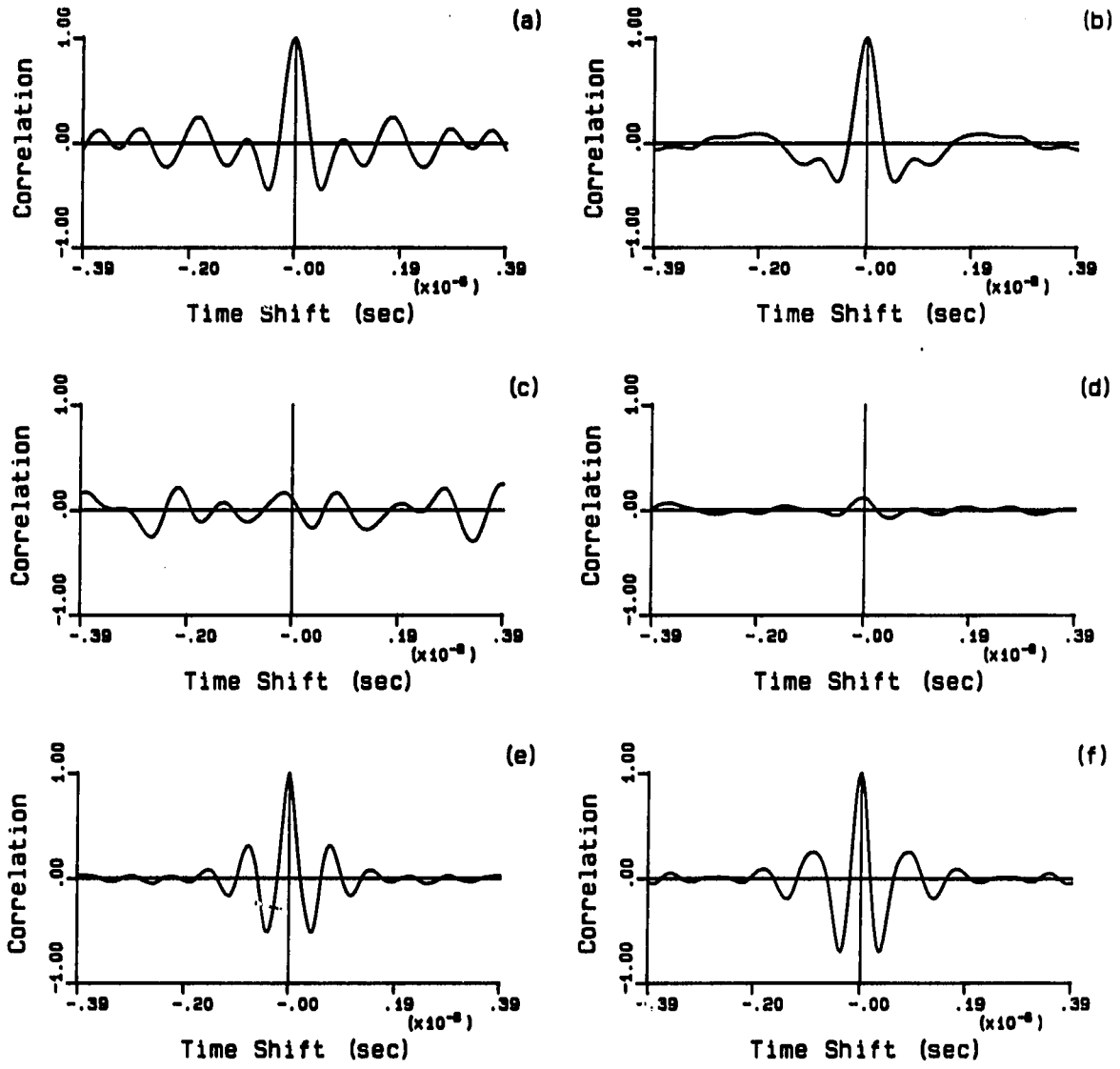

Figure 5.7. Acoustic noise time domain correlation. a) and b) case 3 time-autocorrelation; c) and d) case 3 time-crosscorrelation; e) and f) time-autocorrelation for case 1 and case 2, respectively

indicating a frequency component with somewhat less strength at approximately 11MHz. Figure 5.7.b shows the average time-autocorrelation for the 27 case 3 acoustic noise signals ($\bar{\rho}_t(\tau)$ with c=0). Contributions due to the two dominant frequency components are still evident. The existence of these frequency components will be shown in discussing acoustic noise average power spectrum later in this section. Shown in Fig. 5.7.c and Fig. 5.7.d are the time-crosscorrelation between two case 3 acoustic noise signals (Eq. (5.8) with $i \neq j$) and the average time-crosscorrelation for case 3 acoustic noise ($\bar{\rho}_t(\tau)$ with c=1), respectively. These plots indicate that the case 3 acoustic noise signals measured at adjacent grid positions are uncorrelated. Similar results (not shown) were obtained for case 1 acoustic noise and case 2 acoustic noise, indicating that signals at adjacent grid positions are uncorrelated for all three types of acoustic noise. Figures 5.7.e and 5.7.f show the average time-autocorrelation for case 1 acoustic noise and case 2 acoustic noise, respectively. Figure 5.7.e indicates a strong frequency component at approximately 13MHz for case 1 acoustic noise, and Fig. 5.7.f indicates strength at approximately 12MHz for case 2 acoustic noise.

It is important that the ringing noise be subtracted (as described above) prior to the correlation step for both types of correlation. If this is not done, the correlation may be dominated by the correlation between ringing contributions. Also, recall that the correlation functions used here have an implicit time-invariance assumption. Therefore, the acoustic noise correlation functions shown in Fig. 5.7 are dependent on the time interval over which the signals were measured and

contain some contributions due to the decay of the signals (case 1 acoustic noise and case 3 acoustic noise) with time.

Since a family of acoustic noise signals is available, the distribution associated with random variables can be considered. That is, the distribution associated with the amplitude variations at a particular time, over the N grid positions ($n_a(t_i, \zeta_k)$ k=1,N) can be compared to a Gaussian distribution. Probability plots for the random variable $n(t_{200}, \zeta)$ are shown in Figures 5.8.a-c for case 1 acoustic noise, case 2 acoustic noise, and case 3 acoustic noise, respectively. While a limited number of points are available, the data fit the line well within the central regions for each case, indicating that each type of noise is reasonably Gaussian.

A probability plot of a single acoustic noise signal ($n_a(t_i, \zeta_k)$ i=170,340; i.e., the middle third) for case 3 acoustic noise is shown in Fig. 5.9. This represents the worst result of the three cases. This plot also shows that the distribution is center-weighted and reasonably Gaussian.

It would appear that acoustic noise is reasonably Gaussian in the time domain when considering the distribution of amplitudes for a particular random variable (Fig. 5.8) and when considering the distribution of amplitudes for a particular signal (Fig. 5.9). The central limit theorem can again be employed to explain this near Gaussian behavior. The amplitude of an acoustic noise signal is due to the summation of the contributions due to the scattering at a large number of sites. Since the contribution due to the scattering at each site is a random variable, the central limit theorem says the amplitude distribution

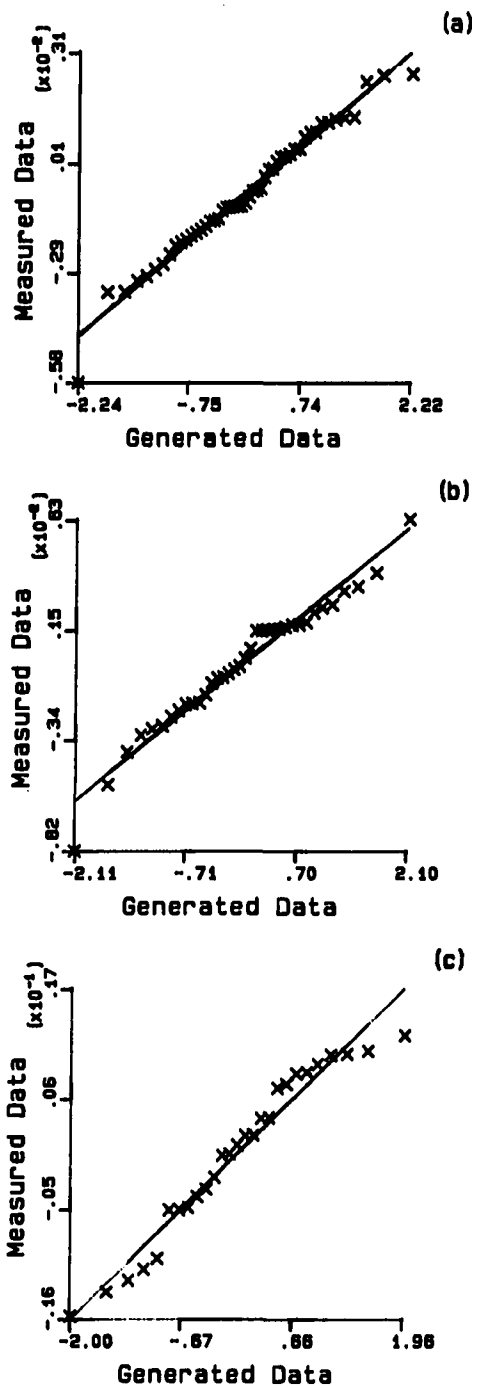

Figure 5.8. Acoustic noise probability plots at t_{200}). a) case 1; b) case 2; c) case 3

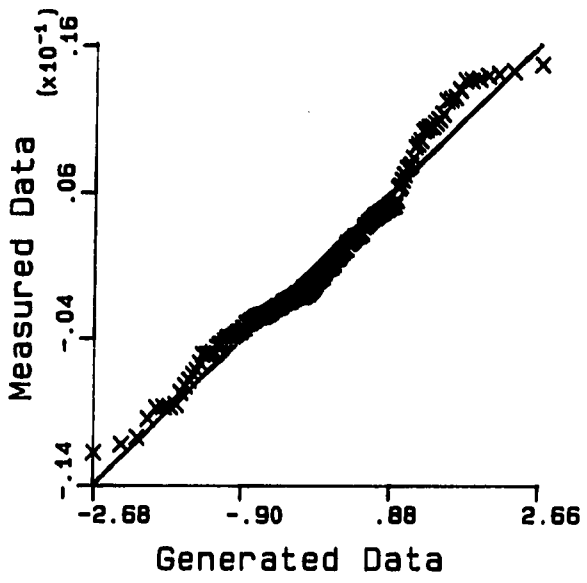

Figure 5.9. Acoustic noise (case 3) temporal probability plot.

due to the summation of all of the individual scattering contributions will tend toward a Gaussian distribution. Therefore, it is not surprising that acoustic noise is reasonably Gaussian. It is also reasonable to expect that when a large number of scattering sites are involved, acoustic noise will be reasonably Gaussian, independent of the nature of the scatterers. Here, grain scattering and pore scattering was considered. As with electronic noise, it is anticipated that acoustic noise will be Gaussian in the frequency domain.

Frequency domain analysis

Frequency domain signals were determined by first truncating each signal outside of the middle third of each signal using the zero-crossing truncation method, followed by a Fourier transform. The sample mean and

sample correlation coefficient were determined at each frequency. Sample means were calculated using Eq. (5.3) written in acoustic noise terms. The sample correlation coefficient defined in analogy with Eq. (5.5). Representative results are shown in Fig. 5.10 for case 3 acoustic noise. Shown in Fig. 5.10.a is the real part of a single case 3 acoustic noise signal. It demonstrates that noise shows wild oscillations in the frequency domain similar to those seen in time domain noise signals. Figures 5.10.b and 5.10.c show the sample mean for the real part and for the imaginary part, respectively, plotted on the same scale as Fig. 5.10.a. As expected, case 3 acoustic noise has zero mean in the frequency domain. Similar results were attained for the other two cases. Figure 5.10.d shows the sample correlation coefficient at each frequency for case 3 acoustic noise. The plot shows no distinct trend as it tends to oscillate about zero. Similar results were attained for the other two cases. Note that the effects of the small sample size are evident in oscillations of Fig. 5.10.d. The value at each frequency in Fig. 5.10.d involves the summation of the product of only 27 real and imaginary pairs while each value in the time domain correlation results (Figures 5.2 and 5.7) involves the summation of the product of at least 400 pairs of amplitudes. As a check that the peaks and valleys in plots of sample correlation coefficient versus frequency are sample effects, the sample correlation coefficient versus frequency was calculated for two sets of 23 signals for case 1 acoustic noise (49 case 1 acoustic noise signals were measured). For both sets of signals, the results showed oscillations about zero typical of those seen in Fig. 5.10.d; however, the positions of the peaks and valleys were not the same for the two sets of signals.

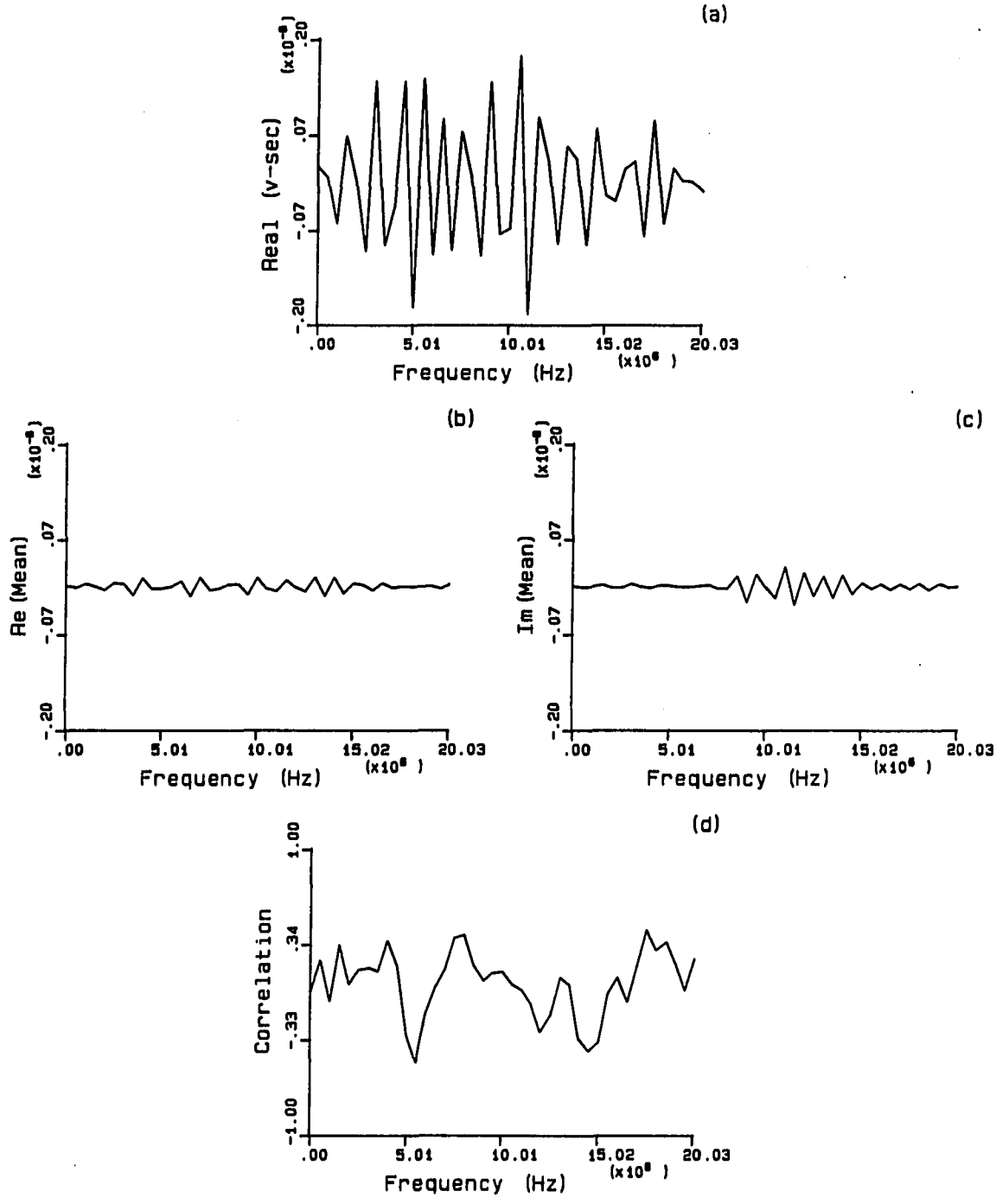

Figure 5.10. Acoustic noise (case 3) frequency domain analysis. a) typical real part for a single noise signal; b) and c) sample mean for the real part and imaginary part, respectively; d) sample correlation coefficient

For completeness, it is stated without presenting any correlation results that noise and scattering amplitude are uncorrelated. Given the random (noise-like) nature of acoustic noise in the frequency domain (Fig. 5.10.a) and the structured nature of scattering amplitudes (Figures 2.2 and 2.3), there is no reason to expect the real and imaginary parts of noise and scattering amplitude to be correlated.

The sample variance at each frequency for each case was determined using Eq. (5.4) written in acoustic noise terms. For zero mean, the sample variance at each frequency is the average power at that frequency. For each case, the average power at each frequency was shown in Fig 4.4 (Neal and Thompson 1986). Peaks at approximately the frequencies indicated by the time-autocorrelation functions (Fig. 5.7) are evident in each case.

The distribution of the real and imaginary parts was considered at 6MHz for case 3 acoustic noise and at 12MHz for case 1 acoustic noise and case 2 acoustic noise. Figures 5.11.a, 5.11.c, and 5.11.e show probability plots for the real part for cases 1 acoustic noise, case 2 acoustic noise, and case 3 acoustic noise, respectively. Similar plots for the imaginary parts are shown in Figures 5.11.b, 5.11.d, and 5.11.f. In all cases, the data follow the straight line well, indicating that each type of acoustic noise is reasonably Gaussian in the frequency domain.

Summarizing, for the three material/transducer combinations, acoustic noise has been shown to be uncorrelated and reasonably Gaussian with zero mean. The variance (average power) as required by the optimal Wiener filter has been established for each case.

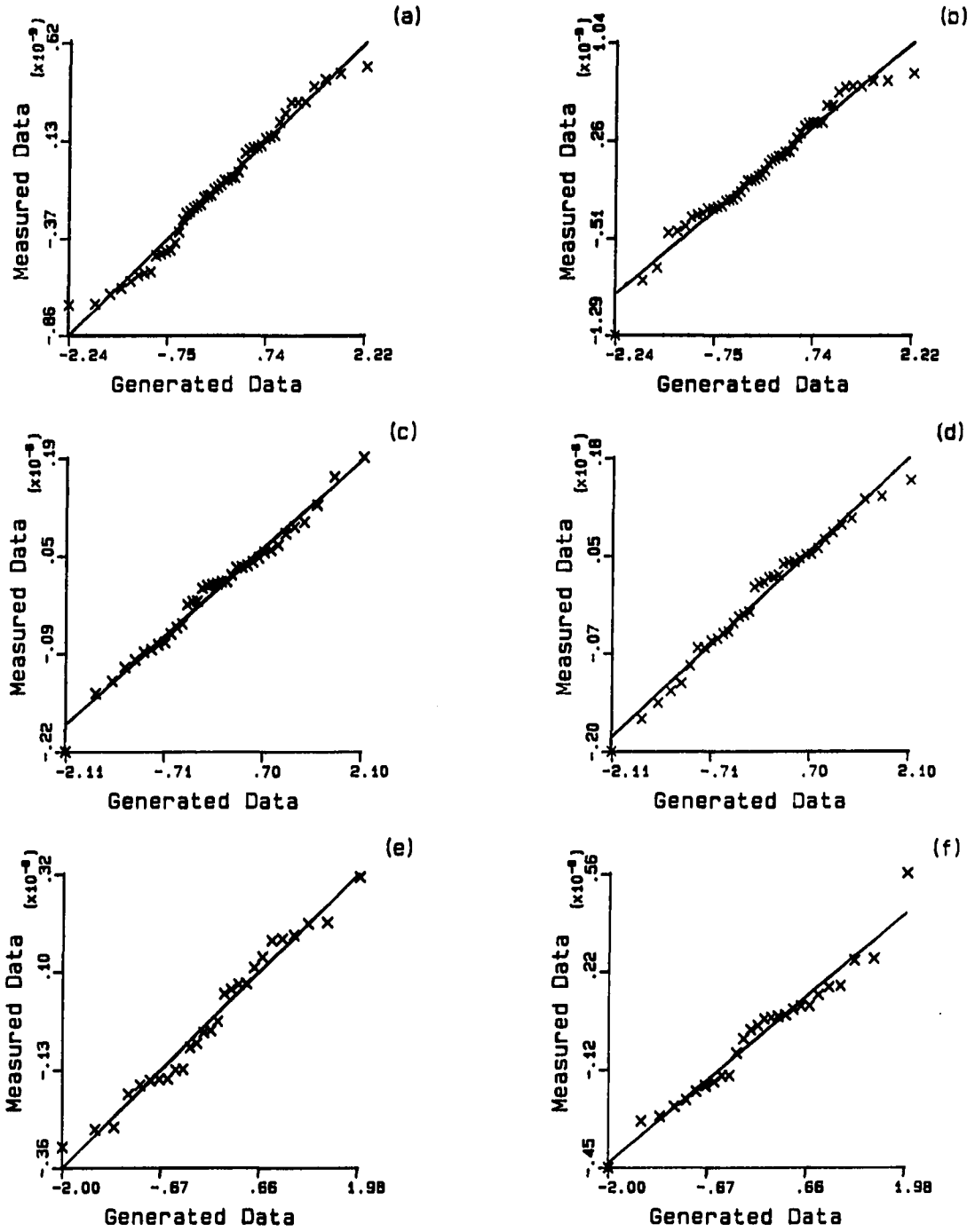

Figure 5.11. Acoustic noise probability plots (frequency domain). a) and b) real and imaginary parts, respectively, 12MHz, case 1; c) and d) real and imaginary parts, respectively, 12MHz, case 2; e) and f) real and imaginary parts, respectively, 6MHz, case 3

Scattering Amplitude

Preliminary comments

There is a basic difference between scattering amplitude as a random variable and noise as a random variable. Random variables can be classified as either deterministic or non-deterministic (Brown 1983). Noise, which has no structure and simply wanders on in a "noise-like manner", can be classified as a non-deterministic random variable. Scattering amplitude, which does not have a random noise-like character, can be considered to be a deterministic random variable. For example, Eq. (2.7) shows that an ensemble of scattering amplitudes associated with an ensemble of Born scatterers would have a deterministic form where the randomness would be associated only with the random variable, a, which represents the radii of the flaws in the ensemble. A primary consequence of this deterministic nature is the ability to anticipate results associated with the analysis of scattering amplitude. To this end, scattering amplitude characteristics established in Chapter II are reviewed below followed by a summary of the implications of these characteristics.

Pertinent scattering amplitude characteristics for volumetric scatterers can be summarized as follows: 1) $A(\omega)$ is dependent on ka; 2) the initial sign of $Re[A(\omega)]$ and $Im[A(\omega)]$ is controlled by the reflection coefficient between the flaw and the host; 3) the real and imaginary parts for volumetric scatterers start out from zero frequency with opposite sign; 4) for a given flaw/host combination, $A(\omega)$ for all flaw sizes start out from zero frequency "in phase"; and 5) at intermediate and high

frequencies, scattering amplitudes for different flaw sizes are "out of phase".

In terms of scattering amplitude analysis, the consequences of these characteristics can be summarized as follows: 1) the scattering amplitude distribution will not be the same in different ka ranges; 2) at long wavelength (low frequency) for a distribution of flaws with a given flaw/host combination, the scattering amplitude distribution will not be Gaussian since Re[A(ω)] and Im[A(ω)] will either be positive for all flaws or negative for all flaws; 3) as a consequence of the previous point, $m_A(\omega)$ will not be equal to zero at long wavelength; 4) also at long wavelength, since scattering amplitudes are "in phase", $\sigma_A^2(\omega)$ will be relatively low; 5) at high frequencies, since scattering amplitudes oscillate about zero, at a given frequency, for different flaw sizes, $m_A(\omega)$ is expected to tend toward zero; 6) since scattering amplitudes are "out of phase" at high frequencies, $\sigma_A^2(\omega)$ is expected to be relatively large; 7) at low frequencies, the real and imaginary parts of the scattering amplitude are expected to be negatively correlated since they start out with opposite signs; and 8) at high frequency, the oscillatory nature of scattering amplitudes is expected to cause the real and imaginary parts to be uncorrelated.

Analysis

Unlike noise which can be directly measured and characterized, it is not possible to measure a family of scattering amplitudes. Prior information which may be available pertains to the physical characteristics of flaws (i.e., size, orientation, composition, etc.). A

reasonable procedure might be to 1) establish the flaw distribution characteristics (in practice, based on a combination of prior destructive evaluations and knowledge of the manufacturing processes); 2) generate a family of scattering amplitudes, $A(\omega, \zeta_k)$, corresponding to randomly chosen flaws (represented by ζ_k) out of the distribution; and 3) use the family of scattering amplitudes to analyze the random variables represented by $A(\omega_i, \zeta)$. An important restriction is that a forward solution, either analytical or numerical, must exist in order to generate scattering amplitudes corresponding to flaws in the distribution. As discussed in Chapter II, this is a restriction which is generally associated with the use of model based estimation techniques.

Distribution In general, given the probability density function $f(a)$ (a=radius) which describes the flaw size distribution, the scattering amplitude distribution cannot be determined analytically, even if an analytical forward solution exists. A generic probability density function transformation problem can be described as follows. Assume that an input-output situation is governed by y=g(x) where the random variable x is the input and the random variable y is the output. Further, assume that the "reverse" relationship x=h(y) can be determined such that x is a unique function of y. The problem of determining the probability density function $f_y(y)$ given $f_x(x)$ can be stated as (Brown 1983)

$$f_y(y) = \left| \frac{dx}{dy} \right| f_x(h(y)) \tag{5.10}$$

where subscripts have been added to the probability density functions in order to avoid confusion. In terms of the problem at hand, a single flaw size distribution determines, at each frequency, a distribution associated

with the real part and a distribution associated with the imaginary part of the scattering amplitude distribution. Therefore, the problem is to determine $f_{Re[A]}(Re[A(\omega_i,\zeta)])$ and $f_{Im[A]}(Im[A(\omega_i,\zeta)])$ given the probability density function $f_a(a)$. Equation (5.10) can be written for the real part as

$$f_{Re[A]}(Re[A(\omega_i,\zeta)]) = \left| \frac{da}{dA} \right| f_a(h(A)) \tag{5.11}$$

In order to determine the scattering amplitude probability density function, an analytical forward solution, $Re[A(\omega_i,\zeta)]=g(a)$, must exist, and it must be possible to "reverse" this relationship to find $a=h(Re[A(\omega_i,\zeta)])$. Analogous relationships can be stated for the imaginary part.

In order to analyze scattering amplitude distributions in a research environment, a flaw distribution must be assumed. In certain cases, the size distribution associated with voids or inclusions is approximately lognormal (Hatch and Choate 1929, Hatch 1933, Kottler 1950, Hahn and Shapiro 1967, Gubernatis and Domany 1983, Thompson et al. 1983a, Hsu and Uhl 1987). The random variable analyses and subsequent filter analyses presented in this dissertation are based on lognormal distributions. By definition, if the distribution associated with Log(a) is normal (Gaussian) with mean, m, and variance, σ^2, then the random variable a is lognormal with probability density function

$$f_a(a) = \frac{1}{\sqrt{2\pi}\,(\sigma)\,a} \exp\left[\frac{-(\text{Log } a - m)^2}{2\sigma^2} \right] \tag{5.12}$$

For a lognormal distribution of volumetric scatterer, the transformation represented by Eq. (5.11) is possible at long wavelength. For a particular frequency at long wavelength, $Re[A(\omega_i,\zeta)]$ is proportional to a^3 (Eq. (2.8)). In addition, $Im[A(\omega_i,\zeta)]$ is proportional to a^6 at long wavelength (Rose 1988). Thus, at particular frequency at long wavelength, the relationship between flaw radius and either part of $A(\omega_i,\zeta)$ can be described by the input-output relationship

$$A = b\, a^n \tag{5.13}$$

where b is a proportionality constant, a represents flaw radius, n=3 when the shorthand notation, A, represents $Re[A(\omega_i,\zeta)]$, and n=6 when A represents $Im[A(\omega_i,\zeta)]$. The reverse of this relationship is given by $a=(A/b)^{1/n}$. Thus, an analytical forward solution exists, the solution can be reversed, and the reverse relationship defines a one-to-one correspondence between flaw size and scattering amplitude. Under these circumstances, Eq. (5.11) can written as

$$f_A(A) = \left| \frac{d}{dA} (A/b)^{1/n} \right| f_a((A/b)^{1/n}) \tag{5.14}$$

Combining Equations (5.12) and (5.14), carrying out the differentiation, and rearranging yields

$$f_A(A) = \frac{1}{\sqrt{2\pi}\,(n\sigma)\,A} \exp\left[\frac{-[\text{Log } A - (\text{Log } b + nm)]^2}{2n^2\sigma^2} \right] \tag{5.15}$$

where m and σ^2 are the mean and variance, respectively, of the Gaussian random variable representing Log(a). Equation (5.15) shows that A is lognormal where the mean and variance of the Gaussian random variable

representing Log(A) are equal to Log(b)+nm and $2n^2\sigma^2$, respectively. To show that these equalities are true, reconsider Eq. (5.13). Taking the logarithm of both sides of Eq. (5.13) yields

$$\text{Log } A = \text{Log } b + n\text{Log } a \tag{5.16}$$

Since Log(A) and Log(a) are Gaussian

$$m_{\text{Log } A} = \text{Log } b + n m_{\text{Log } a} = \text{Log } b + nm \tag{5.17}$$

and

$$\sigma^2_{\text{Log } A} = n^2 \sigma^2_{\text{Log } a} = n^2\sigma^2 \tag{5.18}$$

Thus, for volumetric flaws at long wavelength, a lognormal distribution of flaws results in a lognormal distribution for $\text{Re}[A(\omega_i, \zeta)]$ and for $\text{Im}[A(\omega_i, \zeta)]$.

The scattering amplitude distribution will now be considered numerically. Provided that a forward solution exists, the distribution can be considered numerically from a family of calculated scattering amplitudes. The procedure which was used to establish a family of scattering amplitudes is as follows:

1. Establish the mean, m_a, and breadth (as represented by the standard deviation, σ_a) of the assumed lognormal flaw distribution;
2. Randomly generate N flaw sizes (ζ_k k=1,N) out of the assumed distribution;
3. Calculate the scattering amplitudes ($A(\omega, \zeta_k)$ k=1,N) associated with the randomly chosen flaw sizes.

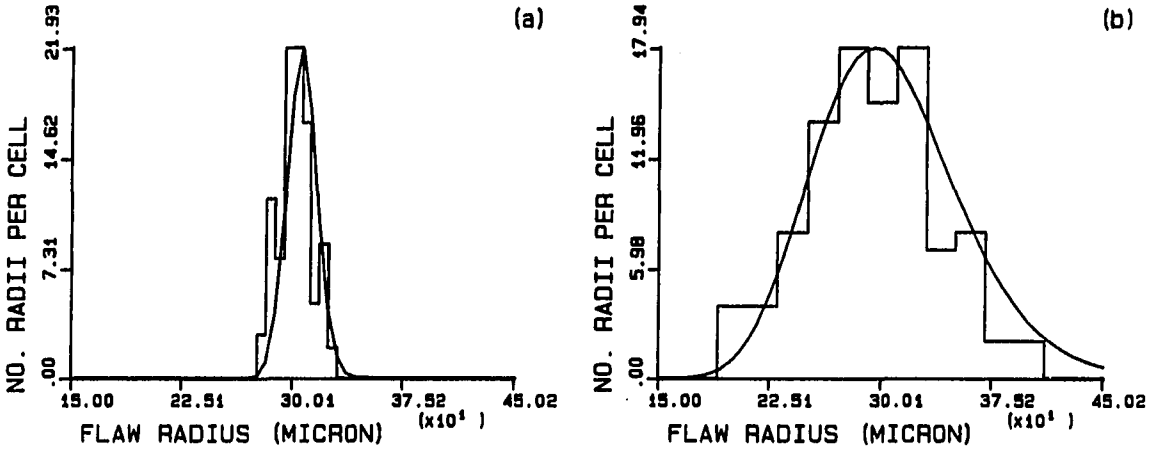

Figure 5.12. Lognormal flaw size distributions. a) m_a=300μm, σ_a=10μm ; b) m_a=300μm, σ_a=50μm

Figure 5.12 represents the results of steps 1 and 2 for two breadths of lognormal distributions of spherical voids in stainless steel. The solid line in Fig. 5.12.a shows the lognormal probability density function associated with a flaw size distribution with m_a=300μm and σ_a=10μm. Superimposed on the graph is a histogram showing the distribution of 100 flaw sizes (N=100). The vertical axis label refers to the histogram. Flaw sizes were determined at random out of the assumed lognormal distribution by using a uniform random number generator which was transformed to yield approximately standard normal random numbers (Kennedy and Gentle 1980) and then transformed again to yield approximately lognormal random numbers (Hahn and Shapiro 1967). Figure 5.12.b gives similar results for a broader distribution with m_a=300μm and σ_a=50μm. Note as demonstrated by the figure, the lower the low coefficient of

variation (σ_a/m_a), the more symmetric and Gaussian the lognormal distribution (Hatch and Choate 1929, Hahn and Shapiro 1967, Haugen 1968).

The scattering amplitude distribution for a lognormal distribution of spherical voids in stainless steel will now be considered at long wavelength for the two flaw distributions shown in Fig. 5.12. The histograms in Fig. 5.13.a and Fig. 5.13.b represent the distributions of the real part ($Re[A(\omega_i,\zeta_k)]$ k=1,100) at 2MHz for flaw size distributions depicted in Fig. 5.12.a (m_a=300μm, σ_a=10μm) and Fig. 5.12.b (m_a=300μm, σ_a=50μm), respectively. Scattering amplitudes were calculated based on the forward solution of Ying and Truell (1956). Note that all values of $Re[A(\omega_i,\zeta_k)]$ are positive. All values of the imaginary part are negative; however, for plotting convenience, the distribution of (-1.0) times the imaginary part ($Im[A(\omega_i,\zeta_k)]$ k=1,100) is shown in Figures 5.13.c and 5.13.d at 2MHz for the two flaw distributions. At 2MHz for flaw radii ranging from 150μm to 450μm, a/λ ranges from 0.025 to 0.078 (ka ranges from 0.16 to 0.49). Superimposed on each histogram is a lognormal probability density function which was determined based on Eq. (5.15). The parameters in Eq. (5.15) were determined by estimating m_A and σ_A^2 (the mean and variance of the lognormal distribution of A) from the histograms and then transforming these values to establish the mean and variance of Log(A) (Haugen 1980).

For each condition represented in Fig. 5.13, the lognormality of the scattering amplitude distribution is verified as the conformance between the histograms and the lognormal probability density functions is excellent. For the narrow flaw distribution, the scattering amplitude distribution (Figures 5.13.a and 5.13.c) are quite symmetric and are

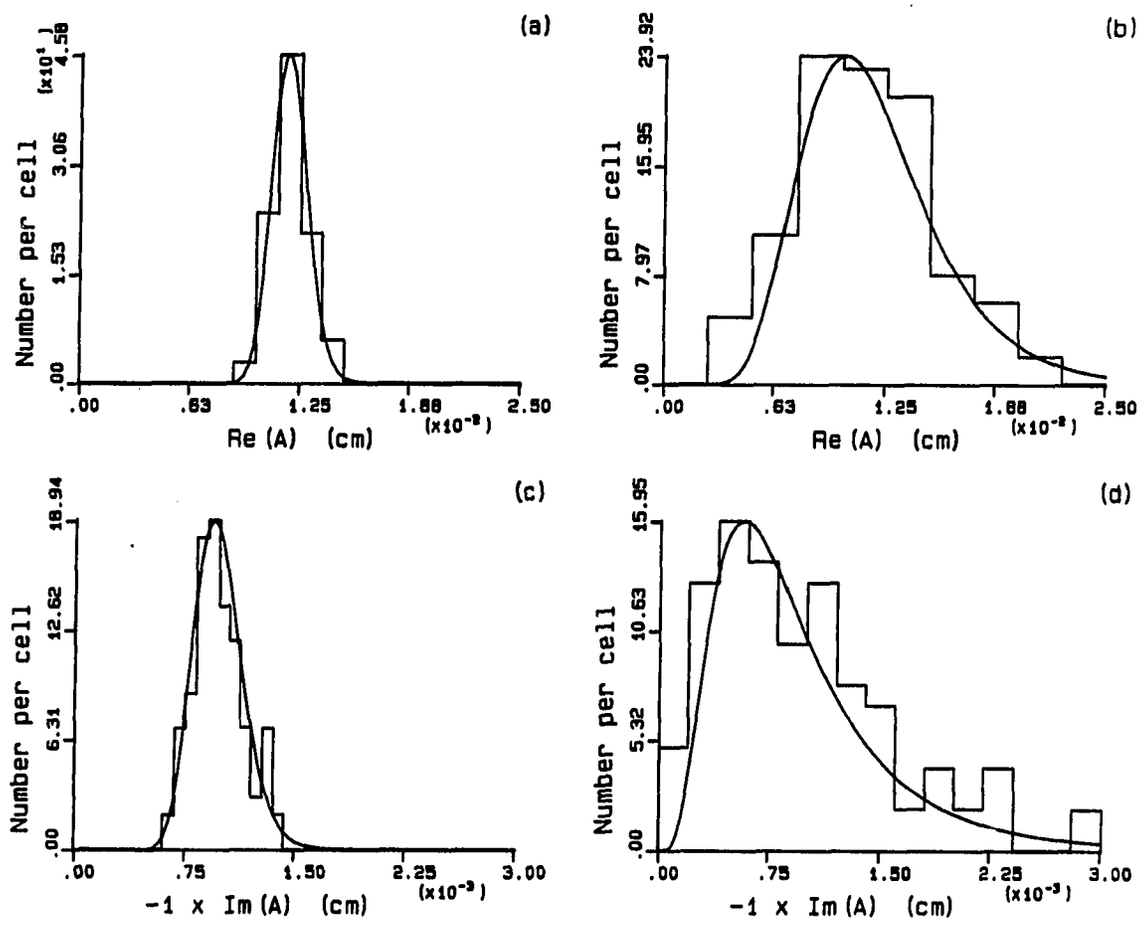

Figure 5.13. Scattering amplitude distribution (long wavelength). a) and c) real and imaginary parts, respectively, at 2MHz for m_a=300μm and σ_a=10μm; b) and d) real and imaginary parts, respectively, at 2MHz for m_a=300μm and σ_a=50μm)

reasonably Gaussian. As the flaw distribution breadth increases, the scattering amplitude distribution (Figures 5.13.b and 5.13.d) becomes less Gaussian. The distribution becomes less Gaussian since it becomes unsymmetric and since the difference between the mode (i.e., the peak in the probability density function) and the scattering amplitude

distribution mean becomes greater. Determining if relatively broad flaw distributions lead to lognormal scattering amplitude distributions which are reasonably Gaussian will be left to the application of the filter (i.e., does the filter work reasonably well for a relatively broad flaw distribution?). As will be discussed in Chapter V, the nature of the optimal Wiener filter is somewhat forgiving in that as the breadth of the flaw distribution increases and the scattering amplitude distribution becomes less Gaussian, the importance of the scattering amplitude mean is deemphasized.

At intermediate and high frequencies, scattering amplitudes have a more complicated and generally oscillatory nature as demonstrated by the figures in Chapter II and by Equations (2.7) and (2.9). In general, the scattering amplitude distribution cannot be determined analytically at these frequencies. In addition, unlike the long wavelength case where the scattering amplitude distribution is lognormal independent of the mean and breadth of the flaw distribution, at intermediate and high frequencies, the sinusoidal nature of scattering amplitudes dictates that the nature of the scattering amplitude distribution will be a function of the mean and the breadth of the flaw distribution. This concept can be clarified by considering a Born scatterer at high frequencies (Eq. (2.9)). If the flaw distribution is narrow, then cos(2ka) will vary over only a small portion of one period, resulting in a narrow, unimodal scattering amplitude distribution (i.e., a distribution whose probability density function has only one peak). If the flaw distribution is broad enough so that cos(2ka) varies over more than one period, then a different (potentially bimodal) distribution will result. Note that part of the complexity is due to the

lognormal flaw size distribution. If the flaw size distribution were uniform and broad enough to span more than one period, the scattering amplitude distribution would certainly be bimodal. Now consider the effect of the mean of the flaw distribution. For a narrow flaw distribution, if $2km_a$ is approximately an integral multiple of π, the scattering amplitude distribution will be either all positive or all negative. For any flaw distribution breadth, if $2km_a$ is an integral multiple of $\pi/2$, the scattering amplitude distribution will contain both positive and negative values.

The histograms in Fig. 5.14 represent scattering amplitude distributions at 15MHz corresponding to lognormal distributions of spherical voids in stainless steel. As in Fig. 5.13, Figures 5.14.a and 5.14.b give the distribution of the real part for the two flaw distributions represented in Fig. 5.12, and Figures 5.14.c and 5.14.d give the distribution of the imaginary part. Note that the horizontal axis scale is unique for each plot. At 15MHz for a flaw radius range from 150μm to 450μm, ka ranges from 2.4 to 7.35. For the narrow flaw distribution, the scattering amplitude distributions (Figures 5.14.a and 5.14.c) appear to be unimodal, and the distribution of the imaginary part (Fig. 5.14.c) is relatively symmetric. For the broader flaw distribution, the scattering amplitude distributions (Figures 5.14.b and 5.14.d) are unsymmetric and show some bimodal tendencies. The bottom line observations relative to the scattering amplitude distributions given in Fig. 5.14 are 1) the nature of the distribution is a function of the flaw distribution, 2) the distribution is certainly not Gaussian, 3) for a

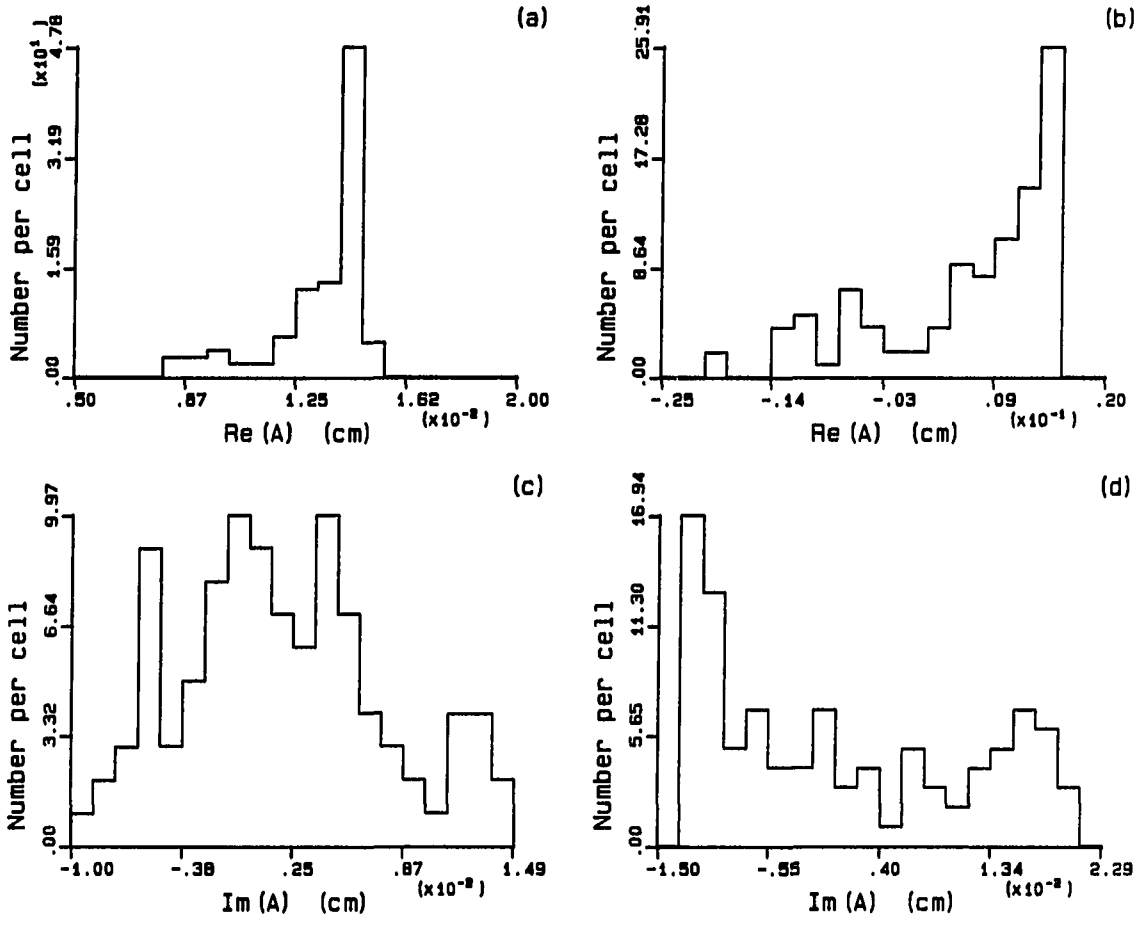

Figure 5.14. Scattering amplitude distribution (intermediate frequency). a) and c) real and imaginary parts, respectively, at 15MHz for m_a=300μm and σ_a=10μm; b) and d) real and imaginary parts, respectively, at 15MHz for m_a=300μm and σ_a=50μm)

narrow flaw distribution the distribution may be reasonably Gaussian, and 4) in general, the distribution is not reasonably Gaussian.

In summary, at long wavelength for a lognormal distribution of volumetric scatterers, scattering amplitude has a lognormal distribution. The extent to which the lognormal distribution is reasonably Gaussian is a

function of the breadth of the flaw distribution. At intermediate and high frequencies, the scattering amplitude distribution corresponding to a lognormal flaw distribution cannot be determined analytically and is, in general, not reasonably Gaussian.

Correlation, mean, and variance Since scattering amplitude is not expected to have zero mean at all frequencies, a sample correlation coefficient will be defined based on Eq. (3.4). For computational convenience, Eq. (3.4) can be written as (Hahn and Shapiro 1967)

$$\rho_z = \frac{E[xy] - m_x m_y}{\sigma_x \sigma_y} \tag{5.19}$$

Based on this form, the sample correlation coefficient at the i^{th} frequency can be defined in scattering amplitude terms as

$$\bar{\rho}(\omega_i) = \frac{\frac{1}{N}\sum_{k=1}^{N} \mathrm{Re}[A(\omega_i,\zeta_k)]\ \mathrm{Im}[n(\omega_i,\zeta_k)] - \bar{m}_{Re}(\omega_i)\ \bar{m}_{Im}(\omega_i)}{\bar{\sigma}_{Re}(\omega_i)\ \bar{\sigma}_{Im}(\omega_i)} \tag{5.20}$$

The sample mean for the real part (see Eq. (5.3)) is given by

$$\bar{m}_{Re}(\omega_i) = \mathrm{Re}[\bar{m}_A(\omega_i)] = \frac{1}{N}\sum_{k=1}^{N} \mathrm{Re}[A(\omega_i,\zeta_k)] \tag{5.21}$$

The sample mean for the imaginary part can be similarly defined. The sample standard deviation for the real part is given by

$$\bar{\sigma}_{Re}(\omega_i) = \sqrt{\frac{1}{N}\sum_{k=1}^{N} \mathrm{Re}[A(\omega_i,\zeta_k)]^2 - \bar{m}_{Re}(\omega_i)} \tag{5.22}$$

The sample standard deviation for the imaginary part can be similarly defined. Finally, the sample variance is equal to the sum of the squares of the sample standard deviations (see Eq. (3.3)) and can be written as

$$\bar{\sigma}_A^2(\omega_i) = \bar{\sigma}_{Re}^2(\omega_i) + \bar{\sigma}_{Im}^2(\omega_i) \tag{5.23}$$

Representative results will now be presented. Summary comments will be made at the end of the section.

Sample correlation coefficients versus frequency are given in Fig. 5.15.a for the narrow flaw distribution considered above (m_a=300μm, σ_a=10μm) and in Fig. 5.15.b for the broader distribution (m_a=300μm, σ_a=10μm). Results for an even broader distribution with m_a=300μm and σ_a=100μm are given in Fig. 5.15.c. The plots are shown from 0-40MHz. Due to the deterministic nature of scattering amplitudes, the correlation is very structured. For the narrow distribution, the general character of the plot is similar to a plot of the product of the real and imaginary parts of the scattering amplitude for a 300μm radius spherical void in stainless steel. As expected, the correlation is negative at very low frequencies. For the broader flaw distribution depicted in Fig. 5.15.b, the real and imaginary parts are "out of phase" at intermediate and high frequencies, and the correlation coefficient tends to oscillate about zero. As the distribution breadth is increased further (Fig. 5.15.c), the correlation coefficient tends to zero at lower frequencies. Notice that even for the broadest distribution, the correlation is negative at very low frequencies.

Figures 5.16.a and 5.16.b show the sample mean for the real part and the imaginary part, respectively, for the two narrower flaw distributions

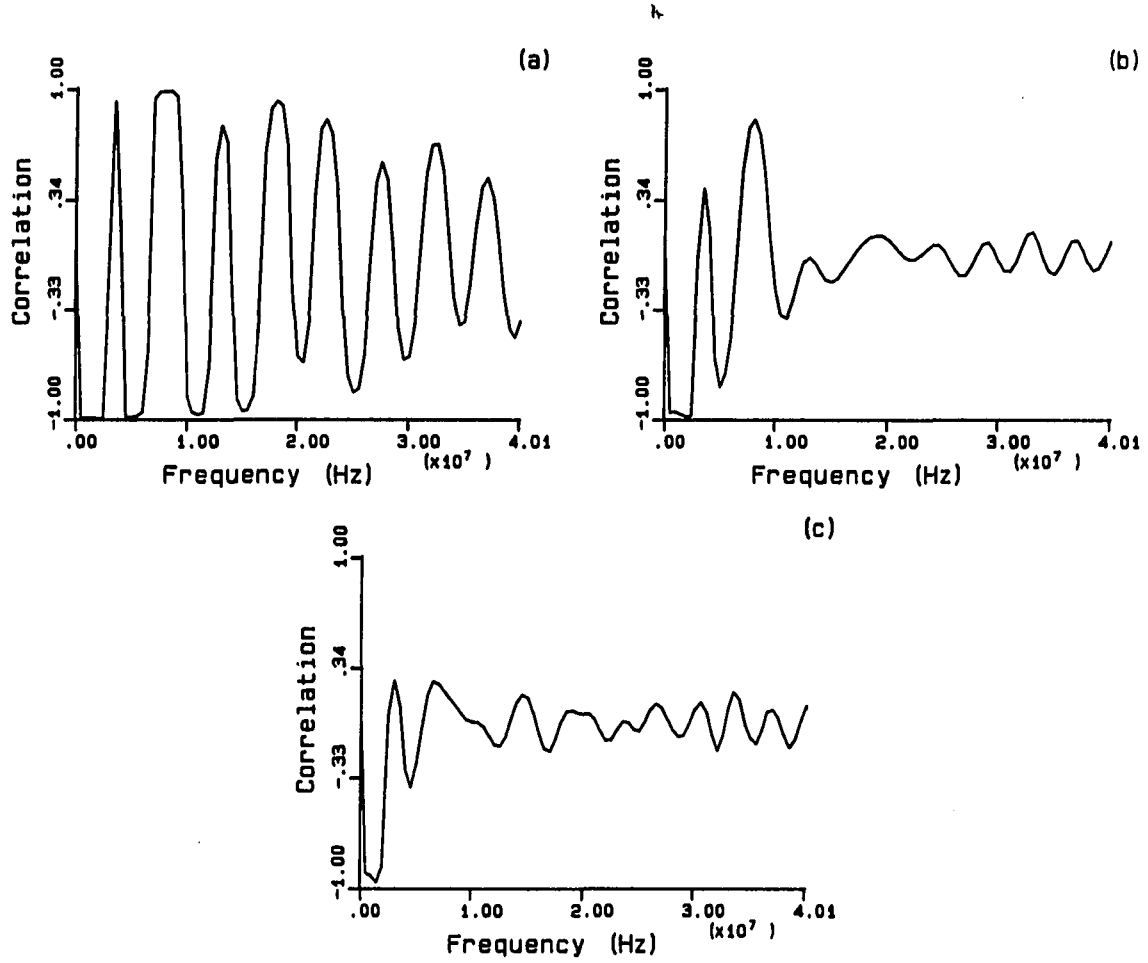

Figure 5.15. Scattering amplitude correlation. a) m_a=300μm and σ_a=10μm; b) m_a=300μm and σ_a=50μm; c) m_a=300μm and σ_a=100μm

considered above. The distribution with σ_a=100μm is considered in Fig. 5.18. The dotted line in each figure represents the appropriate part of the scattering amplitude for a 300μm radius spherical void in stainless steel. The solid line in each figure represents the sample mean for the narrow distribution (m_a=300μm, σ_a=10μm), and the dashed line represents the broader distribution (m_a=300μm, σ_a=50μm). For the narrow

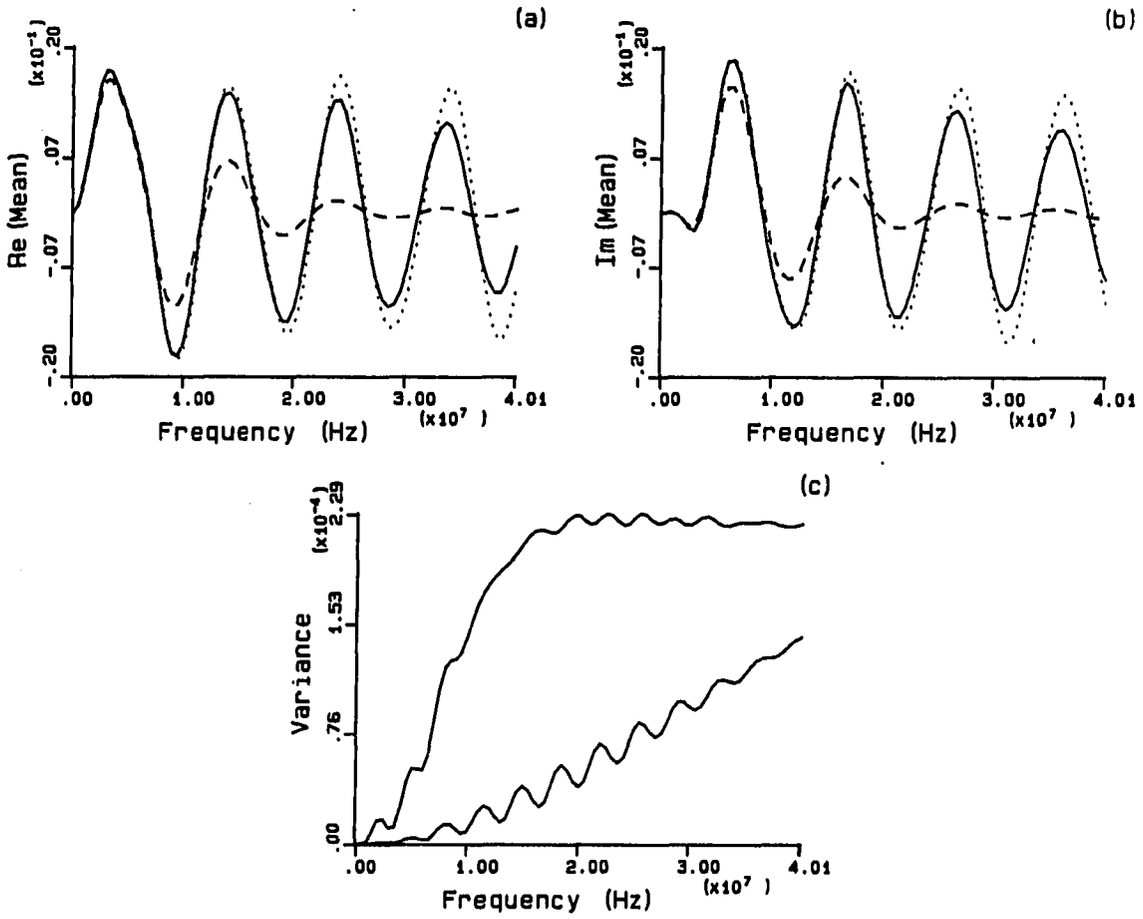

Figure 5.16. Scattering amplitude mean and variance (spherical void). a) and b) sample mean for real part and imaginary part, respectively, with m_a=300μm and σ_a=10μm (solid) and σ_a=50μm (dashed) (the dotted line is $A(\omega)^a$ for a=300μm); c) sample variance for m_a=300μm and σ_a=10μm (lower curve) and σ_a=50μm (upper curve)

distribution, the scattering amplitude mean (solid line) approaches the scattering amplitude for a flaw with radius equal to the mean radius (dotted line). This is especially evident at low frequencies where scattering amplitudes for different flaw sizes are "in phase". At higher

frequencies, scattering amplitudes become "out of phase" and cancelation begins to force the mean toward zero. This is somewhat evident even for the narrow distribution in the 20-40MHz range. For the broader distribution (dashed line), scattering amplitudes become "out of phase" sooner (i.e., at lower frequencies). This is shown by the figures as the mean oscillates about zero at high frequencies and some cancelation is evident even below 10MHz.

The sample variance for the two flaw distribution is shown in Fig. 5.16.c. The lower curve is for the narrow distribution (σ_a=10μm) and the upper curve is for the broader distribution (σ_a=50μm). This figure also shows the anticipated results. That is, the variance increases with increasing frequency as the scattering amplitudes for different flaw sizes effectively get "out of phase". Also, at a particular frequency, the scattering amplitude variance increases as the flaw distribution breadth increases.

The scattering amplitude for a tin-solder sphere in thermoplastic contains detailed or "noise-like" features (Fig. 2.2.f). Consider two lognormal distributions of tin-solder spheres in thermoplastic with m_a=300μm for both distributions. The solid lines in Figures 5.17.a and 5.17.b are the sample mean for the real part of the scattering amplitude corresponding to flaw distributions with σ_a=50μm and σ_a=100μm, respectively. The dashed line in each plot is $A(\omega)$ for a tin-solder sphere in thermoplastic with a=300μm. First, notice that the mean tends to zero except at low frequency. For the broader distribution (Fig. 5.17.b) which was not considered in the previous figure, the mean approaches zero well below 5MHz. The main point of the figure is that

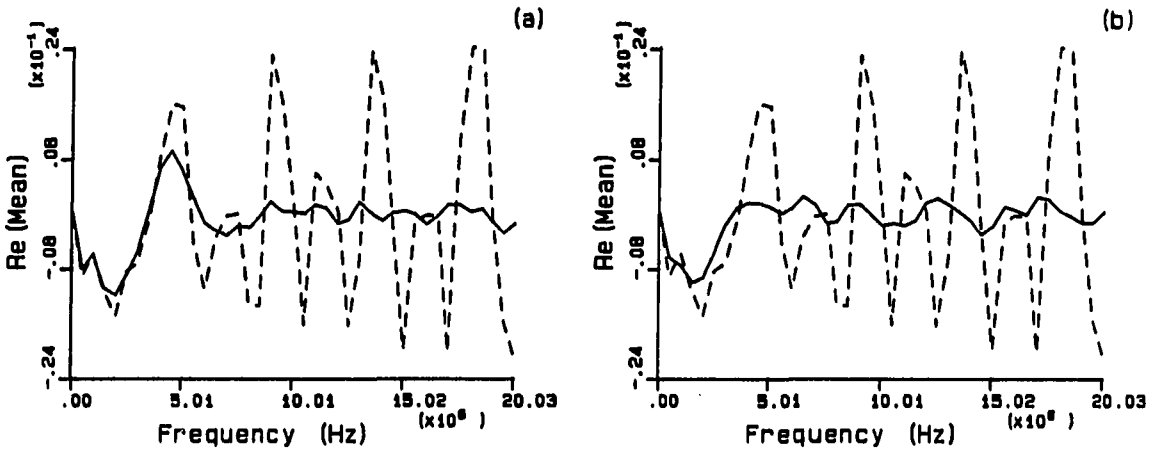

Figure 5.17. Scattering amplitude mean (tin-solder sphere). a) σ_a=50μm (solid); b) σ_a=100μm (solid) (the dashed line is $A(\omega)$ for a=300μm

detailed features in scattering amplitudes will, in general, not be reproduced in the scattering amplitude mean. As demonstrated by the figure, even a low frequencies where the scattering amplitude mean does not go to zero, averaging tends to eliminate the detailed features. In the next chapter, it is shown that the optimal Wiener filter utilizes the scattering amplitude mean. Therefore, if detailed features are important in flaw characterization, it is important to be aware that these features will, in general, not be present in the scattering amplitude mean.

The situation where the characterization of the flaw distribution is not correct will now be considered. Again, consider a lognormal distribution of spherical voids in stainless steel. Assume, for instance, that the actual flaw distribution is correctly characterized with m_a=300μm and σ_a=50μm. Further, assume that the distribution has been incorrectly

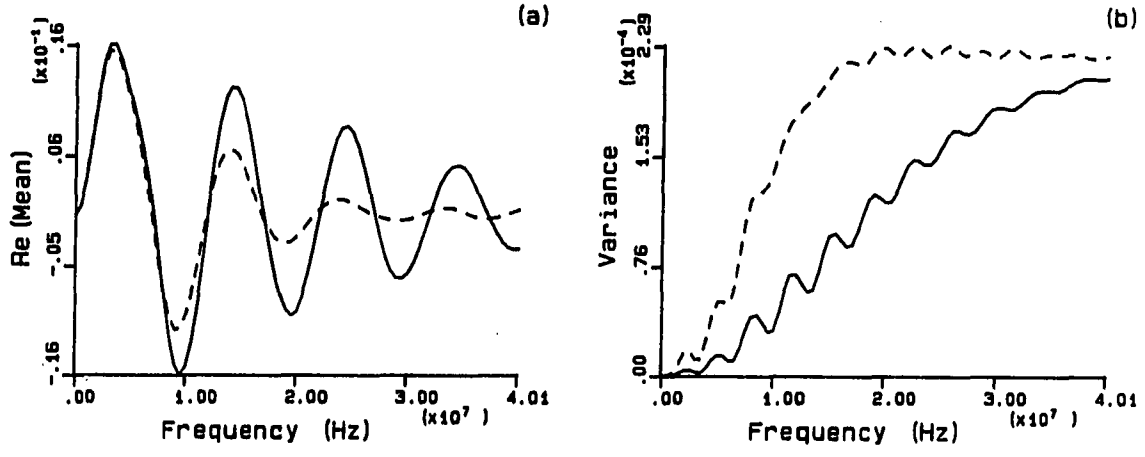

Figure 5.18. Scattering amplitude mean and variance (effect of errors). a) and b) sample mean for real part and sample variance, respectively (correct distribution, σ_a=50μm, dashed line; incorrect distribution, σ_a=25μm, solid line)

characterized with σ_a=25μm. Figures 5.18.a and 5.18.b show the sample mean for the real part and the sample variance, respectively, for the correctly characterized distribution (m_a=300μm, σ_a=50μm) in dashed line and for the incorrectly characterized distribution (m_a=300μm, σ_a=25μm) in solid line. These figures demonstrate two points. First, an error in characterizing the flaw distribution breadth has resulted in errors in both the scattering amplitude mean and variance. Likewise, an error in characterizing the flaw distribution mean would cause an error in both the scattering amplitude mean and variance. Second, characterization errors have a greater effect at higher frequencies. That is, at low frequencies, both the scattering amplitude mean and variance are relatively insensitive to flaw distribution characterization errors.

In summary, as demonstrated by Figure 5.15, the deterministic nature of scattering amplitudes dictates that 1) the real and imaginary parts are not uncorrelated at all frequencies, 2) the extent of the correlation is a function of the flaw distribution, and 3) the correlation is negative at low frequencies for volumetric scatterers. As expected, scattering amplitudes do not have zero mean at all frequencies. Further, the mean tends to the scattering amplitude for the mean flaw size 1) for a narrow flaw distribution at all frequencies and 2) at low frequencies for any breadth of flaw distribution. For broad flaw distributions, the mean tends to zero except at low frequencies. In general, detailed features in scattering amplitudes will not be reflected in the scattering amplitude mean. Scattering amplitude variance increases with frequency and also increases with increasing flaw distribution breadth. Errors in characterization of the flaw distribution show up in both the scattering amplitude mean and variance. At low frequency, the scattering amplitude mean and variance are relatively insensitive to such errors.

CHAPTER VI. FILTER EVALUATION

This chapter focuses on the strengths and weaknesses of the optimal Wiener filter in determining scattering amplitude estimates from noise-corrupted flaw signals. The desensitization filter algorithm (as defined in Chapter II, pp. 43-46) is used as a basis of comparison; therefore, a brief evaluation of this estimation technique is given prior to the evaluation of the optimal Wiener filter. The chapter begins with a section which defines the procedures used in evaluating the filters.

Procedures

Noise-corrupted flaw signals

The initial approach taken in this work was to combine the measured flaw signals and measured noise signals to create noise-corrupted flaw signals from which scattering amplitude estimates could be determined. To provide flexibility in evaluating the optimal Wiener filter, simulated flaw signals were also used in combination with measured noise signals to create noise-corrupted flaw signals.

Signal to noise ratio Since the flaw signal is either simulated or measured separate from the measurement of the noise signals, it is possible to scale the noise prior to adding it to a flaw signal in order to achieve any S/N. In this work, noise signals were scaled to achieve the desired average S/N over the flaw and noise ensemble being considered. That is, a scale factor, K, was calculated so that a S/N based on the mean flaw size, m_a, and the average noise power was at a specified level. This

average S/N, denoted SN_K, was defined in the frequency domain as the ratio of the square root of the power in a noise-free flaw signal for a flaw with radius equal to m_a to the square root of the estimated average noise power (Addison et al. 1982). In equation form, SN_K can be written as

$$SN_K = \frac{\sqrt{\sum_{i=1}^{M} |H(\omega_i)A(\omega_i, \zeta_\mu)|^2}}{K \sqrt{\sum_{i=1}^{M} E[n^2(\omega_i)]}} \qquad (6.1)$$

where $A(\omega, \zeta_\mu)$ is the calculated scattering amplitude for a flaw with radius equal to m_a, $E[n^2(\omega_i)]$ is the estimated average noise power (previously written as $\bar{\sigma}_n^2(\omega)$ and defined in Eq. (5.4)), and the power is summed from 0 frequency to the upper limit of the bandwidth, f_{max} (see page 43). From Eq. (6.1), K, is calculated so that SN_K will be equal to the desired average S/N. It is to be noted that since K is calculated based on the average flaw size, a time domain S/N calculated for each noise-corrupted flaw signal in a family of flaw signals would tend to decrease from the signal for the largest flaw to the signal for the smallest flaw.

Simulated flaw signals Consider the creation of noise-corrupted flaw signals using noise-free simulated flaw signals and measured acoustic noise signals. Assume that as preliminary steps: 1) $H(\omega)$ has been calculated (as discussed below); 2) the mean, m_a, and standard deviation, σ_a, associated with the lognormal flaw distribution have been established; 3) the acoustic noise type to be used has been selected; and 4) the scale factor, K, has been calculated. The steps stated below were then repeated

N times to create a family of noise-corrupted flaw signals as represented by $F(t,\zeta_k)$ (k=1,N). For the k^{th} flaw, the noise-corrupted flaw signal was generated as follows:

1. Select a measured acoustic noise signal, $n^r(t,\zeta_j)$, corresponding to the j^{th} grid position where the grid position is selected at random out of the possible grid position for the chosen type of acoustic noise (the number of grid positions available for each type of acoustic noise is defined in Table 4.1). The superscript, r, indicates that the noise is "as measured" and includes transducer ringing noise (see Eq. (4.6)).
2. Multiply the noise signal by K.
3. Generate a flaw radius at random out of the assumed lognormal distribution.
4. Calculate the scattering amplitude, $A(\omega,\zeta_k)$, corresponding to the k^{th} randomly chosen radius (Ying and Truell 1956).
5. Create a noise-free simulated flaw signal by convolving $A(\omega,\zeta_k)$ with $H(\omega)$ followed by an IFT. For the k^{th} flaw, the noise-free flaw signal can be written as

$$F(t,\zeta_k)^{\text{noise-free}} = \text{IFT}\{\, H(\omega)A(\omega,\zeta_k) \,\} \qquad (6.2)$$

7. Add the scaled noise signal to the noise-free flaw signal to create a noise-corrupted flaw signal. For the k^{th} flaw, the noise-corrupted flaw signal can be written as

$$F(t,\zeta_k)^{\text{noise-corrupted}} = F(t,\zeta_k)^{\text{noise-free}} + K\, n^r(t,\zeta_j) \qquad (6.3)$$

where the noise-free signal is simulated and the noise is measured acoustic noise.

When creating a noise-free simulated flaw signal, $H(\omega)$ must be calculated and convolved with a calculated scattering amplitude as in step 5 above. In this work, $H(\omega)$ was calculated based on the type of acoustic noise being used and following the general procedure used to estimate $H(\omega)$ associated with the measured flaw signals as discussed in Chapter IV. In particular, a reference signal, $F_R(\omega)$ (see Eq. (4.7)), was determined based on the measurement of a front surface reflection from the noise sample for the type of acoustic noise being used. Propagation effects associated with the reference experiment, $P_R(\omega)$, were calculated. Propagation effects associated with the flaw signal, $P_f(\omega)$, were calculated assuming that a flaw were at the center of the measurement interval for the type of acoustic noise being used. The measurement system response, $H(\omega)$, was then calculated per Eq. (4.9) as $F_R(\omega)[P_f(\omega)/P_R(\omega)]$. Note that since the exact $H(\omega)$ which is used to create noise-corrupted flaw signals is also used in estimating scattering amplitudes from the flaw signals, the detailed nature of $H(\omega)$ is not critical. The important point is that the simulated flaw signals and measured acoustic noise signals lie within approximately the same bandwidth. This is assured by the procedure described above since the same transducer, water path, and instrument settings used to measure the acoustic noise were used to measure the reference signal.

Measured flaw signals In the previous section, step 2 specified that a scattering amplitude should be calculated for exactly the randomly generated radius. When using the set of 10 measured flaw signals as a

base for creating a family of noise-corrupted flaw signals, the randomly generated radius will typically not be equal to the radius of one of the polystyrene spheres (see Table 4.2). Therefore, the flaw signal for the randomly generated radius was approximated by the measured flaw signal from the polystyrene sphere whose radius was nearest the randomly generated radius.

A family of noise-corrupted flaw signals was generated using measured flaw signals and measured noise signals per the steps listed below. Again, assume that m_a and σ_a have been established and K has been calculated (Eq. (6.1)). Only case 2 acoustic noise was used with the measured flaw signals since this noise was measured with the same transducer used to measure the flaw signals. For the k^{th} flaw, the noise-corrupted flaw signal was generated as follows:

1. Select a case 2 acoustic noise signal, $n^r(t,\zeta_j)$, corresponding to the j^{th} grid position where the grid position is selected at random out of the 36 grid positions (see Table 4.1) for case 2 acoustic noise.
2. Multiply the noise signal by K (Eq. (6.3)).
3. Generate a flaw radius at random out of the assumed lognormal distribution.
4. Determine which of the 10 polystyrene spheres has radius nearest the randomly generated radius.
5. Add the scaled noise signal to the time-shifted (see Chapter IV, pp. 84-87) measured flaw signal from the polystyrene sphere determined in step 4 to create a noise-corrupted flaw signal.

The resultant signal involves an essentially noise-free measured flaw signal and measured acoustic noise.

Filter application

The result of the steps defined above is a family of noise-corrupted flaw signals as represented by $F(t,\zeta_k)$ (k=1,N). The task is to estimate the flaw signature from each signal using the desensitization algorithm and the optimal Wiener filter.

Desensitization filter The desensitization filter algorithm was defined in Chapter II (pp. 43-46). In determining scattering amplitude estimates in this work, only the first two steps in the algorithm (i.e., filtering and low frequency extrapolation) were applied. The third step, high frequency windowing, was treated as an optional step. Here, the high frequency window was applied only as a preliminary step in determining flaw radius estimates via the IBA (see Eq. (4.10)).

When determining a scattering amplitude estimate from a noise-corrupted flaw signal which is based on a measured flaw signal, the measurement system response estimate, $\hat{H}(\omega)$, determined as discussed in Chapter V, was utilized. With the desensitization constant, Q, set equal to 10% of $|\hat{H}(\omega)|_{max}$, the scattering amplitude estimate at the i^{th} frequency for the k^{th} flaw determined by the filtering step can be written as (see Equations (2.46) and (2.47))

$$\hat{A}(\omega_i,\zeta_k) = W(\omega_i)\left[\frac{F(\omega_i,\zeta_k)\,\hat{H}^*(\omega_i)}{|\hat{H}(\omega_i)|^2}\right] \qquad (6.4)$$

where the filter term is given by

$$W(\omega_i) = \frac{\dfrac{|\hat{H}(\omega_i)|^2}{0.01\ |\hat{H}(\omega)|^2_{max}}}{\dfrac{|\hat{H}(\omega_i)|^2}{0.01\ |\hat{H}(\omega)|^2_{max}} + 1} \tag{6.5}$$

Low frequency extrapolation is then performed in an automated fashion as defined in Chapter II.

When determining scattering amplitude estimates from noise-corrupted signals created with simulated flaw signals, application of the desensitization filter algorithm is as defined above with the subtle difference that $H(\omega)$ is used in place of $\hat{H}(\omega)$. That is, since $H(\omega)$ was used to create the noise-corrupted flaw signal, it is known exactly, and the estimation step is performed with the exact measurement system response as opposed to an estimate. Since $H(\omega)$ was calculated as described above based on a measured front surface reflection, even though $H(\omega)$ is known exactly, it still contains noise (see Eq. (4.7)).

Optimal Wiener filter In Chapter III, it was shown that noise has zero mean at all frequencies and that the scattering amplitude mean is not equal to zero at all frequencies. Therefore, the evaluation of the optimal Wiener filter will focus on the weighting term form (Eq. (4.21)) where it is assumed that $m_n(\omega)=0$ and $E[A(\omega)]$ is known (see Equations 3.26 and 3.27). Application of the optimal Wiener filter requires an estimate of 1) the measurement system response, $\hat{H}(\omega)$; 2) the scattering amplitude mean, $\bar{m}_A(\omega)$, and variance, $\bar{\sigma}^2_A(\omega)$; and 3) the average noise power, $\bar{E}[n^2(\omega_i)]$. Estimation of these quantities was covered in Chapter V. Given these estimates, the optimal Wiener filter determines a scattering

amplitude estimate at the i^{th} frequency for the k^{th} flaw as (see Equations (3.26) and (3.27))

$$\hat{A}(\omega_i, \zeta_k) = W_1(\omega_i) \left[\frac{F(\omega_i, \zeta_k)\ \hat{H}^*(\omega_i)}{|\hat{H}(\omega_i)|^2} \right] + W_2(\omega_i) \left[\bar{m}_A(\omega_i) \right] \qquad (6.6)$$

where the weighting terms can be written as

$$W_1(\omega_i) = \frac{\dfrac{|\hat{H}(\omega_i)|^2\ \bar{\sigma}_A^2(\omega_i)}{\bar{E}[n^2(\omega_i)]}}{\dfrac{|\hat{H}(\omega_i)|^2\ \bar{\sigma}_A^2(\omega_i)}{\bar{E}[n^2(\omega_i)]} + 1} \qquad W_2(\omega_i) = \frac{1}{\dfrac{|\hat{H}(\omega_i)|^2\ \bar{\sigma}_A^2(\omega_i)}{\bar{E}[n^2(\omega_i)]} + 1} \qquad (6.7)$$

Notice that only the flaw signal and the final scattering amplitude estimate are a function of the flaw being considered (ζ_k). All other quantities are fixed once the flaw and noise distributions are defined. As discussed in the previous section, when simulated flaw signals are used, the measurement system response is known exactly and $H(\omega)$ replaces $\hat{H}(\omega)$ in Equations (6.6) and (6.7). When the measured acoustic noise is scaled by K, the estimate of the average noise power must be scaled by K^2. Thus, when using scaled noise, $K^2\bar{E}[n^2(\omega_i)]$ replaces $\bar{E}[n^2(\omega_i)]$ in Eq. (6.7). Finally, when radius estimates are determined via the IBA, application of the optimal Wiener filter is followed by the high frequency windowing step as defined for the desensitization filter algorithm (pp. 43-46).

Error calculation

As stated in the filter derivation (Chapter III), for Gaussian random variables, finding the most probable scattering amplitude estimate is equivalent to finding the estimate which yields a minimum squared error. Therefore, the results presented later in this chapter utilize an average normalized squared-error between the scattering amplitude estimate and the calculated scattering amplitude as a tool for establishing the quality of scattering amplitude estimates. Since the filter determines an optimum complex scattering amplitude estimate, a total error, e_T, which is the average of the error on the real and imaginary parts was utilized. The total error for a family of flaw signals is defined as

$$e_T = \frac{1}{2}\left[\frac{1}{N}\sum_{k=1}^{N} e_{Re}(\zeta_k) + \frac{1}{N}\sum_{k=1}^{N} e_{Im}(\zeta_k) \right] \tag{6.8}$$

where N is the total number of noise-corrupted flaw signals considered, and $e_{Re}(\zeta_k)$ and $e_{Im}(\zeta_k)$ were calculated from 0 frequency to f_{max} per Eq. (4.11). Notice that this range includes the low frequency extrapolation region below f_{min} (see pp. 43-46).

Flaw radius estimates determined via the IBA (Eq. (4.10) were utilized as a further analysis tool. Both an average percent error, e_a, defined as

$$e_a = \frac{1}{N}\sum_{k=1}^{N} 100\,\frac{\hat{a}_k - a_k}{a_k} \tag{6.9}$$

and an average absolute value of the percent error, $|e_a|$, defined as

$$|e_a| = \frac{1}{N} \sum_{k=1}^{N} \left| 100 \frac{\hat{a}_k - a_k}{a_k} \right| \tag{6.10}$$

were calculated. Here, the correct radius for the k^{th} flaw is a_k and the estimated radius is $\hat{a}_k$. Note that as defined, e_a will be negative when a flaw is undersized.

Overall estimation procedures

With the procedures associated with the major steps stated, the overall procedures can now be defined. By varying certain parameters, the performance of the optimal Wiener filter can be studied for a variety of conditions. In all cases, a finite number of parameters, along with the procedures previously described, completely define the conditions associated with a given family of signals. In the results presented later, parameters which were the same for all cases are 1) the flaw size distribution was lognormal, 2) 100 randomly chosen flaw sizes were used to determine $\bar{m}_A(\omega)$ and $\bar{\sigma}_A^2(\omega)$ (see Chapter V), and 3) 50 noise-corrupted flaw signals (corresponding to 50 randomly chosen flaw sizes) were considered at each condition. Parameters which were varied and therefore must be stated to completely specify a given set of conditions are 1) the flaw distribution mean, m_a; 2) the flaw distribution breadth, specified in terms of the standard deviation, σ_a; 3) the acoustic noise type; and 4) the S/N as defined in Eq. (6.1).

The overall procedure used to determine scattering amplitude estimates and associated errors for a family of signals at a given condition are defined as follows:

1. Calculate $\bar{m}_A$ and $\bar{\sigma}_A^2$ at each frequency.

2. Calculate the scale factor, K (Eq. (6.1).

3. Repeat the following steps 50 times.

   A. Create a noise-corrupted flaw signal using either a simulated or measured flaw signal.

   B. If ringing noise is significant, scale the estimate of the ringing noise, $\hat{n}_r(t)$, by K, and subtract it from the noise-corrupted flaw signal.

   C. Truncate the signal (as discussed below) and take its Fourier transform.

   D. Estimate the scattering amplitude via the desensitization filter algorithm and calculate $e_{Re}(\zeta_k)$ and $e_{Im}(\zeta_k)$ (Eq. (4.11)).

   E. Estimate the scattering amplitude via the optimal Wiener filter and calculate $e_{Re}(\zeta_k)$ and $e_{Im}(\zeta_k)$.

6. Calculate e_T (Eq. (6.8)) associated with the desensitization filter algorithm.

7. Calculate e_T associated with the optimal Wiener filter.

These procedures results in two data points, one associated with each estimation approach, at a given condition. Changing any condition such as S/N, for instance, will result in two additional points. In this manner, plots of e_T versus S/N for each approach can be generated.

As an optional step, IBA radius estimates and associated errors can be calculated for the desensitization filter and for the optimal Wiener filter following steps H and I, respectively. Average radius estimation errors, e_a and $|e_a|$ (Equations (6.9) and (6.10)), can then be calculated for each filter following steps 6 and 7, respectively.

As indicated in step C, prior to the estimation step, each signal was truncated in the time domain and a family of signals in the frequency domain, $F(\omega, \zeta_k)$ (k=1,N), was determined by taking the Fourier transform of each signal. Truncation was done at zero-crossings as defined in Chapter IV. As a standard procedure, it was assumed that the duration of the signal from the flaw would be difficult to determine for low S/N; therefore, the truncation was done the same for all signals such that the middle 1/3 of the time domain signal was included (this approach was routinely followed in analyzing noise in Chapter V).

Desensitization Filter

Qualitative analysis

The behavior of the desensitization filter can be established using frequency dependent S/N concepts. $SN_h(\omega)$, which reflects the stability of the deconvolution, was defined in Eq. (2.29) as $|H(\omega)|/|n_h(\omega)|$. Also, both Murakami et al. (1978) and Furgason et al. (1978) indicated that the desensitization term (denoted Q^2 here) is related to the noise level in the system. If Q^2 is taken to be equal to the average system noise power, $E[n_h^2(\omega)]$, then the expected value of $SN_h(\omega)$ could be defined such that

$$E[SN_h(\omega)]^2 = \frac{|H(\omega)|^2}{E[n_h^2(\omega)]} = \frac{|H(\omega)|^2}{Q^2} \qquad (6.11)$$

The desensitization filter can now be rewritten as

$$\hat{A}(\omega) = \frac{E[SN_h(\omega)]^2}{E[SN_h(\omega)]^2 + 1} \left[\frac{F(\omega)}{H(\omega)}\right] \tag{6.12}$$

As the system response goes to zero, $E[SN_h(\omega)] \rightarrow 0$, the filter term goes to zero, and $\hat{A}(\omega)$ is forced to zero. That is, in the unstable region, the estimate determined by the unconstrained deconvolution is filtered out. In the stable region, $E[SN_h(\omega)]$ is large, the filter term approaches one, and the filter passes the unconstrained deconvolution with measurement system effects successfully removed. In the transitional region, the filter term takes on intermediate values and makes a smooth transition from one to zero (see Fig. 2.4).

As indicated in the previous paragraph, the strength of the desensitization filter is that it acts in a rational manner to provide for the stable removal of measurement system effects. The overriding weakness of the filter is that it passes everything within the bandwidth, including potentially dominant acoustic noise. For discussion purposes, it is instructive to replace $F(\omega)$ in Eq. (6.12) with $H(\omega)A(\omega)+n(\omega)$ to yield

$$\hat{A}(\omega) = W(\omega) \left[A(\omega) + \eta(\omega) \right] \tag{6.13}$$

where $W(\omega)$ is defined in Eq. (6.5) and the noise term, $\eta(\omega)$, is equal to $n(\omega)/H(\omega)$. Within the central region of the bandwidth, $W(\omega)$ approaches 1.0 (see Fig. 2.4) and all noise is passed by the filter. Also, notice that since $A(\omega)$ and $\eta(\omega)$ are filtering in identical fashion, their ratio always remains the same. That is, filtering does not result in an improvement in the S/N at a particular frequency.

The ability of the desensitization filter to remove measurement system effects is demonstrated in Fig 6.1. Figures 6.1.a and 6.1.b show the calculated (Ying and Truell 1956) impulse response function, R(t), and magnitude of the scattering amplitude, $|A(\omega)|$, respectively, for a 109μm radius polystyrene sphere in thermoplastic (flawed specimen fabrication was discussed in Chapter IV). The impulse response function shows a front surface reflection from the flaw, a plateau region, and a back surface reflections from the flaw. Figure 6.1.c shows the measured flaw signal, F(t), from the 109μm radius polystyrene sphere. The magnitude of the measured signal in the frequency domain, $|F(\omega)|$, is shown in Fig. 6.1.d. The measurement system response for this case is that shown in Fig. 2.4.a. Measurement system effects cause distortion of the frequency domain signal (i.e., the positions and relative heights of the peaks in Fig. 6.1.d are not the same as those in Fig. 6.1.b) and a loss of resolution in the time domain (i.e., two distinct reflections and a plateau region are not present in Fig. 6.1.c). Figures 6.1.e and 6.1.f show $\hat{R}(t)$ and $|\hat{A}(\omega)|$ determined by application of the desensitization filter followed by low frequency extrapolation. The impulse response estimate was determined by taking the IFT of $\hat{A}(\omega)$. The distortion present in the frequency domain has been nearly eliminated by the constrained deconvolution. In the time domain, the impulse response function estimate shows greatly improved resolution. The two reflections and plateau region are now clearly visible.

Now consider the weaknesses of the desensitization filter. Figure 6.2 shows noise-corrupted flaw signals and corresponding scattering amplitude estimates for three levels of noise. Each time domain signal

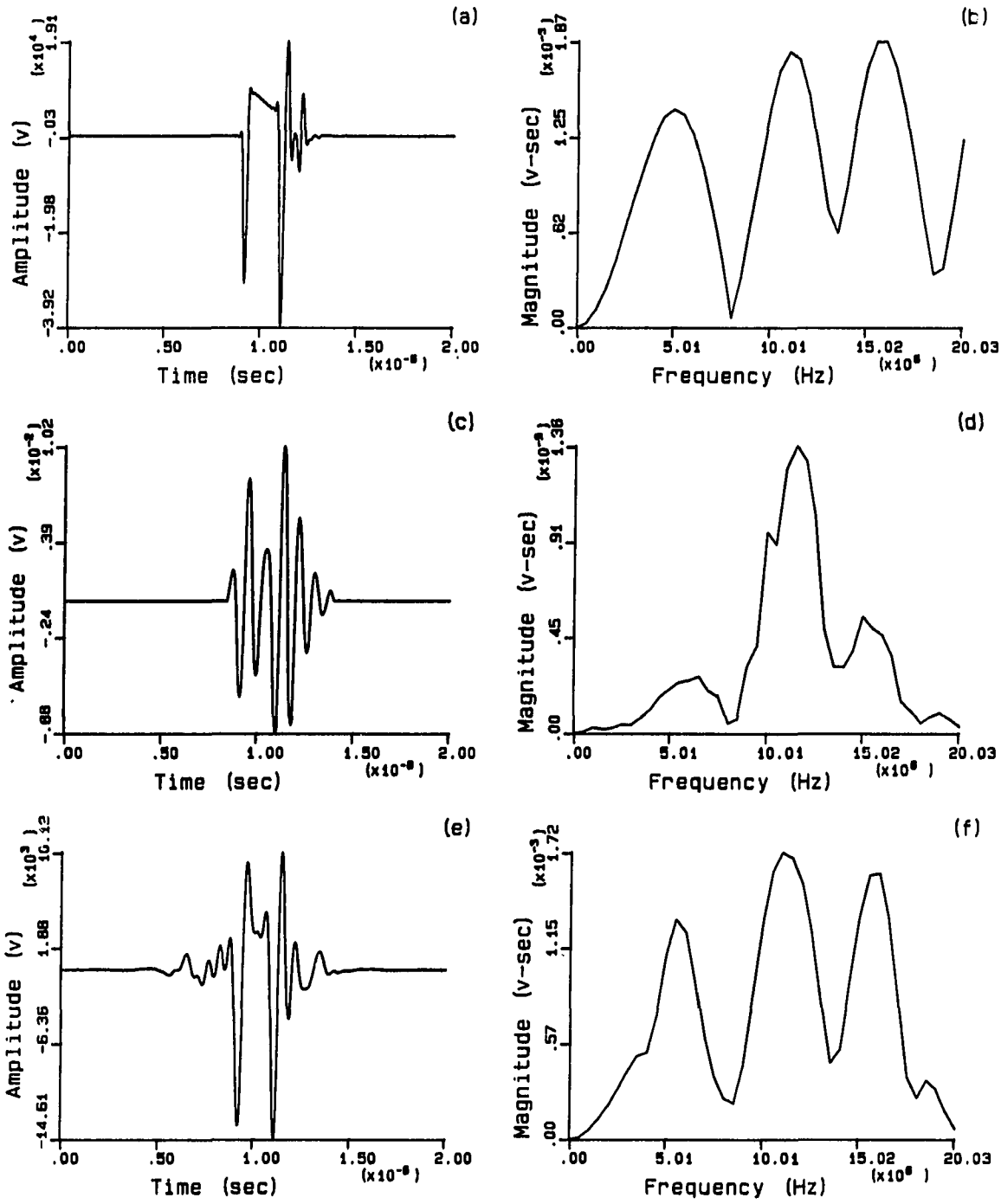

Figure 6.1. Desensitization filter analysis (noise-free case). a) and b) calculated R(t) and $|A(\omega)|$; c) and d) measured flaw signal, F(t), and magnitude spectrum, $|F(\omega)|$; e) and f) $\hat{R}(t)$ and $|\hat{A}(\omega)|$ determined with the desensitization filter

(Figures 6.2.a, 6.2.c, and 6.2.e) shows the flaw signal for the 109μm radius polystyrene sphere in thermoplastic (as shown in Fig. 6.1.c) and a noise-corrupted version of the flaw signal. The noise-corrupted versions were created by adding scaled case 2 acoustic noise to the flaw signal. Expressed in dB ($dB=20Log_{10}(SN_K)$), SN_K equals 20dB, 5dB, and 0dB for the noise-corrupted signals in Figures 6.2.a, 6.2.c, and 6.2.e, respectively. Figures 6.2.b, 6.2.d, and 6.2.f show the calculated $Re[A(\omega)]$ (dashed line) and $Re[\hat{A}(\omega)]$ (solid line) determined via the desensitization filter followed by low frequency extrapolation. For the low noise case (Figures 6.2.a and 6.2.b), the desensitization filter provides a good scattering amplitude estimate. Bandlimitation effects are evident at both low and high frequencies. As the noise level is increased (to the point where the flaw would be very difficult to detect in Fig. 6.2.e), the filter continues to pass the noise and the scattering amplitude estimates becomes dominated by noise.

Considering estimation in the presence of case 3 acoustic noise, which represents a noise source with its strength at low frequencies within the bandwidth, is also instructive. The average power spectrum for this case is shown in Fig. 4.4.d. Figure 6.3.a shows the power (solid line) associated with a single measured case 3 acoustic noise signal. A noise-free simulated flaw signal representing scattering from a 200μm radius spherical void in aluminum was created. The flaw signal was then corrupted with case 3 acoustic noise scaled so that SN_K=5dB. The filter term, $W(\omega)$, for this case is given by the dashed line in Fig. 6.3.a (the vertical scale is for the noise power and $W(\omega)$ varies from 0 to 1.0 as in Fig. 2.4.b). Notice that at frequencies where the acoustic noise is

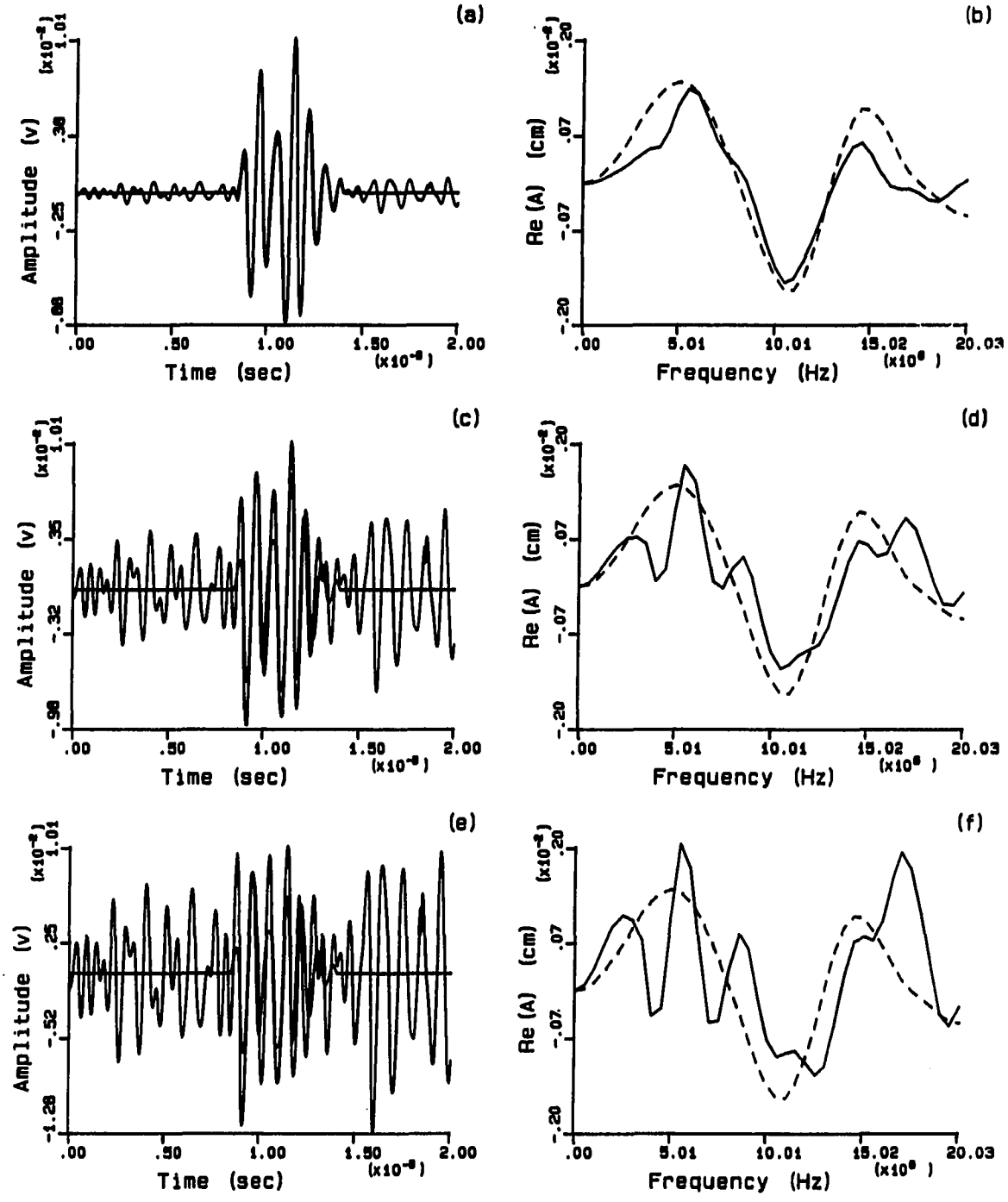

Figure 6.2. Desensitization filter analysis (case 2 acoustic noise). a), c), and e) flaw signals for a 109μm radius polystyrene sphere in thermoplastic corrupted with case 2 acoustic noise; b), d), and f) corresponding scattering amplitude estimates

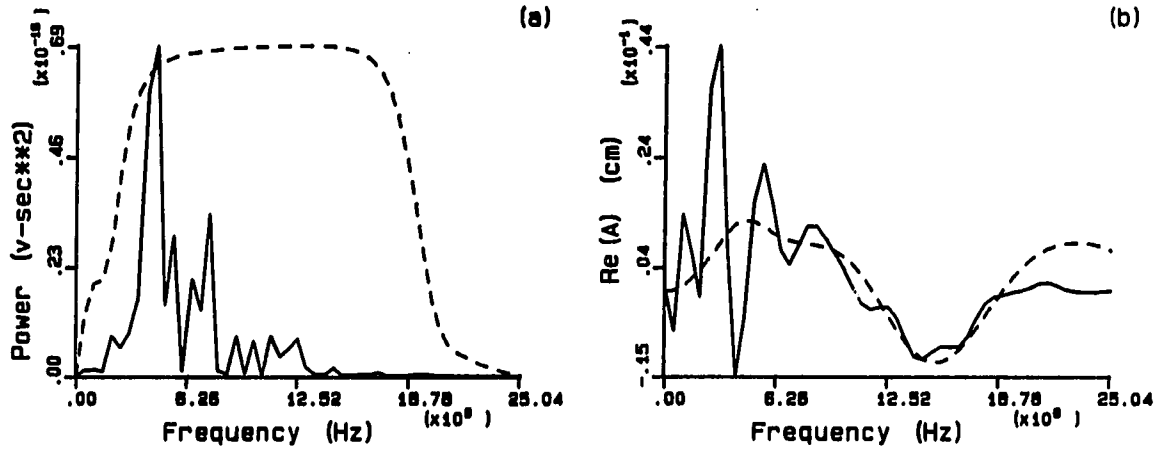

Figure 6.3. Desensitization filter analysis (case 3 acoustic noise). a) noise power spectrum for a single case 3 acoustic noise signal (solid) and $W(\omega)$ (dashed); b) calculated (dashed) and estimated (solid) $Re[A(\omega)]$ for a spherical void in aluminum

strong, $W(\omega)$ approaches its maximum value of 1.0. Shown in Fig. 6.3.b are $Re[\hat{A}(\omega)]$ (solid line) determined using the desensitization filter without low frequency extrapolation and the calculated $Re[A(\omega)]$ (dashed line). Figure 6.3.b again demonstrates the inability of the desensitization filter to filter out acoustic noise. This figure also shows that extrapolation in the presence of low frequency acoustic noise would be very difficult. This is especially true when extrapolation is done in an automated fashion as is the case with the low frequency extrapolation procedure used in the desensitization filter algorithm.

Summarizing, using frequency dependent S/N concepts, the behavior of the desensitization filter in stabilizing the deconvolution has been shown to be related to the source of the instability. The strength of the

desensitization filter algorithm is its ability to remove measurement system effects while stabilizing the deconvolution (Fig. 6.1). The major deficiency of the filter is its insensitivity to acoustic noise (Figures 6.2 and 6.3).

Optimal Wiener Filter

Qualitative analysis

In order to emphasize the differences between the desensitization filter and the optimal Wiener filter, it is useful to consider the constrained deconvolution form of the optimal Wiener filter (Eq. (3.35)) where both the noise and scattering amplitude are assumed to have zero mean. Constrained deconvolution techniques involve some form of constraining term (e.g., $\lambda^2(\omega)$ in Eq. (1.4)). From Eq. (3.35) it is clear that (for the zero mean case) the optimal Wiener filter determines $\lambda^2(\omega)$ at each frequency in an optimal fashion as the ratio of the average noise power divided by the average scattering amplitude power. Since $E[n^2(\omega)]$ includes both electronic and acoustic noise, the constraining term will force the scattering amplitude estimate to zero in regions where the deconvolution is unstable and also in regions where acoustic noise becomes dominant.

With $E[n(\omega)]=0$ and $E[A(\omega)]=0$, the optimal Wiener filter can be written in terms of the expected value of $SN_f(\omega)$. $SN_f(\omega)$ was defined in Eq. (2.30) as $|H(\omega)||A(\omega)|/|n(\omega)|$. Therefore, $E[SN_f(\omega)]$ can be defined such that

$$E[SN_f(\omega)]^2 = \frac{|H(\omega)|^2 \, E[A^2(\omega)]}{E[n^2(\omega)]} \tag{6.14}$$

Combining Equations (3.28), (3.29), and (6.14), the filter can be written as (Neal and Thompson 1986)

$$\hat{A}(\omega) = \frac{E[SN_f(\omega)]^2}{E[SN_f(\omega)]^2 + 1} \left[\frac{F(\omega)}{H(\omega)}\right] \tag{6.15}$$

This form is the same as that used in the analyzing the desensitization filter in terms of $E[SN_h(\omega)]$ (Eq. (6.12)). For the optimal Wiener filter, unlike the desensitization filter, the filter term is controlled by the expected S/N at each frequency for the ensemble of noise-corrupted flaw signals. The filter is therefore sensitive to acoustic noise as reflected in the behavior of the filter. For low S/N, whether due to electronic noise and indicating instability or due to acoustic noise dominance, the filter term goes to zero and $\hat{A}(\omega)$ is forced to zero (i.e., the constrained deconvolution result is filtered out). For high S/N, the filter term approaches one and the estimate determined by the unconstrained deconvolution is passed. Note that while the optimal Wiener filter is sensitive to acoustic noise and attempts to prevent a scattering amplitude estimate from being dominated by noise, it does not extract the true scattering amplitude from noise-corrupted data, nor does it improve the S/N at any frequency. In this respect, it is the same as the desensitization filter (see Eq. (6.13)).

The remainder of the work in this dissertation will focus on the weighting term form of the optimal Wiener filter where it is assumed that

$E[n(\omega)]=0$ and $E[A(\omega)]$ is known (see Equations 3.26 and 3.27). This form shows that, at each frequency, the filter utilizes prior information to determine an optimal estimate as the weighted average of the unconstrained deconvolution, $F(\omega)/H(\omega)$, and the scattering amplitude mean, $E[A(\omega)]$. In other words, the filter uses two pieces of information: 1) that which is contained within $F(\omega)/H(\omega)$ and was learned from the ultrasonic interrogation of the flaw, and 2) prior knowledge of the flaw distribution as represented by $E[A(\omega)]$. In order to emphasize this concept, henceforth, the unconstrained deconvolution, $F(\omega)/H(\omega)$, will be referred to as the experimental result (Neal and Thompson 1987). The weighting term form also shows that the second term, $W_2(\omega)E[A(\omega)]$, essentially provides for a scattering amplitude estimate in regions were $W_1(\omega)$ has forced the experimental result to zero. Therefore, in principle, the filter provides for estimation outside of the bandwidth, and also provides for an estimate in regions within the bandwidth were acoustic noise is dominant.

In order to understand the filter, the weighting terms could be written in terms of an average frequency dependent S/N. In doing this, $W_1(\omega)$ would be of the form of the filter term given in Eq. (6.15) and $W_2(\omega)$ would be equal to $1-W_1(\omega)$. Such an analysis would indicate that for a favorable S/N, $W_1(\omega)\rightarrow 1$ ($W_2(\omega)\rightarrow 0$) and the experimental result is emphasized ($E[A(\omega)]$ is deemphasized). When the S/N is unfavorable, indicating that the experimental result is dominated by noise (either electronic noise outside of the bandwidth or acoustic noise within the bandwidth), $W_1(\omega)\rightarrow 0$ ($W_2(\omega)\rightarrow 1$) and the experimental result is deemphasized ($E[A(\omega)]$ is emphasized).

The filter can also be understood by considering the behavior of the weighting terms with respect to variations in the individual terms ($|H(\omega)|^2$, $\sigma_A^2(\omega)$, and $E[n^2(\omega)]$) which control the weighting terms (Neal and Thompson 1987). Outside of the bandwidth (i.e., as $|H(\omega)|$ goes to zero) $W_1(\omega) \rightarrow 0$ and $W_2(\omega) \rightarrow 1$ (this behavior is demonstrated by the graphical examples given in Figures 6.4 and 6.5). Thus, at frequencies where no experimental information is available, the experimental result is not used and $\hat{A}(\omega)$ is determined by $E[A(\omega)]$. As the center of the bandwidth is approached and $H(\omega)$ increases, the weighting terms shift the emphasis from $E[A(\omega)]$ to the experimental result.

The filter's reaction to acoustic noise is as follows. At frequencies where the experimental result is on the average dominated by noise (i.e., $E[n^2(\omega)]$ is large relative to $|H(\omega)|^2\sigma_A^2(\omega)$), the experimental result is deemphasized and $E[A(\omega)]$ is emphasized. If the noise level is reduced indicating that the quality of the experimental result is improved, $W_1(\omega)$ increases in order to place more emphasis on the experimental result. This behavior is demonstrated in Figures 6.4. The solid lines in Figures 6.4.a and 6.4.b are $W_1(\omega)$ and $W_2(\omega)$, respectively, for various signal to noise ratios. Defined in terms of SN_K, the signal to noise ratios represented are (going from top to bottom in Fig. 6.4.a and from bottom to top in Fig. 6.4.b) 20dB, 10dB, 5dB, 0dB, -5dB, and -10dB. The assumed flaw distribution is a lognormal distribution of polystyrene spheres in thermoplastic. The measurement system response is as given in Fig. 2.4.a. Figures 6.4.a and 6.4.b demonstrate that as the S/N decreases, indicating that the experimental result in becoming more noise-corrupted, $W_1(\omega)$ decreases and $W_2(\omega)$ increases. Notice that

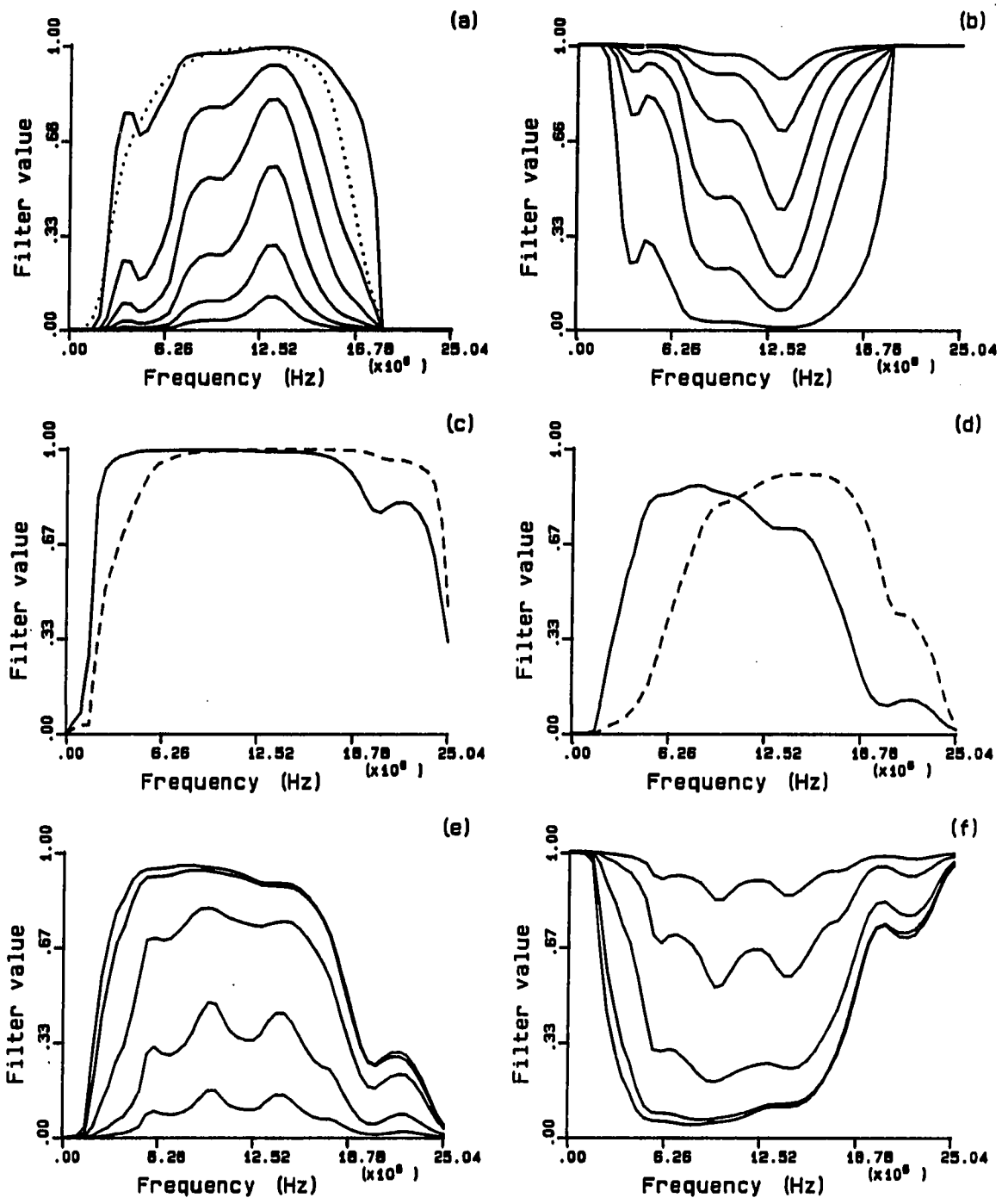

Figure 6.4. Optimal Wiener filter (weighting term variations). a) and b) S/N effects; c) and d) noise frequency dependence effects; e) and f) flaw distribution breadth effects

regardless of the value of SN_K, $W_1(\omega)$ is equal to zero and $W_2(\omega)$ is equal to one outside of the bandwidth. The dotted line in Fig. 6.4.a is the desensitization filter term as shown in Fig. 2.4.b. For the 20dB case, the desensitization filter term is very similar to $W_1(\omega)$ for the optimal Wiener filter.

An important feature of the optimal Wiener filter is its sensitivity to the frequency dependence of the noise. This sensitivity is demonstrated by the plots of $W_1(\omega)$ shown in Figures 6.4.c and 6.4.d. The solid line in each figure represents $W_1(\omega)$ for the simulation of flaws in the case 1 acoustic noise sample (ASTM 8 stainless steel). The dashed lines in the figures represent $W_1(\omega)$ for the simulation of flaws in the case 3 acoustic noise sample (aluminum with 2% porosity). In both cases, a lognormal distribution of spherical voids is assumed with m_a=200μm and σ_a=30μm. As demonstrated in Fig. 4.4, case 1 acoustic noise has its maximum strength at high frequencies within the bandwidth while case 3 acoustic noise has its strength at low frequencies. Figure 6.4.c represents the 20dB case where both types of acoustic noise are negligible; therefore, the filter terms essentially act as bandpass filters. Figure 6.4.d represents a lower S/N (0dB) where the acoustic noise is dominant over a portion of the bandwidth in both cases. As demonstrated in the figure, $W_1(\omega)$ for case 1 acoustic noise (solid line) shows rapid drop-off at high frequencies, thus filtering out the high frequency acoustic noise. For case 3 acoustic noise (dashed line), $W_1(\omega)$ is decreased at low frequency in order to filter out the low frequency noise.

The behavior of the filter with respect to the breadth of the flaw distribution is more subtle. A narrow flaw distribution (i.e., small $\sigma_A^2(\omega)$) implies that $A(\omega)$ for most of the flaws in the ensemble will vary only slightly from the mean, $E[A(\omega)]$. Thus, for a narrow flaw distribution, $W_2(\omega)$ is large so that $\hat{A}(\omega)$ is determined primarily by $E[A(\omega)]$. A broad flaw distribution (i.e., large $\sigma_A^2(\omega)$) implies that $A(\omega)$ for many of the flaws in the ensemble will vary only significantly from $E[A(\omega)]$. Thus, for a broad flaw distribution, the weighting terms shift the emphasis from $E[A(\omega)]$ to the experimental result. This behavior is demonstrated by the plots of $W_1(\omega)$ and $W_2(\omega)$ shown in Figures 6.4.e and 6.4.f, respectively, for various flaw distribution breadths. In each case, a lognormal distribution of polystyrene spheres in thermoplastic with m_a=250μm is assumed. Flaw distribution breadths (σ_a) represented in the figures are (from top to bottom in Fig. 6.4.e and from bottom to top in Fig. 6.4.f) 5μm, 10μm, 25μm, 50μm, and 75μm. As demonstrated by the figures, as the flaw distribution breadth increases, $W_2(\omega)$ decreases in order to place less emphasis on $E[A(\omega)]$ and $W_1(\omega)$ increases in order to place more emphasis on the experimental result. As a final observation, notice that while going from σ_a=50μm to σ_a=75μm represents a significant increase in the flaw distribution breadth, there is an insignificant change in the corresponding weighting terms (the top two curves in Fig. 6.9.e and the bottom two curves in Fig. 6.9.f). Since the weighting terms approach the limits of one and zero asymptotically, seemingly large changes in the parameters which control the weighting terms may result in small changes in the weighting terms (and correspondingly small changes in

scattering amplitude estimation results as discussed later in this chapter) (Neal and Thompson 1988).

Scattering amplitude estimates determined by the optimal Wiener filter will now be considered for the cases used in demonstrating the weaknesses of the desensitization filter. Figure 6.5 shows the weighting terms and $Re[\hat{A}(\omega)]$ for the three signal to noise ratios (20dB, 5dB, and 0dB) considered in Fig. 6.2. Figures 6.5.a, 6.5.c, and 6.5.e show $W_1(\omega)$ in solid line and $W_2(\omega)$ in dashed line. Figures 6.2.b, 6.2.d, and 6.2.f show $Re[\hat{A}(\omega)]$ in solid line and the calculated $Re[A(\omega)]$ in dashed line. Scattering amplitude estimates were determined from the noise-corrupted flaw signals shown in Fig. 6.2. A lognormal distribution of polystyrene spheres in thermoplastic with m_a=110μm and σ_a=10μm was assumed. For the low noise case (Figures 6.2.a and 6.2.b), the estimate determined by the optimal Wiener filter and that determined by the desensitization filter (Fig. 6.2.b) are nearly the same. This is not surprising since Fig. 6.4.a showed that for high S/N the desensitization filter term (dotted line) and $W_1(\omega)$ (top solid line) are nearly the same. The most significant difference between the optimal Wiener filter estimate and the desensitization filter estimate is in the low frequency extrapolation area where the second term, $W_2(\omega)E[A(\omega)]$, in the optimal Wiener filter has eliminated the bandlimitation effects which are evident in the estimate determined by the desensitization filter. As will be demonstrated in Fig. 6.7, the near perfect match between $Re[A(\omega)]$ and $Re[\hat{A}(\omega)]$ at low frequencies is due to the fact that the flaw size being considered is nearly equal to m_a.

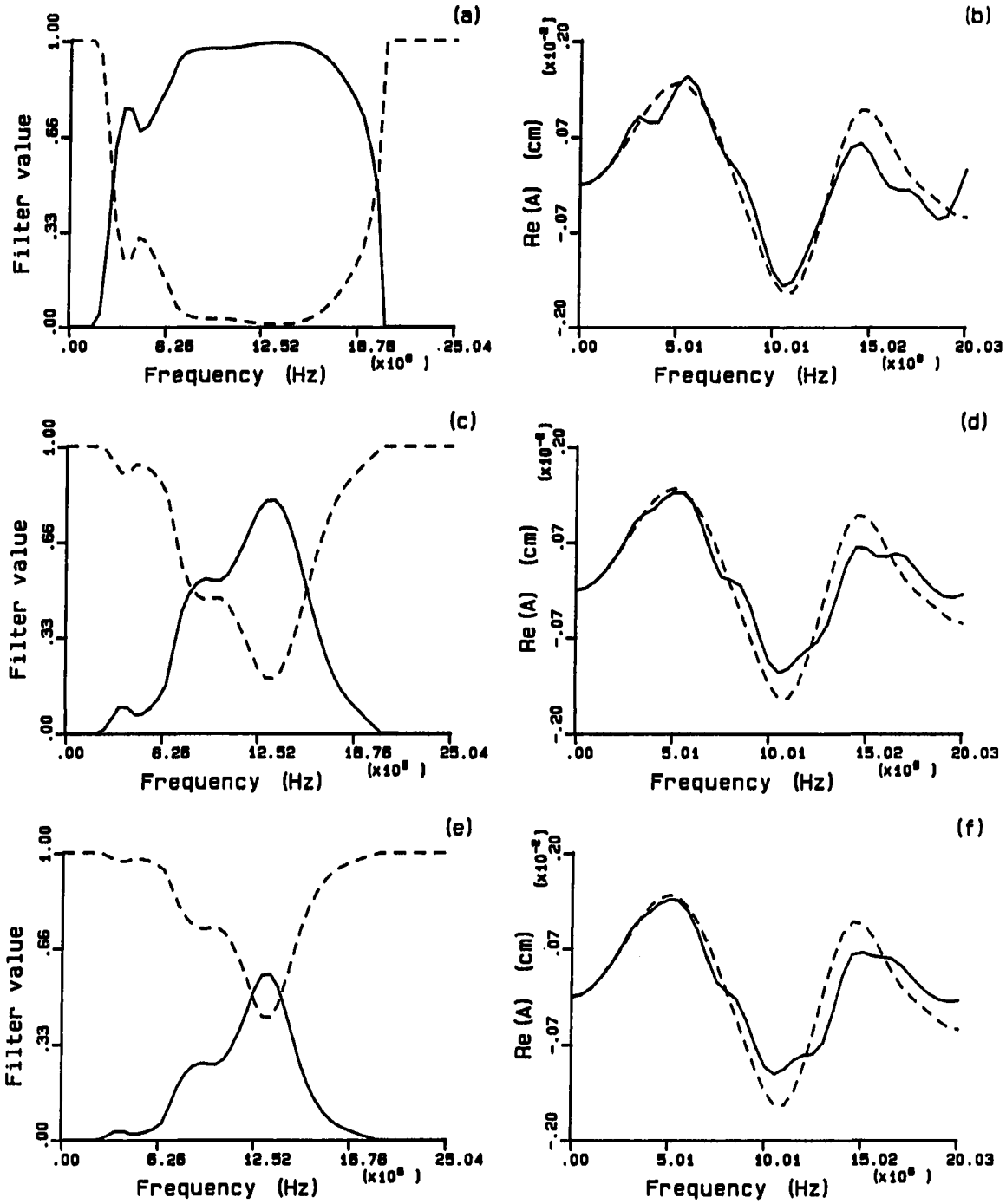

Figure 6.5. Optimal Wiener filter (case 2 acoustic noise-ideal case). a), c), and f) $W_1(\omega)$ (solid) and $W_2(\omega)$ (dashed) for SN_K=20dB, 5dB, and 0dB, respectively; b), d), and f) $Re[\hat{A}(\omega)]$ (dashed) and $Re[A(\omega)]$ (solid) for SN_K=20dB, 5dB, and 0dB, respectively

The strength of the optimal Wiener filter is demonstrated by the lower S/N cases in Fig. 6.5. Notice that as the S/N ratio decreases in going from Figures 6.5.a to 6.5.c to 6.5.d, $W_1(\omega)$ (solid line) decreases and $W_2(\omega)$ (solid line) increases. Thus, as the experimental result becomes more noise-corrupted, the weighting terms deemphasize the experimental result and place more emphasis on $E[A(\omega)]$. The acoustic noise which dominates the flaw signals shown in Figures 6.2.c and 6.2.e and which was passed by the desensitization filter (Figures 6.2.d and 6.2.f) is filtered out by the optimal Wiener filter and replaced with $E[A(\omega)]$. This is demonstrated by Figures 6.5.d and 6.5.f as none of the noise domination evident in the estimates determined by the desensitization filter is evident in the optimal Wiener filter estimates. This represents an ideal application since 1) $E[A(\omega)]$ for a narrow flaw distribution approaches $A(\omega)$ for a flaw with radius equal to m_a (see Chapter V), 2) the flaw size considered (109μm) is approximately m_a (110μm), and 3) the optimal Wiener filter gladly uses $E[A(\omega)]$ as the noise increases since the flaw distribution is narrow. Nevertheless, the contrast between the scattering amplitude estimates shown in Fig. 6.5 and those shown in Fig. 6.2 demonstrates how the optimal Wiener filter, unlike the desensitization filter, attempts to protect $\hat{A}(\omega)$ from acoustic noise domination.

As a further demonstration of the optimal Wiener filter's sensitivity to acoustic noise, consider the case 3 acoustic noise example used in Fig. 6.3 to demonstrate the weakness of the desensitization filter in dealing with low frequency noise. The solid line in Fig. 6.6.a again represents the noise power associated with a single case 3 acoustic noise

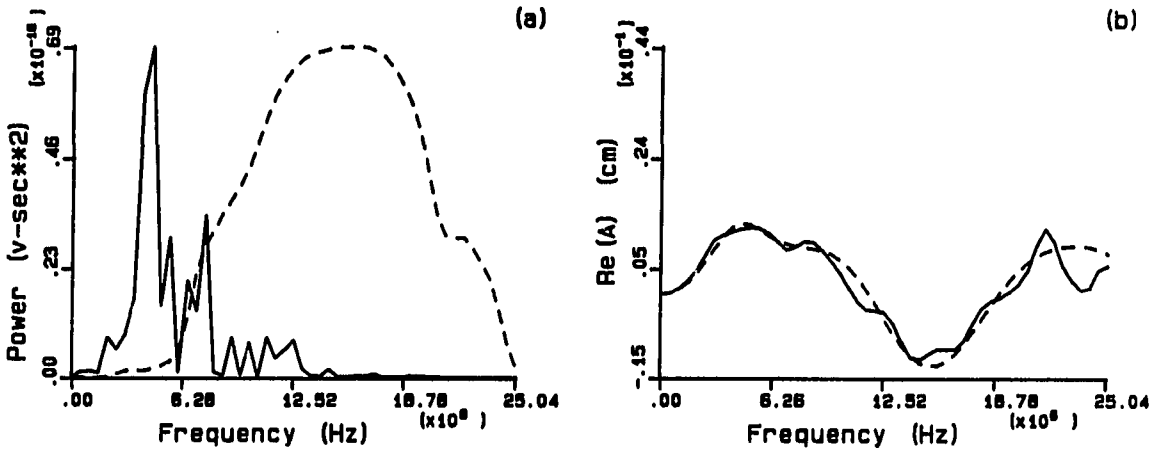

Figure 6.6. Optimal Wiener filter analysis (case 3 acoustic noise). a) noise power spectrum for a single case 3 acoustic noise signal (solid) and $W_1(\omega)$ (dashed); b) calculated (dashed) and estimated (solid) $Re[A(\omega)]$ for a spherical void in aluminum

signal. The dashed line in Fig. 6.6.a is $W_1(\omega)$ for the optimal Wiener filter assuming a lognormal distributions of spherical voids in aluminum with m_a=200μm and σ_a=30μm. The shape of the weighting term demonstrates that the optimal Wiener filter has sensed the acoustic noise dominance at low frequencies and therefore deemphasizes the experimental result in that region. The $Re[\hat{A}(\omega)]$ shown in solid line in Fig. 6.6.b shows very good agreement with the calculated $Re[A(\omega)]$ shown in dashed line. A comparison of the estimate shown in Fig. 6.6.b with that shown in Fig. 6.3.b shows the contrast between the two filters as the optimal Wiener filter has filtered out the noise and effectively extrapolated to zero frequency by utilizing $E[A(\omega)]$ while the desensitization filter is dominated by noise and low frequency extrapolation would be very difficult. Again, this

represents a somewhat ideal case in that the flaw size represented in Fig. 6.6.b is equal to m_a.

Now consider a broader flaw distribution (m_a=110μm, σ_a=30μm). Also, in addition to the 109μm flaw, consider two flaw sizes which vary significantly from m_a. Figures 6.7.a, 6.7.c, and 6.7.e show noise-free measured flaw signals and noise-corrupted (corrupted with case 2 acoustic noise) flaw signals with SN_K=20dB for polystyrene spheres in thermoplastic with radii of 62μm, 109μm, and 156μm, respectively. Figures 6.7.b, 6.7.d, and 6.7.f show $Re[\hat{A}(\omega)]$ determined from these signals in solid line and $Re[A(\omega)]$ in dashed line. First, notice that since SN_K is calculated based on $A(\omega)$ for a flaw with radius equal to m_a, the S/N for a given noise-corrupted flaw signal is a function of the size of the flaw. This behavior is evident in the noise-corrupted flaw signals in the figure as the S/N decreases as the flaw size increases. The noise-corrupted flaw signal shown in Fig. 6.7.c is the same as the one shown in Fig. 6.2.a, and $Re[\hat{A}(\omega)]$ determined by the optimal Wiener filter as shown in Fig. 6.5.a is nearly the same as the estimate shown in Fig. 6.7.d. There is a subtle difference in the two estimates at low frequency due to the difference in the breadth of the flaw distribution associated with the two estimates. For Fig. 6.2, the flaw distribution was quit narrow and $E[A(\omega)]$ was therefore readily utilized at low frequency as the lower limit of the bandwidth was approached. For Fig. 6.7, the distribution is broader, implying that $E[A(\omega)]$ is not necessarily a good estimate; consequently, the optimal Wiener filter relies on the experimental result to lower frequencies and uses $E[A(\omega)]$ only at very low frequency. Since the flaw size for Fig. 6.7.d is 109μm (approximately equal to m_a), $E[A(\omega)]$ is a

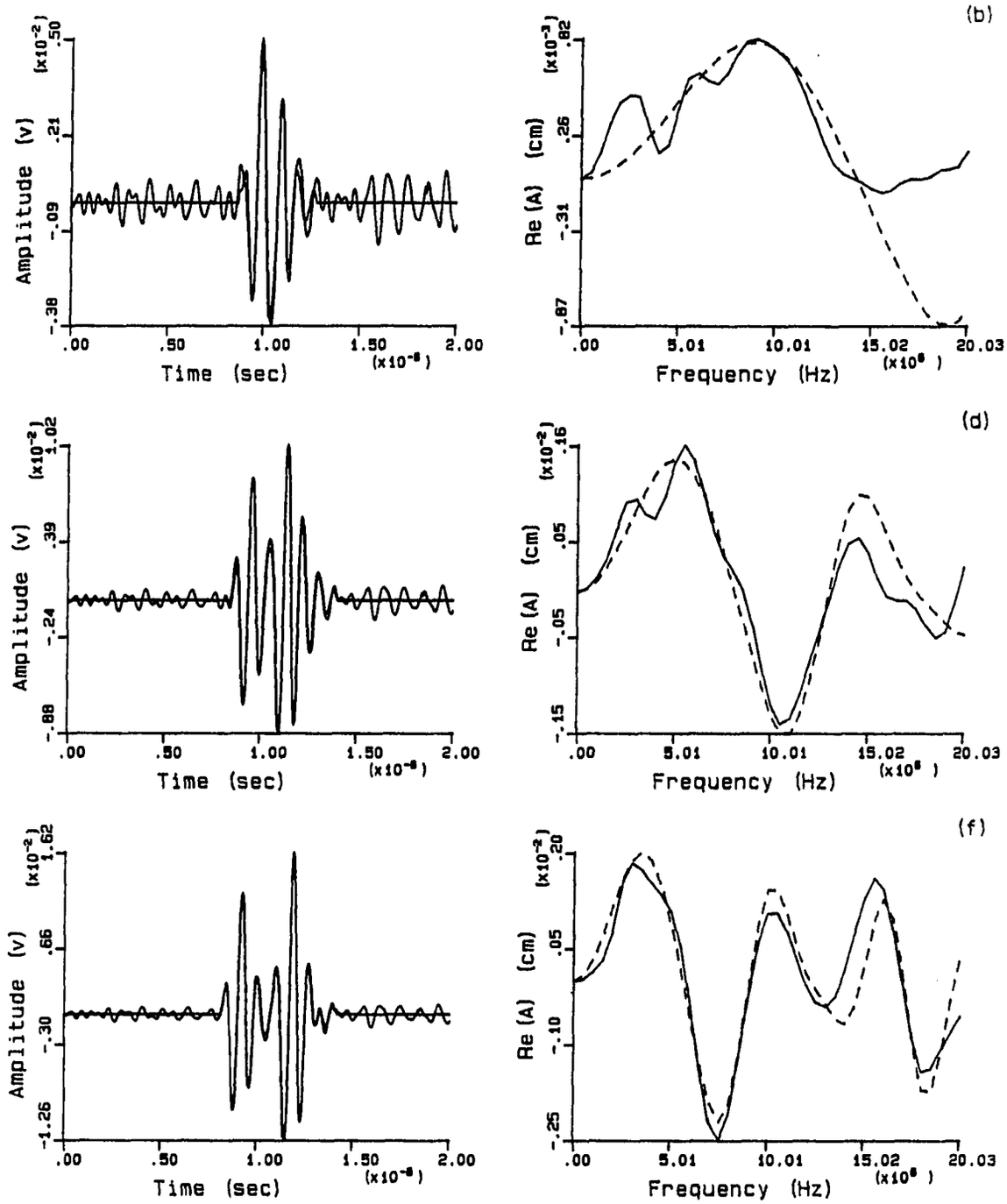

Figure 6.7. Optimal Wiener filter (case 2 acoustic noise-high S/N). a), c), and e) flaw signals for a 109μm radius polystyrene sphere in thermoplastic corrupted with case 2 acoustic noise; b), d), and f) corresponding scattering amplitude estimates

good estimate at very low frequency as demonstrated by the dashed line and the solid line being coincident in this region. For the other two flaw sizes, $E[A(\omega)]$ is not a particularly good estimate at low frequency. This is demonstrated by the figure as the solid line rises much too rapidly for the small flaw (Fig. 6.7.b), and the solid line rises too slowly for the large flaw (Fig. 6.7.f). While this behavior is not ideal, a basic premise of the optimal Wiener filter is that the scattering amplitude distribution is Gaussian so that for the majority of the flaws in a distribution, $E[A(\omega)]$ will be a reasonably good estimate at low frequency. Conversely, there will be a relatively small number of flaws in the distribution such as the ones represented in Figures 6.7.b and 6.7.f. Finally, it was stated that in principle, the second term in the optimal Wiener filter, $W_2(\omega)E[A(\omega)]$, provides for a scattering amplitude estimate outside of the bandwidth. The high frequency portion of the estimate in Fig. 6.7.a shows that while this is true in principle, since $E[A(\omega)]$ approaches zero at high frequencies for most flaw distributions (except for extremely narrow distribution (see Chapter V)), the scattering amplitude estimate is simply forced to zero at high frequency. In other words, other than for very narrow flaw distributions, $E[A(\omega)]$ plays a significant role only at low frequency. At intermediate and high frequency the optimal Wiener filter essentially acts as an optimally constrained deconvolution estimation technique (see Eq. (3.35)).

There is a significant difference between the interaction of the terms which control the weighting terms at low frequency versus high frequency. At low frequency, the scattering amplitude variance is relatively small and $H(\omega)$ goes to zero, both of which indicate that

$E[A(\omega)]$ should be emphasized. Conversely, at high frequency, the scattering amplitude variance is high indicating that $E[A(\omega)]$ is not a good estimate and the experimental result should be emphasized while $H(\omega)$ again goes to zero indicating that the experimental result is not good.

Now consider the same flaw distribution and flaw sizes as those considered in Fig. 6.7 only with a lower S/N (SN_K=5dB). The results for this case are given in Fig. 6.8 Again, notice that the S/N decreases with increasing flaw size from Fig. 6.8.a to Fig. 6.8.e. This figure demonstrates the same type of problem for the optimal Wiener filter as discussed at the end of the previous paragraph. That is, the broad flaw distribution indicates that $E[A(\omega)]$ should be deemphasized while the high noise says that the experimental result should be deemphasized. Thus, there is a complicated frequency dependent interaction between the scattering amplitude variance and the average noise power. In such situations there are no good alternative as demonstrated by the degradation in the scattering amplitude estimates given in Fig. 6.8 relative to those given in Fig. 6.7.

In summary, for high S/N, the performance of the optimal Wiener filter and the desensitization filter is quit similar. As the noise level increases, since the optimal Wiener filter is sensitive to the average noise level, the two filters yield very different estimates. The quality of the estimates determined by the optimal Wiener filter is a function of the interactions between the average noise level and the flaw distribution breadth.

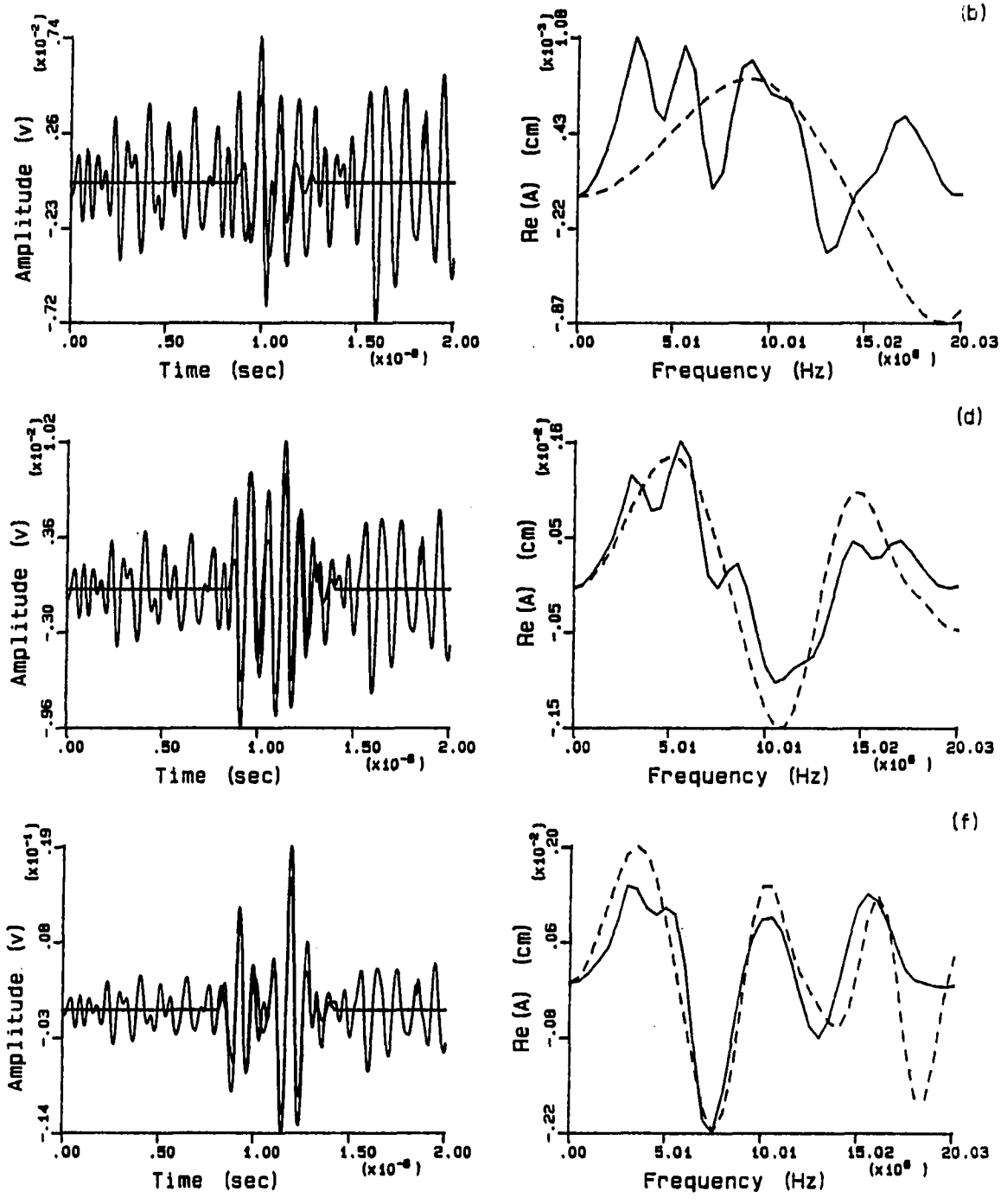

Figure 6.8. Optimal Wiener filter (case 2 acoustic noise-low S/N). a), c), and e) flaw signals for a 109μm radius polystyrene sphere in thermoplastic corrupted with case 2 acoustic noise; b), d), and f) corresponding scattering amplitude estimates

Quantitative analysis

The performance of the optimal Wiener filter will now be considered in terms of quantified error calculations between estimated and calculated scattering amplitudes (Neal and Thompson 1987, Neal and Thompson 1988). Figure 6.9 shows the total error (Eq. (6.8)) versus SN_K for the desensitization filter and optimal Wiener filter, respectively, assuming a lognormal distribution of polystyrene spheres in thermoplastic with m_a=110μm. Values of SN_K ranging from 20dB to -10dB were considered (note that the -10dB case is rather unrealistically noisy in terms of being able to detect a flaw - an example of a 0dB noise-corrupted flaw signals for a 109μm radius flaw is shown in Fig. 6.2.e). Noise-corrupted flaw signals were generated by combining measured flaw signals with case 2 acoustic noise. In Fig. 6.9 and all subsequent graphs, data points associated with the desensitization filter and optimal Wiener filter are represented by open circles and triangles, respectively.

The results given in Fig. 6.9.a are for a narrow flaw distribution with σ_a=10μm. The behavior of the desensitization filter and the optimal Wiener filter was considered qualitatively for this distribution in Figures 6.2 and 6.5, respectively. The results given in Fig. 6.9.a show that at high S/N, the two filters yield similar results. As the noise level increases (i.e., as the S/N decreases), the error for the desensitization filter grows rapidly since the filter simply passes the noise. On the other hand, the optimal Wiener filter places more emphasis on $E[A(\omega)]$ and less emphasis on the experimental result as the noise level increases and the experimental result becomes increasingly noise

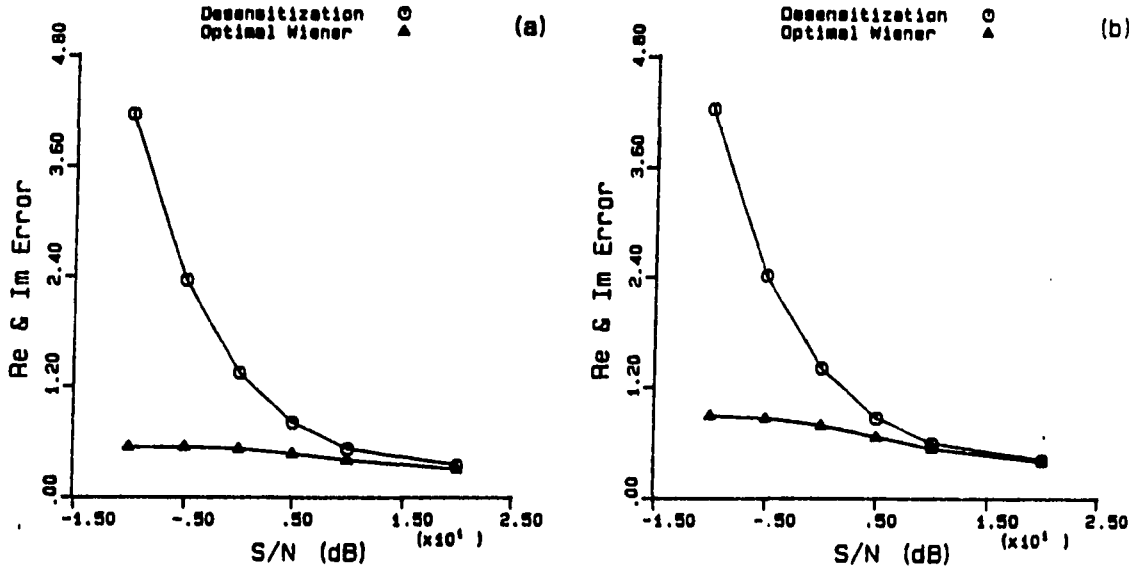

Figure 6.9. Filter results (measured flaw signals). a) m_a=110μm, σ_a=10μm; b) m_a=110μm, σ_a=30μm; (case 2 acoustic noise)

corrupted. Since E[A(ω)] is a good estimate of the scattering amplitude for most flaws out of a narrow flaw distribution, the optimal Wiener filter readily uses E[A(ω)] at low S/N; therefore, the error for the optimal Wiener filter shows very little increase with increased noise level.

Figure 6.9.b shows similar results for a broader distribution with σ_a=30μm. The behavior of the optimal Wiener filter was considered qualitatively for this case in Figures 6.7 and 6.8. The results for the desensitization filter show little dependence on the breadth of the flaw

distribution (Neal and Thompson 1988). This result is as expected since the filter term for the desensitization filter is determined only by the measurement system response and the desensitization term. For the broader distribution, unlike the results for the narrow distribution, the optimal Wiener filter shows an increased error with increased noise level. This behavior can be explained as follows. For a broad distribution, $E[A(\omega)]$ is not a good estimate of the scattering amplitude for many flaws in the distribution (see Figures 6.7 and 6.8); therefore, the optimal Wiener filter is slower to use $E[A(\omega)]$ and effectively passes more of the noise as the experimental result is utilized at higher noise levels. Since $E[A(\omega)]$ is not a good estimate for many flaws in the distribution, when $E[A(\omega)]$ is used, the error between $E[A(\omega)]$ and the true scattering amplitude is greater than the error for a narrow distribution. The results given in Fig 6.9.b show that while poor estimates like the one shown in Fig. 6.8.b will exist, for the majority of the flaws, the optimal Wiener filter yields significantly improved estimates over the desensitization filter.

In Figures 6.10.a and 6.10.b, the results shown in Figures 6.9.a and 6.9.b are reproduced using simulated flaw signals (instead of measured flaw signals) as a base for generating noise-corrupted flaw signals. At high S/N, experimental and modeling errors which are present in the measured flaw signals (see Chapter IV) cause the errors in Figures 6.9.a and 6.9.b to be slightly higher than the errors in Figures 6.10.a and 6.10.b. At low S/N, the effect of these errors is less noticeable. Demonstrating the ability to utilize simulated flaw signals to study estimation techniques is an important result. The use of simulated flaw

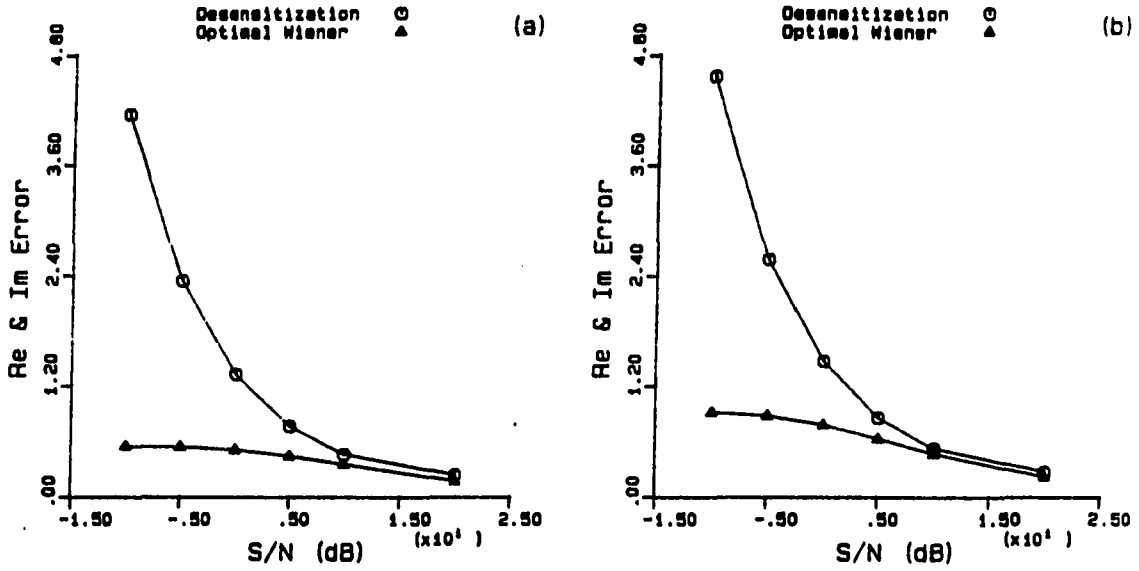

Figure 6.10. Filter results (simulated flaw signals). a) m_a=110μm, σ_a=10μm; b) m_a=110μm, σ_a=30μm; (case 2 acoustic noise)

signals provides the flexibility to consider greater flaw distribution breadths, different distribution means, and different flaw types while still using measured acoustic noise.

The results presented in the previous two figures show an increasing error for the optimal Wiener filter with increasing flaw distribution breadth. This behavior is pursued further in the next three figures by considering four breadths of lognormally distributed spherical voids in stainless steel (Neal and Thompson 1988). Noise-corrupted flaw signals were generated using simulated flaw signals and case 1 acoustic noise. In

each of the next three figures, parts a, b, c, and d correspond to distributions with m_a=250μm and σ_a=5μm, 10μm, 25μm, and 50μm, respectively.

Figure 6.11 shows the total error (Eq. (6.8)) versus SN_K for the four flaw distribution breadths. The observations made relative to this figure are consistent with those made relative to Fig. 6.9 and can be summarized as follows: 1) errors for the desensitization filter are essentially independent of the breadth of the flaw distribution, 2) the optimal Wiener filter and the desensitization filter give similar results at high S/N, and 3) the optimal Wiener filter error increases with increasing flaw distribution breadth. Two additional points are to be noted. First, the effect of the distribution breadth is less at high S/N since the experimental result is emphasized and $E[A(\omega)]$ is deemphasized (note the small changes in the error at 20dB). Conversely, the effect of the distribution breadth is greater at low S/N since $E[A(\omega)]$ is emphasized (Neal and Thompson 1988). Second, results were generated for a distribution with σ_a=75μm; however, the results are not presented here since they are nearly identical to the results for the σ_a=50μm case. This behavior is a consequence of the asymptotic nature of the weighting terms as discussed relative to Figures 6.4.e and 6.4.f. In these figures, it was shown that the weighting terms for the σ_a=50μm and σ_a=75μm cases were nearly the same. Therefore, the corresponding estimation results show little change. As shown by Neal and Thompson (1988), a plot of total error versus distribution breadth shows an increase in error with distribution breadth for narrow distributions; however, as the asymptotic

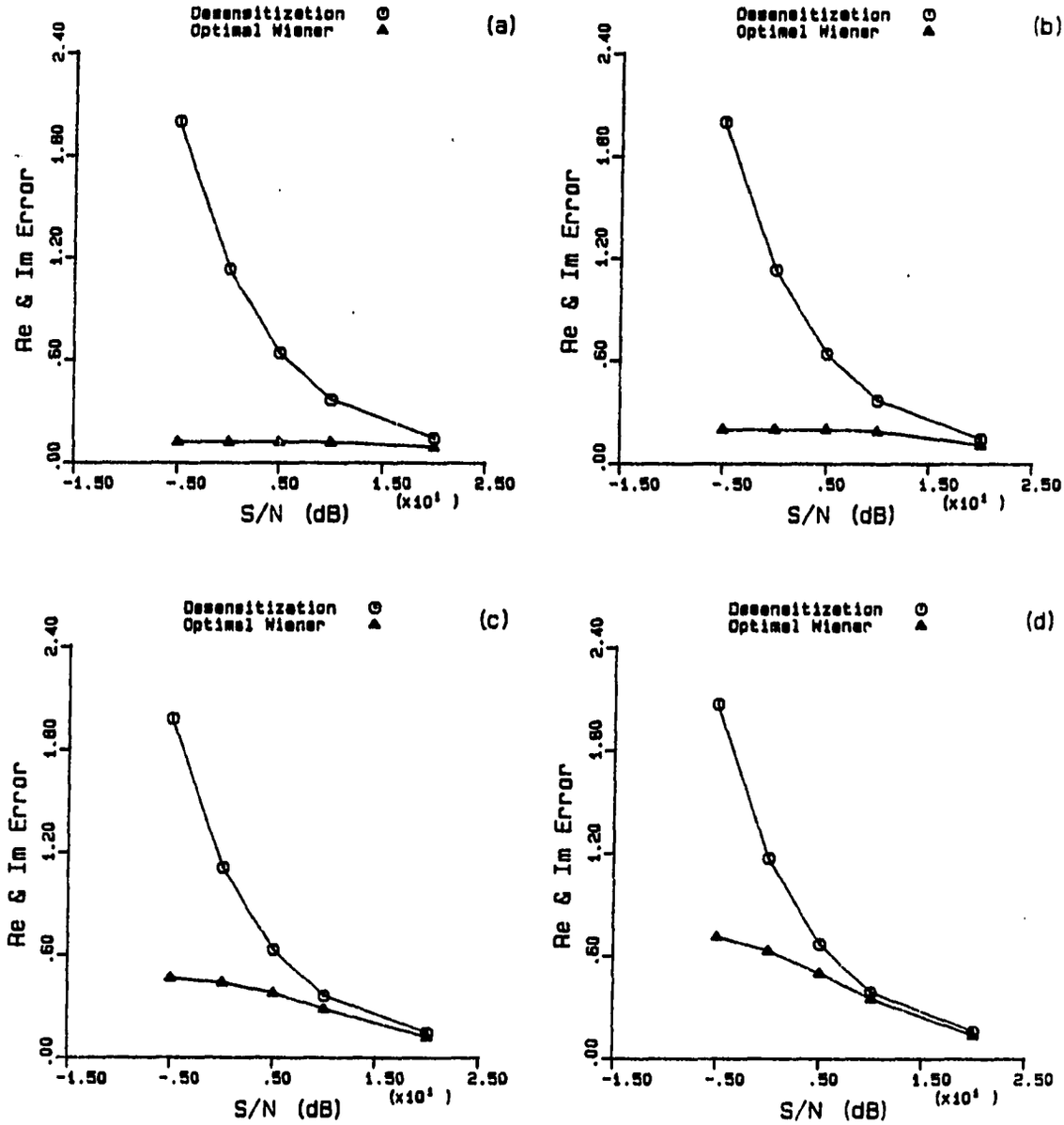

Figure 6.11. Effect of flaw distribution breadth ($\hat{A}(\omega)$ results). a) m_a=250μm, σ_a=5μm; b) m_a=250μm, σ_a=10μm; c) m_a=250μm, σ_a=25μm; d) m_a=250μm, σ_a=50μm; (case 1 acoustic noise)

nature of the weighting terms takes over, the error levels off and effectively becomes independent of the distribution breadth.

The optimal Wiener filter determines scattering amplitude estimates independent of the flaw sizing technique to be used; however, it is tacitly assumed that improved scattering amplitude estimates in a least square-error sense will, in general, lead to improved radius estimates independent of the sizing technique utilized (Neal and Thompson 1987). Nevertheless, it is useful to consider radius estimates determined via the IBA. It was found that at low S/N, estimates determined via the IBA show somewhat erratic behavior. This behavior seems to be particularly pronounced when using the 50% method; therefore, the results presented below are based on radius estimates determined using the area method (see page 84).

Figure 6.12 shows the absolute value of the average percent error, $|e_a|$ (Eq. (6.9)), versus SN_K for the cases considered in Figure 6.10. The assumption that improved scattering amplitude estimates would lead to improved radius estimates is generally followed. An exception exists at high S/N where $|e_a|$ for the desensitization filter is slightly smaller than $|e_a|$ for the optimal Wiener filter even though the scattering amplitude estimates for the optimal Wiener filter were sightly better than those for the desensitization filter. The general conclusions to be drawn from Fig. 6.12 are the same as those enumerated relative to Fig. 6.11. The point to be emphasized is that the errors for the desensitization filter increase dramatically with increased noise level while the errors for the optimal Wiener filter are held in check due to the optimal Wiener filter's sensitivity to noise.

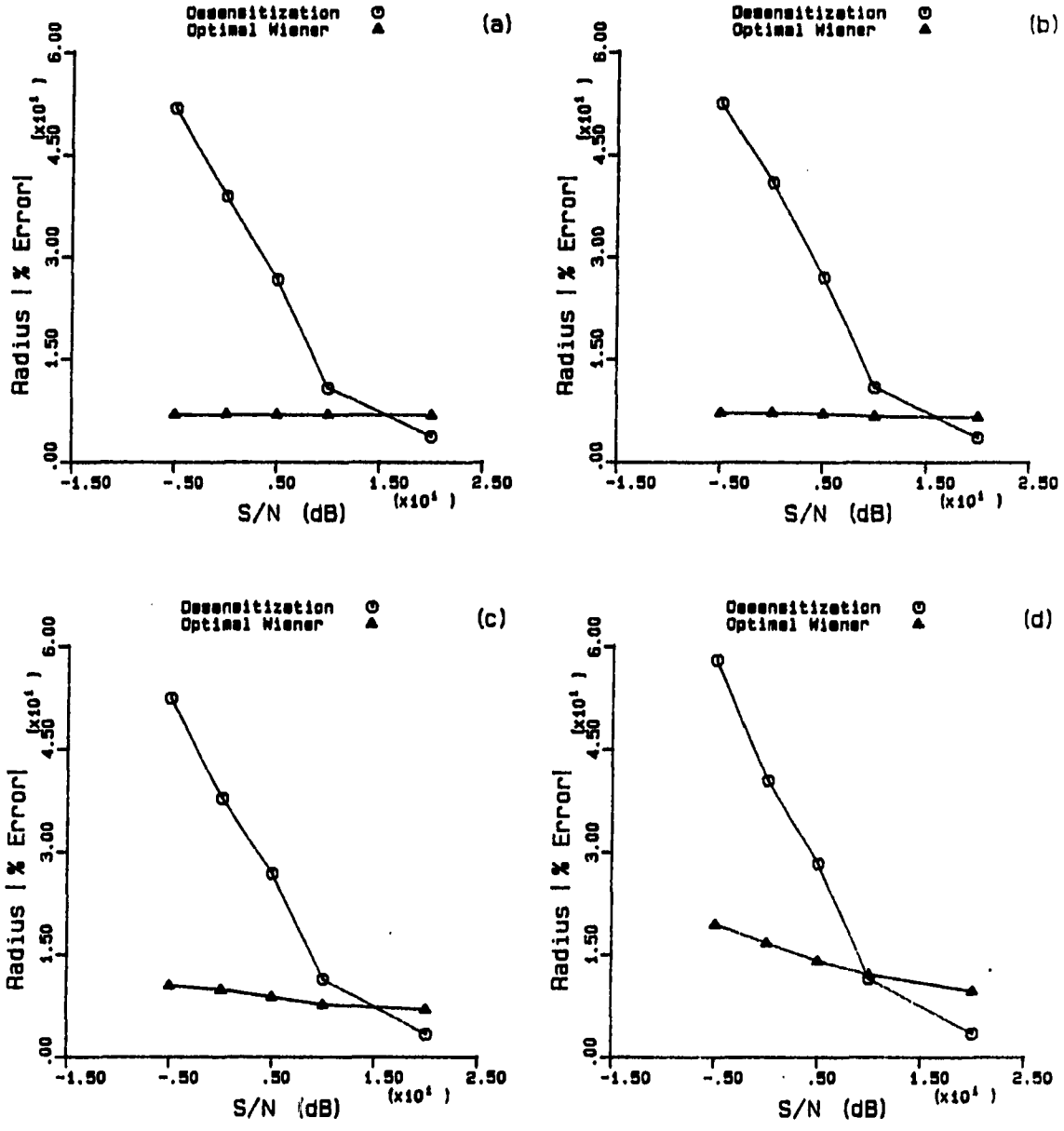

Figure 6.12. Effect of flaw distribution breadth (|radius % error|). a) m_a=250μm, σ_a=5μm; b) m_a=250μm, σ_a=10μm; c) m_a=250μm, σ_a=25μm; d) m_a=250μm, σ_a=50μm; (case 1 acoustic noise)

Figure 6.13 shows the average percent error, e_a (Eq. (6.10)), versus SN_K for the cases considered in Fig. 6.11. Note that e_a must be used with caution since an average percent error of zero could be achieved by greatly oversizing half of the time and greatly undersizing half of the time. At low S/N, the results show the erratic behavior discussed above. The primary observation to be made is again that the sensitivity of the optimal Wiener filter to noise prevents radius estimation errors associated with the optimal Wiener filter from increasing dramatically as the noise level increases. Also, for the conditions considered here (i.e., not to be taken as a general observation), radius estimates associated with the desensitization filter tend to lead to an undersizing of the flaw while estimates associated with the optimal Wiener filter show a slight oversizing behavior (Neal and Thompson 1987).

Since the optimal Wiener filter forces $\hat{A}(\omega)$ to $E[A(\omega)]$ whenever $W_1(\omega)$ goes to zero, it is reasonable to expect radius estimates associated with the optimal Wiener filter to be biased toward the mean flaw size (Neal and Thompson 1988). This behavior would tend to cause and oversizing of small flaw and an undersizing of large flaws. This would in turn lead to a small average percent error on radius estimates as discussed relative to Fig. 6.13. This biasing tendency should by strongest for narrow flaw distributions since $E[A(\omega)]$ is emphasize and since $E[A(\omega)]$ is nearly equal to $A(\omega)$ for a flaw with radius equal to m_a (see Fig. 5.19). For a broader distribution, $E[A(\omega)]$ is significant only at low frequencies, so the biasing tendency may not be apparent. Figure 6.14 demonstrates the biasing tendencies of the optimal Wiener filter for two breadths of lognormally distributed spherical voids in stainless steel. Noise-

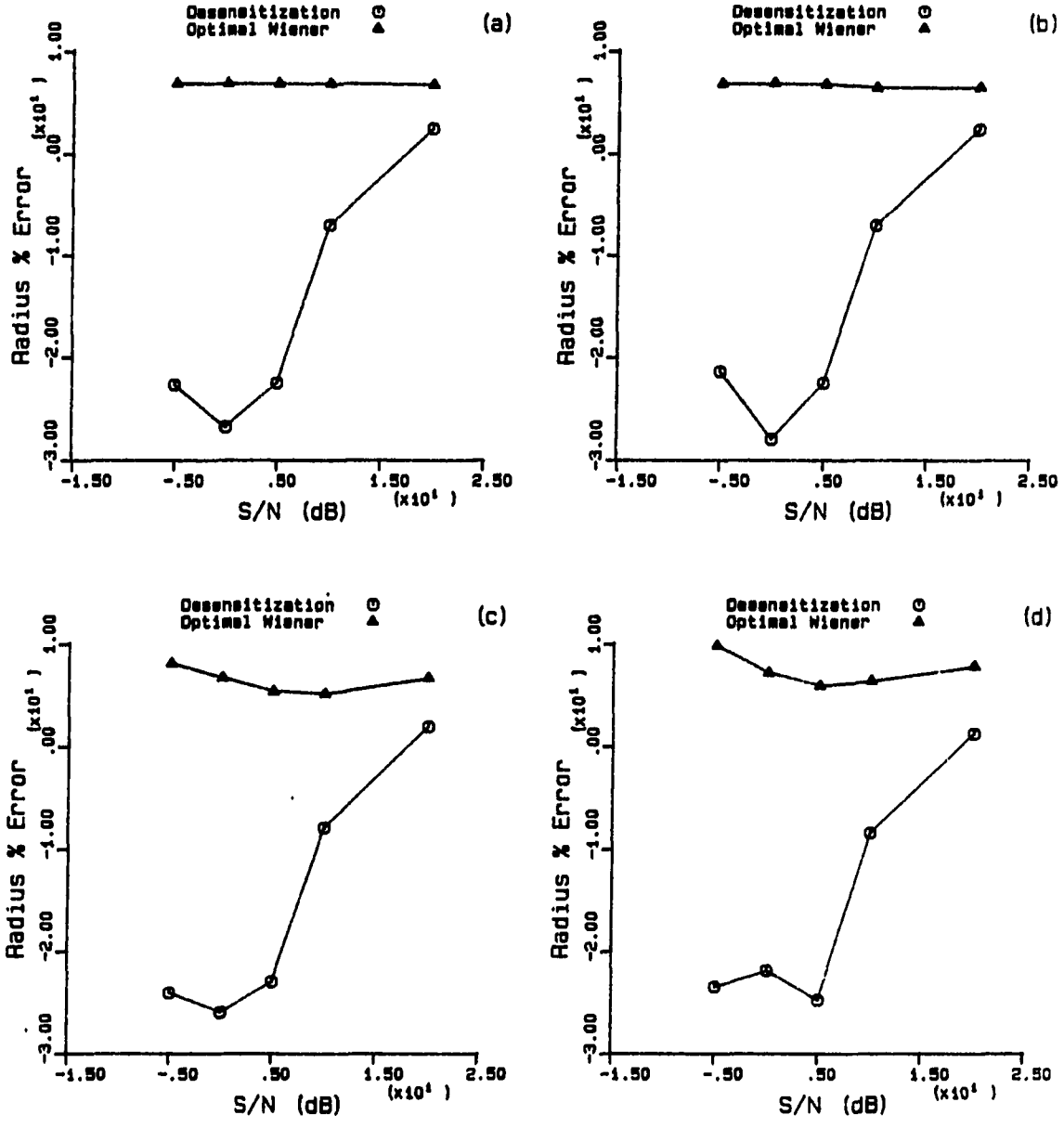

Figure 6.13. Effect of flaw distribution breadth (radius % error). a) m_a=250μm, σ_a=5μm; b) m_a=250μm, σ_a=10μm; c) m_a=250μm, σ_a=25μm; d) m_a=250μm, σ_a=50μm; (case 1 acoustic noise)

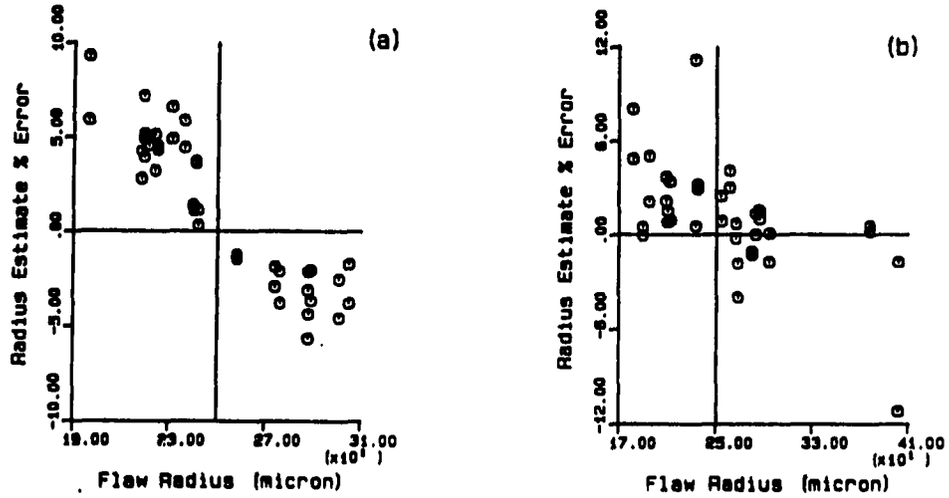

Figure 6.14. Biasing tendency (narrow and broad distributions). a) m_a=250μm, σ_a=15μm; b) m_a=250μm, σ_a=50μm; (case 1 acoustic noise)

corrupted flaw signals were generated using simulated flaw signals and case 1 acoustic noise. The results given in Fig. 6.14.a are for a narrow distribution with m_a=250μm and σ_a=15μm and for a broad distribution with m_a=250μm and σ_a=50μm (Neal and Thompson 1988). As expected, there is no obvious biasing tendency for the broad distribution. For the narrow distribution, the biasing tendency is very evident as all flaws with radii less than the mean are oversized and all flaws with radii greater than the mean are undersized.

In the presence of low frequency noise such as case 3 acoustic noise, the extrapolation step in the desensitization filter algorithm becomes very difficult. This problem was addressed qualitatively relative to Fig. 6.3. As demonstrated in Fig. 6.6, the optimal Wiener filter senses

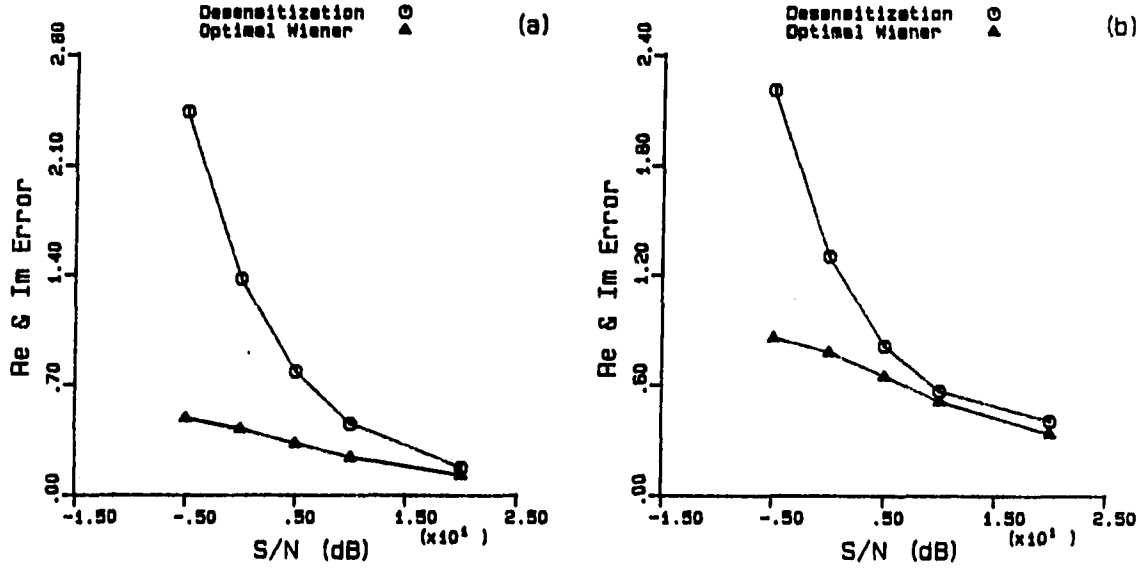

Figure 6.15. Case 3 acoustic noise and noise-like scattering amplitude. a) spherical voids in aluminum (m_a=110μm, σ_a=10μm, case 3 acoustic noise); b) tin-solder spheres in thermoplastic (m_a=110μm, σ_a=30μm, case 2 acoustic noise)

the low frequency noise and provides for a scattering amplitude estimate at low frequency by utilizing $E[A(\omega)]$. Quantitative scattering amplitude estimation results for this case are given in Fig. 6.15.a. Results are shown for the case of a lognormal distribution of spherical voids in aluminum with m_a=200μm and σ_a=30μm. Noise-corrupted flaw signals were generated using simulated flaw signals and case 3 acoustic noise. The results given in Fig. 6.15.a show the same trends as the results shown in Fig. 6.11.c for a similar distribution of spherical voids in stainless

steel. Figures 6.6 and 6.15.a demonstrate that even for the case of low frequency noise, the optimal Wiener filter is successful in determining scattering amplitude estimates to zero frequency through a weighted average of the experimental result and $E[A(\omega)]$.

Scattering amplitude estimation results are shown in Fig. 6.15.b for the case of a lognormal distribution of tin-solder spheres in thermoplastic with m_a=110μm and σ_a=30μm. Noise-corrupted flaw signals were generated using simulated flaw signals and case 2 acoustic noise. The scattering amplitude for a tin-solder sphere in thermoplastic has noise-like characteristics as demonstrated in Fig. 2.3.d. As discussed relative to Fig. 5.20, scattering amplitudes with noise-like features present potential problems for the optimal Wiener filter in that these features may not be present in $E[A(\omega)]$. The results given in Fig. 6.15.b are consistent with the results given in Fig. 6.9.b and demonstrate that in terms of a total error comparison with the desensitization filter, the optimal Wiener filter yields improved estimates for scattering amplitudes with noise-like features.

The robustness of the optimal Wiener filter in the face of errors in estimating the flaw distribution mean and variance are now considered (Neal and Thompson 1988). These errors impact estimation results through their influence on the weighting terms via $\bar{\sigma}_A^2(\omega)$ and through their influence on $\bar{m}_A(\omega)$ (see Equations (6.6) and (6.7) and Fig. 5.19). Consider the effect of errors in estimating the flaw distribution breadth. Assume that a lognormal distribution of spherical voids in stainless steel is correctly characterized with m_a=250μm and σ_a=25μm. Scattering amplitude estimates were determined from noise-corrupted flaw signals

which were generated out of this distribution using simulated flaw signals and case 1 acoustic noise. The optimal Wiener filter was set with $\bar{\sigma}_A^2(\omega)$ and $\bar{m}_A(\omega)$ calculated based on the correct m_a of 250μm and various incorrectly estimated σ_a's ranging from 5μm to 45μm. The scattering amplitude estimation results shown in Figures 6.16.a and 6.16.b were determined with σ_a=5μm and σ_a=15μm, respectively. The results in Figures 6.16.c and 6.16.d were determined with σ_a=35μm and σ_a=45μm, respectively. Estimation results with the optimal Wiener filter set based on the correct parameters were given in Fig. 6.11.c. The general conclusion to be drawn from Fig. 6.16 is that the optimal Wiener filter is relatively insensitive to errors in estimating the flaw distribution breadth. At low S/N, errors due to noise corruption dominate, and any addition errors due to errors in estimating the flaw distribution breadth are negligible. Assuming the distribution is broader than the actual distribution (Figures 6.16.c and 6.16.d) yields only slight increases in estimation errors. This behavior can be explained: 1) due to the asymptotic nature of the weighting terms; and 2) since, for a broad distribution, $\bar{m}_A(\omega)$ is used primarily for low frequency extrapolation, and, at low frequency, $\bar{m}_A(\omega)$ is relatively insensitive to errors in characterization of the flaw distribution. The greatest effect on estimation errors is observed when the assumed flaw distribution breadth is much smaller than actual distribution breadth (Fig. 6.16.a). This behavior is reasonable since: 1) the optimal Wiener filter emphasizes $\bar{m}_A(\omega)$ for a narrow distribution; and 2) the distribution is broader than assumed so that $\bar{m}_A(\omega)$ is not a good estimate of the scattering amplitude for many of the flaws in the distribution.

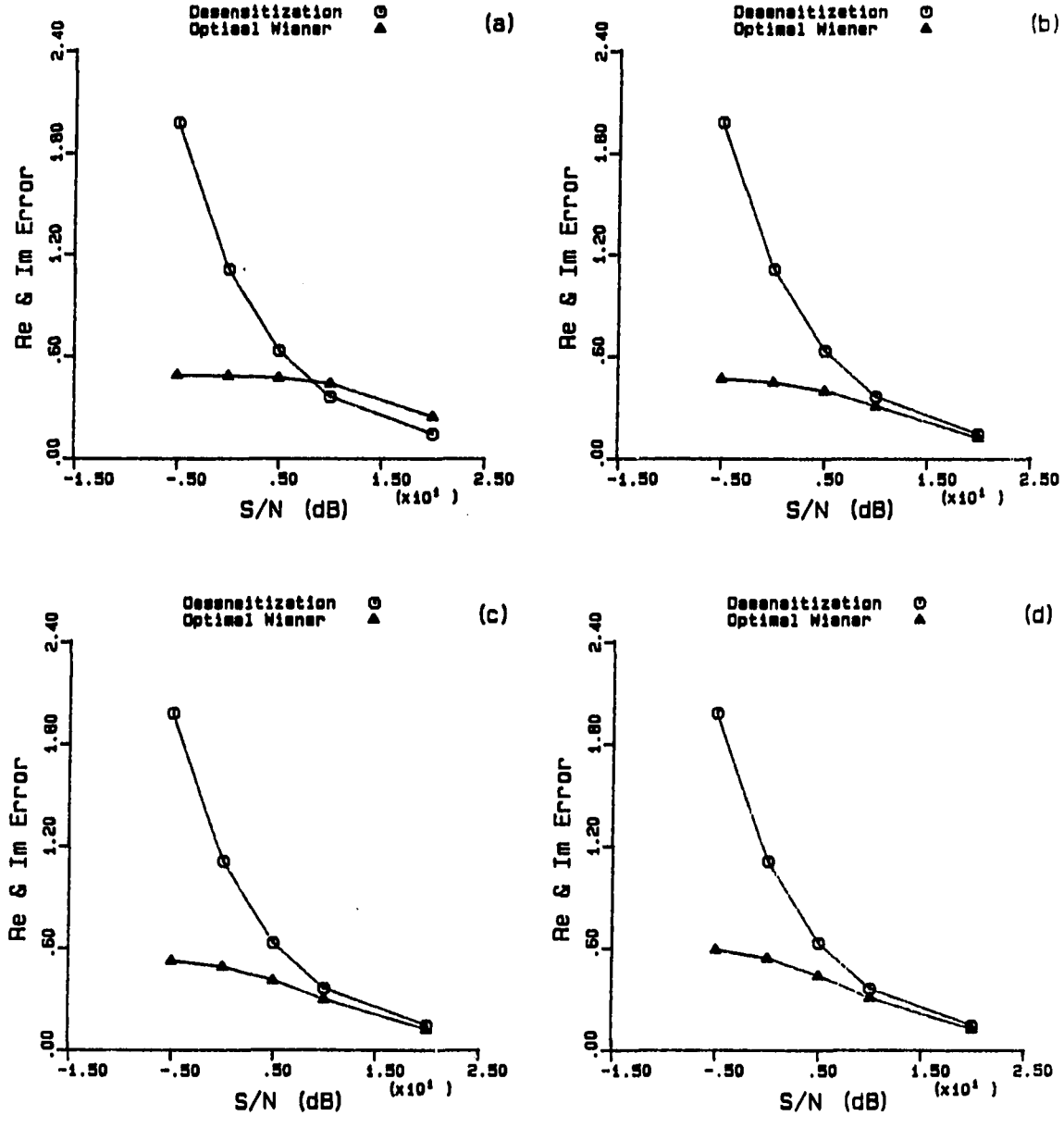

Figure 6.16. Flaw distribution characterization errors (variance).
a) σ_a=5μm; b) σ_a=15μm; c) σ_a=35μm; d) σ_a=45μm;
(actual distribution parameters: m_a=250μm, σ_a=25μm)

While errors in estimating the flaw distribution breadth indirectly effect $\bar{m}_A(\omega)$ (see Fig. 5.19), errors in estimating the flaw distribution mean have a direct effect on $\bar{m}_A(\omega)$. Since $\bar{m}_A(\omega)$ makes up a portion each scattering amplitude estimate, errors in estimating m_a have a greater impact on estimation errors than the impact due to errors in estimating σ_a (Neal and Thompson 1988). Consider the effect of errors in estimating m_a on scattering amplitude estimates for the distribution on which the results presented in Fig. 6.16 where based. The optimal Wiener filter was set with $\bar{\sigma}_A^2(\omega)$ and $\bar{m}_A(\omega)$ calculated based on the correct σ_a of 25μm and various incorrectly estimated m_a's ranging from 150μm to 350μm. The results in Figures 6.17.a and 6.17.b were determined with m_a=150μm and m_a=200μm, respectively. The results in Figures 6.17.c and 6.17.d were determined with m_a=300μm and m_a=350μm, respectively. The impact of errors in estimating m_a is seen at both high S/N and low S/N. At high S/N, errors due to noise corruption are small; therefore, while $\bar{m}_A(\omega)$ is deemphasized at high S/N, increased errors due to errors in $\bar{m}_A(\omega)$ are noticeable. At low S/N, since $\bar{m}_A(\omega)$ is emphasized, errors in $\bar{m}_A(\omega)$ are strongly reflected in the scattering amplitude estimates.

When $\bar{m}_A(\omega)$ is emphasized, such as at low S/N in Fig. 6.17, the optimal Wiener filter is very sensitive to errors in characterization of the flaw distribution mean. The effects of mean estimation errors for a narrow flaw distribution with m_a=250μm and σ_a=5μm are shown in Fig. 6.18. The results given in Figures 6.18.a-d where determined based on m_a=150μm, 200μm, 300μm, and 350μm, respectively. The impact of mean estimation errors is much greater for the narrow distribution than for the broader distribution (Fig. 6.17). For the narrow distribution, the effect of mean

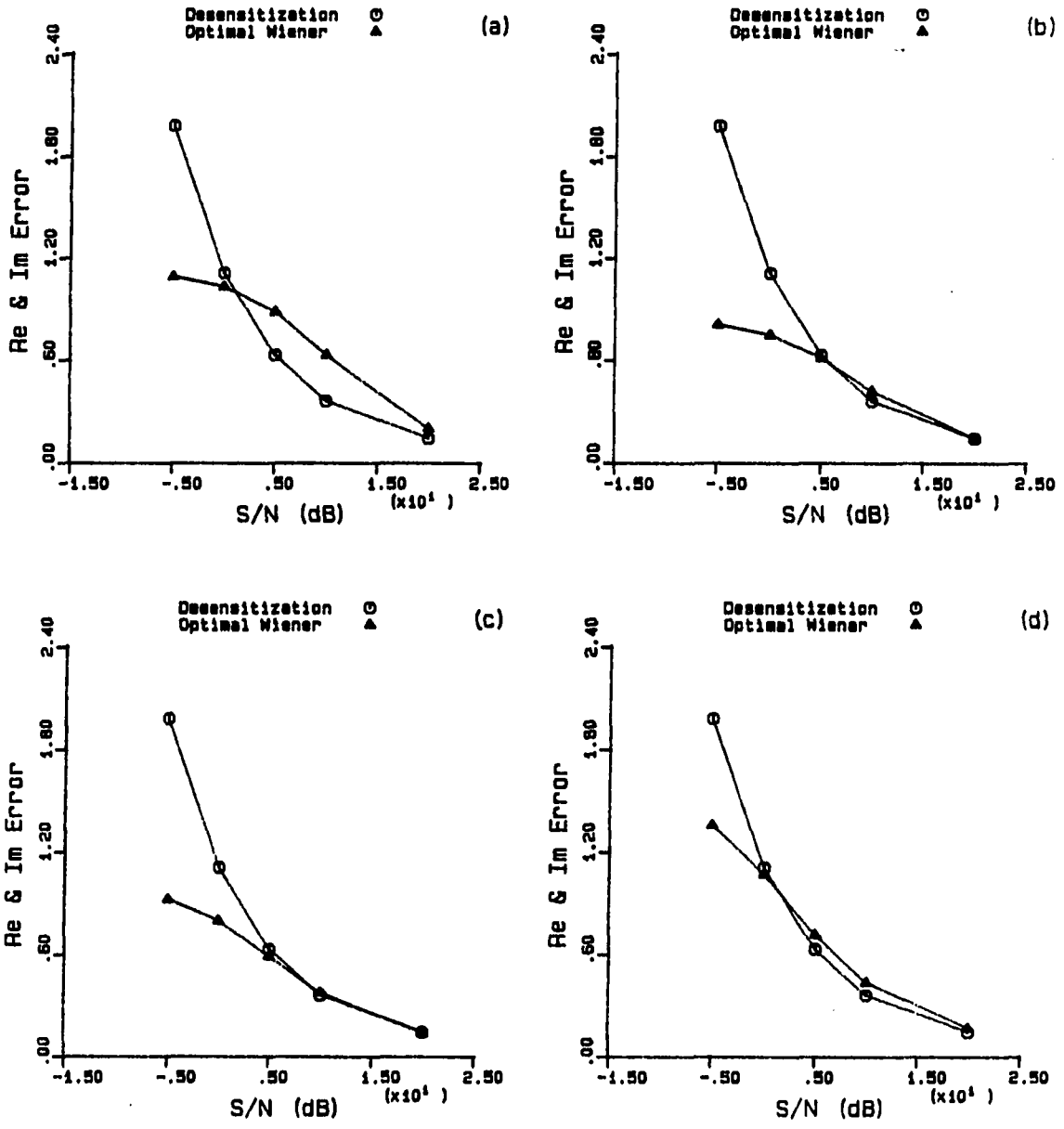

Figure 6.17. Flaw distribution characterization errors (mean/broad). a) m_a=150μm; b) m_a=200μm; c) m_a=300μm; d) m_a=350μm; (actual distribution parameters: m_a=250μm, σ_a=25μm)

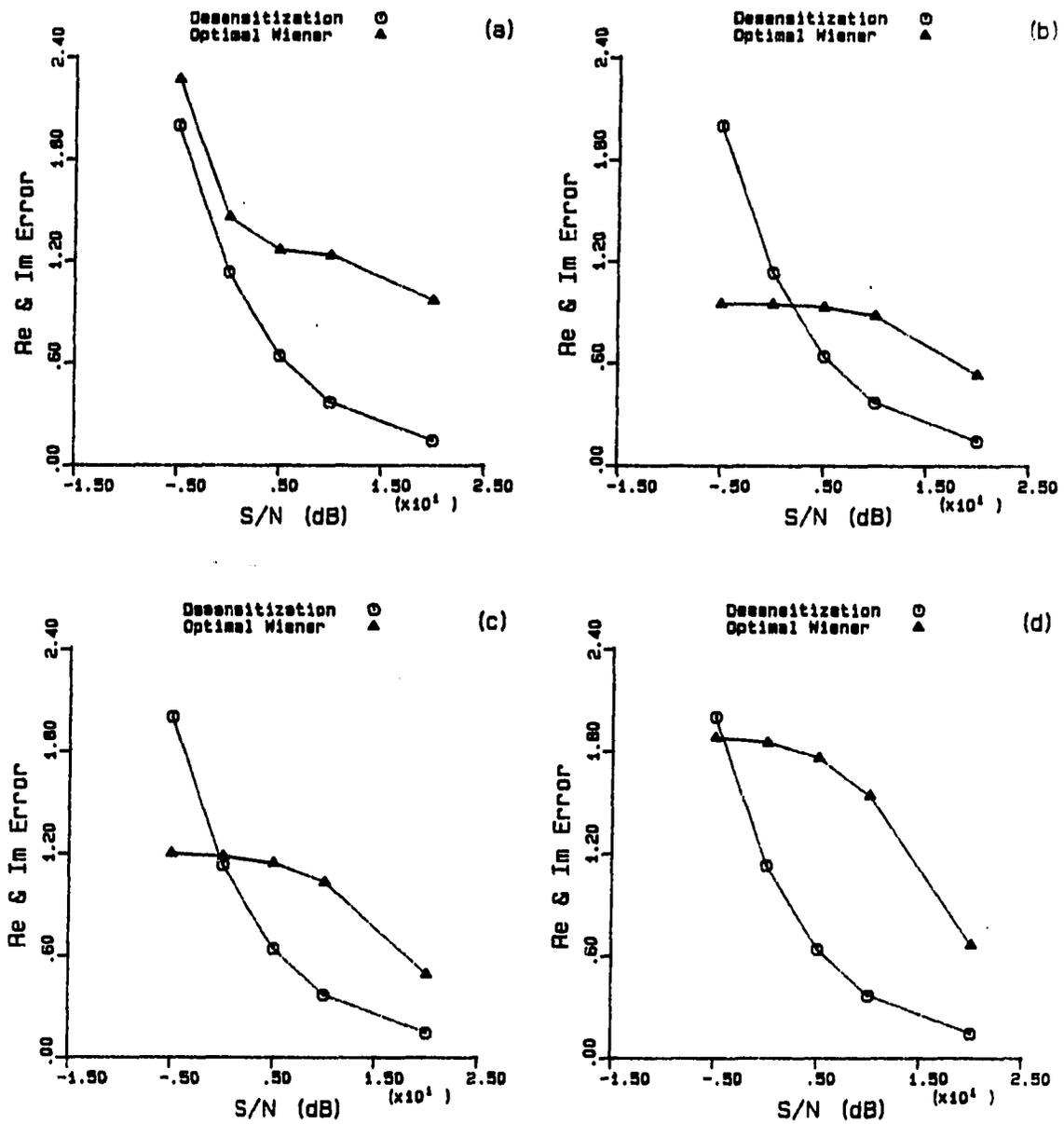

Figure 6.18. Flaw distribution characterization errors (mean/narrow). a) m_a=150μm; b) m_a=200μm; c) m_a=300μm; d) m_a=350μm; (actual distribution parameters: m_a=250μm, σ_a=5μm)

estimation errors is great since: 1) $\bar{m}_A(\omega)$ is emphasized, and 2) $\bar{m}_A(\omega)$ is incorrect since it is based on the incorrect flaw distribution mean. For the broader distribution, the effect of mean estimation errors is less since: 1) $\bar{m}_A(\omega)$ is used primarily for low frequency extrapolation, and 2) errors in $\bar{m}_A(\omega)$ (due to errors in m_a) are minimal at low frequency.

CHAPTER VII. SUMMARY AND DISCUSSION

Evaluation of the optimal Wiener filter has been presented in four stages. Derivation of the filter for the non-zero mean scattering amplitude case yielded a form of the optimal Wiener filter not previously applied to the scattering amplitude estimation problem. This form shows that the filter determines an optimal estimate as the weighted average of the information derived from measurement of the scattered acoustic field and prior information about the flaw distribution.

In order to study the filter under a variety of conditions, a novel approach was adopted where noise-corrupted flaw signals were created by combining essentially noise-free measured flaw signals with measured acoustic noise signals. Procedures involved in the acquisition and processing of flaw signals and noise signals were given in Chapter IV.

Noise and scattering amplitude were analyzed as random variables with emphasis on the evaluation of the assumptions made in deriving the filter. Based on measured noise signals, electronic noise and three types of acoustic noise were shown to be reasonably Gaussian and uncorrelated with zero mean. Both analytical and numerical procedures for relating scattering amplitude distributions to flaw distributions were established. Scattering amplitude was identified as a deterministic random variable, and examples of scattering amplitude means and variances were given. For a distribution of volumetric scatterers with fixed material properties, it was shown that scattering amplitude does not have zero mean at all frequencies and that it is neither uncorrelated nor reasonably Gaussian at all frequencies.

Procedures were given for creating a family of noise-corrupted flaw signals using either measured or simulated flaw signals along with measured noise signals. It was shown that filtering results based on noise-corrupted flaw signals which were created using measured flaw signals and measured noise could be reproduced by using simulated flaw signals and measured noise. The performance of the optimal Wiener filter in determining scattering amplitude estimates from the noise-corrupted flaw signals was evaluated and compared to the performance of the desensitization filter. The optimal Wiener filter and the desensitization filter were shown to yield similar results at high S/N; however, at low S/N the optimal Wiener filter yielded significantly improved results by filtering out the noise and by using prior flaw information. The optimal Wiener filter was shown to yield improved result for both high frequency and low frequency acoustic noise and for both narrow and broad flaw distributions. The tendency of the optimal Wiener filter to oversize small flaw and undersize large flaws was considered. It was shown that this tendency is greatest for narrow distributions and less pronounced for broader distributions. The effect of errors in characterization of the flaw distribution was evaluated. It was found that for narrow flaw distributions, scattering amplitude estimation errors are initially small; however, the results are relatively sensitive to errors in characterization of the flaw distribution. For a broad distribution, estimation errors are initially higher; however, the results are relatively insensitive to errors in characterization of the flaw distribution.

The practical utility of model based estimation techniques such as the optimal Wiener filter will be limited by the availability of flaw distribution information. In general, economic considerations will prohibit establishing an appropriate flaw data base via destructive evaluation of components already in service. However, with increased emphasis on NDE considerations in design and manufacturing, the potential exists for establishing the required flaw information based on knowledge of a particular manufacturing process and destructive evaluation at the development stage (Elsley 1981, Perry 1985). A certain degree of leverage exists in terms of establishing flaw data bases in that prior flaw information is useful not only in flaw signature estimation as demonstrated by this work, but also in the detection, classification, and characterization of flaws.

The ability to measure and characterize noise along with the lack of availability of flaw data suggests that scattering amplitude estimation techniques which incorporate prior noise information but which do not require prior flaw information (Murakami et al. 1978, Furgason et al. 1978) may be useful. Regardless of whether an estimation technique is used which requires both prior noise and flaw information or prior noise information alone, further work is needed in the noise characterization area. The approach taken in this work has been very basic in the sense that 1) $H(\omega)$ was the same for each flaw in a given ensemble, 2) all measurements were made in a pulse-echo mode at normal incidence, and 3) the implications of the acoustic noise measurement procedures is that backscattered noise must be measured adjacent to each flaw to be characterized. Perhaps ideally, information gathered via preliminary flaw

interrogation experiments would be used to optimally select the transducers, instrument settings, water path lengths, and interrogation angles to be employed in measuring flaw signals (Elsley et al. 1980, Davidson and DeFacio 1981, Addison et al. 1982, Wormley et al. 1986, Hsu et al. 1987). In such cases, even for a given type of host material with statistically uniform grain structure, average acoustic noise characteristics will be different for each flaw signal. In particular, both $H_a(\omega)$ and $A_a(\omega)$ will vary with flaw depth, interrogation angle, and mode (pulse-echo versus pitch-catch), and $H_a(\omega)$ will vary with measurement system components and settings. Provided that a large number of scattering sites are involved, it is anticipated that acoustic noise measured at any angle, in either mode, and at any depth will be uncorrelated and reasonably Gaussian (due to the central limit theorem argument given in Chapter V). The problem is that after the flaw interrogation conditions have been established, the average noise power spectrum must be estimated. In practice, due to inspection time constraints or limited access to the flawed component, for example, it may not be feasible to establish the average noise power based on a family of noise signals measured adjacent to each flaw to be characterized. In principle, $H_a(\omega)$ and an estimate of the variance (the average power) of $A_a(\omega)$ could be established via a model based approach where the parameters in the model would be determined based on the measurement conditions and perhaps a single measurement taken adjacent to the flaw to be characterized. Some work has been done in this area (Fertig and Richardson 1983); however, at this point, neither $H_a(\omega)$ nor $A_a(\omega)$ is understood well to make such an approach feasible. Further work in this

area is underway relative to modeling noise for probability of detection studies (Gray 1988).

Other concerns exist relative to the validity of acoustic noise characterization. In certain cases, the presence of a flaw may change the average grain size in the region surrounding the flaw (Perry 1985, Rehbein et al. 1987). In such cases, backscattered noise measured at positions adjacent to the flaw will not be representative of that noise which corrupts the flaw signal. In addition, during the flaw interrogation experiment, there are obviously no scattering sites (e.g., grains or pores) in the position of the flaw. Therefore, it is assumed that a large enough number of scattering sites are involved so that the backscattered noise from a particular region, such as the region occupied by the flaw, is not significant relative to the overall scattering. Since, in general, the interrogating beam diameter will be much greater than the flaw diameter, the strength off-axis scattering contributions make this a reasonable assumption. However, the bounds on such an assumption are not clear and it is not obvious how the they could be reliably set.

REFERENCES

Achenbach, J. D., and A. K. Gautesen. 1977. Geometrical theory of diffraction for 3-D elastodynamics. J. Acoust. Soc. Amer. 61(2):413-421.

Achenbach, J. D., L. Adler, D. K. Lewis, and H. McMaken. 1979. Diffraction of elastic waves by penny-shaped cracks in metals, theory and experiment. J. Acoust. Soc. Amer. 66(6):1848-1856.

Achenbach, J. D., A. K. Gautesen, and H. McMaken. 1982. Ray methods for waves in elastic solids. Pitman Advances Publishing Co., Boston.

Addison, R. C., R. K. Elsley, and J. F. Martin. 1982. Test bed for quantitative NDE - inversion results. p. 251-261. In D. O. Thompson and D. E. Chimenti (ed.) Review of progress in quantitative NDE. Vol. 1. Plenum Press, New York.

Adler, L., and J. D. Achenbach. 1980. Elastic wave diffraction by elliptical cracks: theory and experiment. J. Nondestr. Eval. 1(2):87-99.

Annis, C. G., J. S. Cargill, J. A. Harris, Jr., and M. C. Vanwanderham. 1981. Engine component retirement-for-cause: a nondestructive evaluation (NDE) and fracture mechanics based maintenance concept. p. 53-63. In O. Buck and S. M. Wolf (ed.) Nondestructive evaluation: microstructural characterization and reliability strategies symposium proceedings. Pittsburgh, Pennsylvania, October 5-9, 1980. The Metallurgical Society of AIME, Warrendale, Pennsylvania.

Assefi, T. 1979. Stochastic processes and estimation theory with applications. Wiley, New York.

Beauchamp, K. G., and C. K. Yuen. 1979. Digital methods for signal analysis. George Allen and Unwin, London.

Bendat, J. S., and A. G. Persal. 1971. Random data; analysis and measurement procedures. Wiley, New York.

Beyer, R. T., and S. V. Letcher. 1969. Physical ultrasonics. Academic Press, New York.

Bhagat, P. K., D. E. Chimenti, T. J. Moran, and K. D. Shimmin. 1984. Effects of deconvolution procedures on size estimates in the Born inversion algorithm. p. 395-403. In D. O. Thompson and D. E. Chimenti (ed.) Review of progress in quantitative NDE. Vol. 3. Plenum Press, New York.

Bhagat, P. K., and K. D. Shimmin. 1984. Homomorphic processing in ultrasonic NDE. p. 351-358. In D. O. Thompson and D. E. Chimenti (ed.) Review of progress in quantitative NDE. Vol. 3. Plenum Press, New York.

Bond, L. J., C. Chaloner, S. J. Wormley, S. P. Neal, and J. H. Rose. 1987. Recent advances in Born inversion (weak scatterers). p. 437-444. In D. O. Thompson and D. E. Chimenti (ed.) Review of progress in quantitative NDE. Vol. 7A. Plenum Press, New York.

Bond, L. J., J. H. Rose, S. J. Wormley, and S. P. Neal. 1988. Advances in Born inversion. p. 23-38. In C. H. Chen (ed.) Signal processing and pattern recognition in nondestructive evaluation of materials. Vol. F44. Springer-Verlag, Berlin.

Bracewell, R. 1965. The Fourier transform and its applications. McGraw-Hill, New York.

Brown, R. G. 1983. Introduction to random signal analysis and Kalman filtering. Wiley, New York.

Chaloner, C., and L. J. Bond. 1987. Investigation of the 1-D inverse Born technique. IEE Proceedings 134, Pt. A:257-265.

Chernoff, H., and L. E. Moses. 1959. Elementary decision theory. Wiley, New York.

Chou, C. H., B. T. Khuri-Yakub, K. Liang, and G. S. Kino. 1980. High-frequency bulk wave measurments of structural ceramics. Proceedings of the DARPA/AF Review of progress in quantitative NDE. Technical Report ARWAL-TR-80-4078 (Air Force Wright Aeronautical Laboratories, Dayton, OH, 1980) 663-669.

Clark, G. A., J. D. Brase, B. D. Cook, and D. M. Tilly. 1985a. A- and B-scan resolution enhancement using system identification techniques. Presented at Review of progress in quantitative NDE, June 23-28, 1985 in Williamsburg, VA.

Clark, G. A., D. M. Tilly, B. D. Cook, and J. D. Brase. 1985b. Bandlimited signal extrapolation for A- and B- scan resolution enhancement. Presented at Review of progress in quantitative NDE, June 23-28, 1985 in Williamsburg, VA.

Clark, G. A., D. M. Tilly, and B. D. Cook. 1986. Ultrasonic signal/image restoration for quantitative NDE. NDT International 19(3):169-176.

Cohen-Tenoudji, F., Y. Pralus, A. Lambert, G. Quentin, and B. R. Tittmann. 1984. Polynomial extrapolation toward low frequencies of the spectrum of gated ultrasonic echoes for deconvolution: application to defects in solids. p. 359-371. In D. O. Thompson and D. E. Chimenti (ed.) Review of progress in quantitative NDE. Vol. 3A. Plenum Press, New York.

Cooper, T. D., and D. M. Forney. 1981. Increased inspection requirements for critical Air Force engine components. Presented at the 1981 Air Transport Association Nondestructive Testing Forum, Phoenix, Arizona.

Davidson, M. E., and B. DeFacio. 1981. Simulation of a multitransducer ultrasonic dome device for nondestructive evaluation. p. 1241-1252 In W. G. Vogt and M. H. Mickle (ed.) Proceedings of the 12th Annual Pittsburgh conference on modeling and simulation. Vol. 12. No. 4. Instrument Society of America, Research Triangle Park, North Carolina.

Davies, A. R. 1982. On the maximum likelihood regularization of Fredholm convolution equations of the first kind. p. 95-105. In C. T. H. Baker and G. F. Miller (ed.) Treatment of Integral Equations by Numerical Methods. Academic Press, New York.

Domany, E., J. A. Krumhansl, and S. Teitel. 1978. Quasistatic approximation to the scattering of elastic waves by a circular crack. J. Appl. Phys. 49(5):2599-2604.

Elsley, R. K., and R. C. Addison. 1981. Dependence of the accuracy of the Born inversion on noise and bandwidth. Proceedings of the DARPA/AF Review of progress in quantitative NDE. Technical Report ARWAL-TR-81-4080 (Air Force Wright Aeronautical Laboratories, Dayton, OH, 1981) 389-395.

Elsley, R. K., J. M. Richardson, and R. C. Addison. 1980. Optimum measurement of broadband ultrasonic data. p. 916-921. In B. R. McAvoy (ed.) Ultrasonic symposium proceedings. Vol. 2. IEEE, New York.

Elsley, R. K., L. A. Ahlberg, and J. M. Richardson. 1981. Low frequency characterization of flaws in ceramics. Proceedings of the DARPA/AF Review of progress in quantitative NDE. Technical Report ARWAL-TR-81-4080 (Air Force Wright Aeronautical Laboratories, Dayton, OH, 1981) 151-164.

Elsley, R. K., K. W. Fertig, J. M. Richardson, and R. S. Linebarger. 1984. Statistical flaw detection: Application to flaws below curved surfaces. p. 81-93. In D. O. Thompson and D. E. Chimenti (ed.) Review of progress in quantitative NDE. Vol. 3A. Plenum Press, New York.

Elsley, R. K., K. W. Fertig, J. M. Richardson, and F. Cohen-Tenoudji. 1985. Statistical approach to the automation of flaw detection. p. 19-26. In D. O. Thompson and D. E. Chimenti (ed.) Review of progress in quantitative NDE. Vol. 4A. Plenum Press, New York.

Eshelby, J. D. 1957. The determination of the elastic field of an ellipsoidal inclusion, and related problems. Proc. R. Soc. London A 241(2):376-396.

Fertig, K. W., and J. M. Richardson. 1980. Inverse scattering at low and intermediate frequencies. Proceedings of the DARPA/AF Review of progress in quantitative NDE. Technical Report ARWAL-TR-80-4078 (Air Force Wright Aeronautical Laboratories, Dayton, OH, 1980) 528-540.

Fertig, K. W., and J. M. Richardson. 1983. Computer simulation of probability of detection. p. 147-169. In D. O. Thompson and D. E. Chimenti (ed.) Review of progress in quantitative NDE. Vol. 2A. Plenum Press, New York.

Fertig, K. W., J. M. Richardson, and R. K. Elsley. 1985. Statistical flaw detection in a scanning mode. p. 27-35. In D. O. Thompson and D. E. Chimenti (ed.) Review of progress in quantitative NDE. Vol. 4A. Plenum Press, New York.

Fitting, D. W., and L. Adler. 1981. Ultrasonic spectral analysis for nondestructive evalutation. Plenum Press, New York.

Frazier, K. 1983. Finding the fatal flaw. Mosaic Sept./Oct. 28-36.

Frederick, J. R., and J. A. Seydel. 1973. Improved discontinuity detection using computer-aided ultrasonic pulse-echo techniques. Welding Research Council Bulletin 185:1-23.

Furgason, E. S., R. E. Twyman, and V. L. Newhouse. 1978. Deconvolution processing for flaw signatures. Proceedings of the DARPA/AF Review of progress in quantitative NDE. Technical Report ARML-TR-78-55 (Air Force Wright Aeronautical Laboratories, Dayton, OH, 1978) 312-318.

Gautesen, A. K., J. D. Achenbach, and H. McMaken. 1978. Surface-wave rays in elastodynamic diffraction by cracks. J. Acoust. Soc. Amer. 63:1824-1831.

Goebbels, K. 1980. Structure analysis by scattered ultrasonic radiation. p. 87-157. In R. S. Sharpe (ed.) Research techniques in nondestructive testing. Vol. 4. Academic Press, New York.

Goodman, N. R. 1963. Statistical analysis based on certain multivariate complex Gaussian distribution. Ann. Math. Statistics 34:152-177.

Gray, T. A. 1982. Experimental procedure and signal processing steps for implementation of the 1-D inverse Born algorithm. Internal communication. Applied NDE Programs, Ames Laboratory, Iowa State University, Ames, IA.

Gray, T. A. 1988. Internal communication. Applied NDE Programs, Ames Laboratory, Iowa State University, Ames, IA.

Gubernatis, J. E., E. Domany, and J. A. Krumhansl. 1977. Formal aspects of the scattering of ultrasound by flaws in elastic materials. J. Appl. Phys. 48:2804-2811.

Gubernatis, J. E., and E. Domany. 1983. Effects of microstructure on the speed and attenuation of elastic waves: formal theory and simple approximations. p. 833-848. In D. O. Thompson and D. E. Chimenti (ed.) Review of progress in quantitative NDE. Vol. 2A. Plenum Press, New York.

Gubernatis, J. E. 1979. Long-wave approximations for the scattering of elastic waves from flaws with applications fo ellipsoidal voids and inclusions. J. Appl. Phys. 50(6):4046-4058.

Hahn, G. J., and S. S. Shapiro. 1967. Statistical models in engineering. Wiley, New York.

Harris, J. A., Jr. 1987. Engine component retirement for cause. Technical Report AFWAL-TR-87-4069 (Air Force Wright Aeronautical Laboratories, Dayton, OH, 1987).

Hatch, T. 1933. Determination of "average particle size" from the screen-analysis of non-uniform particlate substances. Jour. Franklin Inst. 11:27-37.

Hatch, T., and S. P. Choate. 1929. Statistical description of the size properties of non-uniform particulate substances. Jour. Franklin Inst. 3:369-387.

Haugen, E. B. 1968. Probabilistic approaches to design. Wiley, New York.

Haugen, E. B. 1980. Probabilistic mechanical design. Wiley, New York.

Hille, E. 1959. Analytic function theory. Blaisdell Publishing Company, New York.

Hsu, D. K., J. H. Rose, and D. O. Thompson. 1984. Reconstruction of inclusions in solids using ultrasonic Born inversion. J. Appl. Phys. 55(1):162-168.

Hsu, D. K., and D. O. Thompson. 1988. A novel fabrication technique for prescribed interior cracks in a metal. p. 1541-1548. In D. O. Thompson and D. E. Chimenti (ed.) Review of progress in quantitative NDE. Vol. 7B. Plenum Press, New York.

Hsu, D. K., D. O. Thompson, and R. B. Thompson. 1986. Evaluation of porosity in aluminum castings by single-sided access ultrasonic backscatter. p. 1633-1642. In D. O. Thompson and D. E. Chimenti (ed.) Review of progress in quantitative NDE. Vol. 5B. Plenum Press, New York.

Hsu, D. K., D. O. Thompson, and S. J. Wormley. 1987. Reliability of reconstruction or arbitrarily oriented flaws using multiview transducers. IEEE Transactions on Ultrasonics, Ferroelectrics, and Frequency Control UFFC-34(5):508-514.

Hsu, D. K., and K. M. Uhl. 1987. A morphological study of porosity defects in graphite-epoxy composties. p. 1175-1184. In D. O. Thompson and D. E. Chimenti (ed.) Review of progress in quantitative NDE. Vol. 6B. Plenum Press, New York.

Kennedy, W. J., and J. E. Gentle. 1980. Statistical computing. Marcel Dekker, New York.

Kino, G. S. 1987. Acoustic waves: devices, imaging, and analog signal processing. Prentice-Hall, Englewood Cliffs, New Jersey.

Kogan, V. G., D. K. Hsu, and J. H. Rose. 1985. Characterization of flaws using the zeroes of the real and imaginary parts of the ultrasonic scattering amplitude. Journal of Nondestructive Evaluation 5(2):57-68.

Kogan, V. G., and J. H. Rose. 1985. Limited aperture effects on ultrasonic image reconstruction. J. Acoust. Soc. Am. 77(4):1342-1351.

Koo, L. S. 1987. Ultrasonic flaw classification: an approach using modeling, signal processing, and adaptive learning. Doctoral Dissertation. Iowa State University, Ames, IA.

Kottler, F. 1950. The distribution of particle sizes. Jour. Franklin Instr. 19:339-356.

Kolsky, H. 1963. Stress waves in solids. Dover, New York.

Krautkramer, J., and H. Krautkramer. 1977. Ultrasonic testing of materials. Springer-Verlag, New York.

Lakhtakia, A., V. V. Varadan, and V. K. Varadan. 1985. Scattering of ultrasonic waves by oblate spheroidal voids of high aspect ratios. J. Appl. Phys. 58:4525-4530.

Larson, H. J. 1974. Introduction to probability theory and statistical inference. Wiley, New York.

Lee, D. A. 1981. Scatterer sizing from elastodynamic backscattering using splines. p. 1253-1257 In W. G. Vogt and M. H. Mickle (ed.) Proceedings of the 12th Annual Pittsburgh conference on modeling and simulation. Vol. 12. No. 4. Instrument Society of America, Research Triangle Park, North Carolina.

Lee, D. A., R. L. Crane, and T. J. Moran. 1984. A practical method for viewing resolution-noise-bandwidth trade-offs in NDE data reductions. p. 907-915. In D. O. Thompson and D. E. Chimenti (ed.) Review of progress in quantitative NDE. Vol. 3. Plenum Press, New York.

Marsh, K. A., J. M. Richardson, R. C. Addison, and R. K. Elsley. 1983. The automation of the Born inversion for ultrasonic flaw sizing. p. 975-987. In D. O. Thompson and D. E. Chimenti (ed.) Review of progress in quantitative NDE. Vol. 2. Plenum Press, New York.

Mason, W. P. 1968. Physical acoustics. Academic Press, New York.

Mason, W. P., H. J. McSkimin. 1947. Attenuation and scattering of high frequency sound waves in metals and glasses. J. Acoust. Soc. Am. 19(3):464-473.

Mendel, J. M. 1983. Optimal seismic deconvolution an estimation-based approach. Academic Press, New York.

Mix, D. F. 1969. Random signal processing. Addison-Wesley, Reading, Massachusetts.

Murakami, Y., B. T. Khuri-Yakub, G. D. Kino, J. M. Richardson, and S. G. Evans. 1978. An application of Wiener filtering to nondestructive evaluation. Appl. Phys. Lett. 33(8):685-687.

Neal, S., and D. O. Thompson. 1986. An examination of the application of Wiener filtering to ultrasonic scattering amplitude estimation. p. 737-745. In D. O. Thompson and D. E. Chimenti (ed.) Review of progress in quantitative NDE. Vol. 5A. Plenum Press, New York.

Neal, S., and D. O. Thompson. 1987. An *a priori* knowledge based Wiener filtering approach to ultrasonic scattering amplitude estimation. p. 807-813. In D. O. Thompson and D. E. Chimenti (ed.) Review of progress in quantitative NDE. Vol. 6A. Plenum Press, New York.

Neal, S. P., and D. O. Thompson. 1988. The effects of prior flaw information on Wiener filter based ultrasonic flaw scattering amplitude estimation. p. 857-864. In D. O. Thompson and D. E. Chimenti (ed.) Review of progress in quantitative NDE. Vol. 7A. Plenum Press, New York.

Oppenheim, A. V., and R. W. Schafer. 1975. Digital signal processing. Prentice-Hall, Englewood Cliffs, New Jersey.

Opsal, J. L., and W. M. Visscher. 1985. Theory of elastic wave scattering: applications of the method of optimal truncation. J. Appl. Phys. 58(3):1102-1115.

Papadakis, E. P. 1968. Ultrasonic attenuation caused by scattering in polycrystalline media. Charter 15. In Warren P. Mason (ed.) Physical acoustics, principles and methods. Vol. 4B. Academic Press, New York.

Papoulis, A. 1965. Probability, random variables, and stochastic processes. McGraw-Hill, New York.

Perry, M. 1985. Unpublished presentation made at Ames Lab July 1, 1985. M. Perry is the NDT laboratory manager at Rolls-Royce Limited, Bristol, England.

Phillips, D. 1962. A technique for the numerical solution of certain integral equations of the first kind. J. Assoc. Comput. Mach. 9:97-109.

Poe, G. D., and J. L. Opsal. 1982. Application of parameter estimation/system identification to quantitative ultrasonic NDE. p. 213-217. In D. O. Thompson and D. E. Chimenti (ed.) Review of progress in quantitative NDE. Vol. 1. Plenum Press, New York.

Rehbein, D. K., D. K. Hsu, R. B. Thompson, and T. A. Jones. 1987. Nondestructive evaluation of tubing closure welds. p. 157-162. In R. W. Siegel, J. R. Weertman, and R. Sinclair (ed.) Materials research society symposia proceedings (Characterization of Defects in Materials). Vol 82. Material Research Society, Pittsburgh.

Richardson, J. M. 1978. The inverse problem in elastic wave scattering at long wavelength. p. 759-766. In B. R. McAvoy (ed.) Ultrasonic symposium proceedings. IEEE, New York.

Richardson, J. M. 1980. Deterministic and probabilistic inversion at long wavelengths. Proceedings of the DARPA/AF Review of progress in quantitative NDE. Technical Report ARWAL-TR-81-4078 (La Jolla, CA, 1979) 514-519.

Richardson, J. M. 1984. Scattering of elastic waves from symmetric inhomogeneities at low frequencies. Wave Motion 6(4):325-336.

Richardson, J. M., and R. K. Elsley. 1979. Extraction of low-frequency properties from scattering measurements. p. 336-341. In J. deKlerk and B. R. McAvoy (ed.) Ultrasonic symposium proceedings. IEEE, New York.

Richardson, J. M., and R. K. Elsley. 1980. Semi-adaptive approach to the extraction of low-frequency properties from scattering measurements. p. 847-851. In B. R. McAvoy (ed.) Ultrasonic symposium proceedings. Vol. 2. IEEE, New York.

Richardson, J. M., and J. C. Gysbers. 1977. Application of estimation theory to image improvement. p. 212-218. In B. R. McAvoy (ed.) Ultrasonic symposium proceedings. IEEE, New York.

Rose, J. H. 1984. Elastic wave inverse scattering in non-destructive evaluation. Internal communication. Applied NDE Programs, Ames Laboratory, Iowa State University, Ames, IA.

Rose, J. H. 1985. Ultrasonic characterization of porosity: theory. p. 909-917. In D. O. Thompson and D. E. Chimenti (ed.) Review of progress in quantitative NDE. Vol. 4B. Plenum Press, New York.

Rose, J. H. 1988. Internal communication. Applied NDE Programs, Ames Laboratory, Iowa State University, Ames, IA.

Rose, J. H., and J. A. Krumhansl. 1979. Determination of flaw characteristics from ultrasonic scattering data. J. Appl. Phys. 50:2951-2952.

Rose, J. H., and J. M. Richardson. 1982. Time domain Born approximation. Journal of Nondestructive Evaluation 3(1):45-53.

Rose, J. H., R. K. Elsley, B. Tittmann, V. V. Varadan, and V. K. Varadan. 1980. Inversion of ultrasonic scattering data. p. 605-614. In V. V. Varadan and V. K. Varadan (ed.) Acoustic, electromagnetic, and elastic wave scattering - focus on the T-Matrix approach. Pergamon Press, New York.

Rose, J. H., T. A. Gray, R. B. Thompson, and J. L. Opsal. 1983. Progress on ultrasonic flaw sizing in turbine rotor components: bore and web geometries. p. 1065-1096. In D. O. Thompson and D. E. Chimenti (ed.) Review of progress in quantitative NDE. Vol. 2B. Plenum Press, New York.

Saff, E. B., and A. D. Snider. 1976. Fundamentals of complex variable analysis for mathematics, science, and engineering. Prentice-Hall, Englewood Cliffs, New Jersey.

Shapiro, S. S. 1980. How to test normality and other distributional assumptions. American Society for Quality Control, Milwaukee.

Stanke, F. E. 1983. Unified theory and measurements of elastic waves in polycrystalline materials. Stanford Univ., Edward L. Ginzton Laboratory Rep. No. 3642.

Stanke, F. E., and G. S. Kino. 1984. A unified theory for elastic wave propagation in polycrystalline materials. J. Acoust. Soc. Amer. 75:665-681.

Teitel, S. 1978. Determination of crack characteristics from the quasistatic approximation for the scattering of elastic waves. J. Appl. Phys. 49(12):5763-5767.

Thompson, D. O., S. J. Wormley, J. H. Rose, and R. B. Thompson. 1983a. Elastic wave scattering from multiple voids (porosity). p. 867-882. In D. O. Thompson and D. E. Chimenti (ed.) Review of progress in quantitative NDE. Vol. 2A. Plenum Press, New York.

Thompson, D. O., S. J. Wormley, J. H. Rose, and R. B. Thompson. 1983b. NDE technique for detection and characterization of porosity. p. 287-303 In P. Holler (ed.) New procedures in nondestructive testing. Springer-Verlag, New York.

Thompson, D. O., S. J. Wormley, and D. K. Hsu. 1986. Apparatus and technique for reconstruction of flaws using model-based elastic wave inverse ultrasonic scattering. Rev. Sci. Instrum. 57(12):3089-3098.

Thompson, R. B. 1983. Quantitative ultrasonic nondestructive evaluation methodes. J. Appl. Mech. 50(4b):1191-1201.

Thompson, R. B. 1985. Status of implementation of the inverse Born sizing algorithm. p. 611-621. In D. O. Thompson and D. E. Chimenti (ed.) Review of progress in quantitative NDE. Vol. 4. Plenum Press, New York.

Thompson, R. B., and T. A. Gray. 1982. Range of applicability of inversion algorithms. p. 233-249. In D. O. Thompson and D. E. Chimenti (ed.) Review of progress in quantitative NDE. Vol. 1. Plenum Press, New York.

Thompson, R. B., and T. A. Gray. 1983. A model relating ultrasonic scattering measurements through liquid-solid interfaces to unbounded medium scattering amplitudes. J. Acoust. Soc. Am. 74(4):1279-1290.

Thompson, R. B., and D. O. Thompson. 1985a. New techniques for quantitative NDE. p. 33-51. In O. Buck and S. M. Wolf (ed.) Nondestructive evaluation: microstructural characterization and reliability strategies symposium proceedings. Pittsburgh, Pennsylvania, October 5-9, 1980. The Metallurgical Society of AIME, Warrendale, Pennsylvania.

Thompson, R. B., and D. O. Thompson. 1985b. Ultrasonic nondestructive evaluation. Proceedings of the IEEE 73(12):1716-1755.

Tikhonov, A. N., and V. Y. Arsenin. 1977. Solutions of ill-posed problems. Wiley, New York.

Tittmann, B. R., and D. O. Thompson. 1977. Approach to a self-consistent calibration procedure of an ultrasonic system. Mater. Eval. 35(4):73-108. (Research Supplement edited by D. O. Thompson).

Tittmann, B. R., and L. A. Ahlberg. 1983. Attenuation and grain noise parameters in Ni-base alloys. p. 129-145. In D. O. Thompson and D. E. Chimenti (ed.) Review of progress in quantitative NDE. Vol. 2A. Plenum Press, New York.

Tittmann, B. R., D. O. Thompson, and R. B. Thompson. 1977. Standards for quantitative nondestructive evaluation. p. 295-311. H. Berger, Nondestructive Testing Standards-A Review. Rep. ASTM STP 624. Amer. Soc. Testing Mater., Philadelphia.

Tittmann, B. R., L. A. Ahlberg, and K. W. Fertig. 1983. Ultrasonic microstructural noise parameters in a powder metal alloy. p. 57-64. In D. O. Thompson and D. E. Chimenti (ed.) Review of progress in quantitative NDE. Vol. 2A. Plenum Press, New York.

Twomey, S. 1965. The application of numerical filtering to the solution of integral equations encountered in indirect sensing measurements. Jour. Franklin Inst. 279:95-109.

Varadan, V. V. 1978. Scattering matrix for elastic waves. II. Application to elastic cylinders. J. Acoust. Soc. Am. 63(4):1014-1024.

Varadan, V. V. 1979. Elastic wave scattering. p. 33-59. In V. V. Varadan and V. K. Varadan (ed.) Acoustic, electromagnetic, and elastic wave scattering - focus on the T-Matrix approach. Pergamon Press, New York.

Varadan, V. V., and V. K. Varadan. 1979. Scattering matrix for elastic waves. II. Application. J. Acoust. Soc. Amer. 65(4):896-905.

Visscher, W. M. 1981. Calculation of the scattering of elastic waves from a penny-shaped crack by the method of optimal truncation. Wave Motion. 3(1):49-69.

Whalen, A. D. 1971. Detection of signals in noise. Academic Press, New York.

White, R. M. 1958. Elastic wave scattering at a cylindrical discontinuity in a solid. J. Acoust. Soc. Am. 30(8):771-785.

Wormley, S. J., D. K. Hsu, and D. O. Thompson. 1986. The effects of flaw orientation and finite aperture on model based reconst ruction using multiprobe transducers. p. 529-539. In D. O. Thompson and D. E. Chimenti (ed.) Review of progress in quantitative NDE. Vol. 5A. Plenum Press, New York.

Wormley, S. J., D. O. Thompson, and K. M. Lakin. 1983. A computational tool for the design of ultrasonic systems. p. 1473-1485. In D. O. Thompson and D. E. Chimenti (ed.) Review of progress in quantitative NDE. Vol. 2B. Plenum Press, New York.

Ying, C. F., and R. Truell. 1956. Scattering of a plane longitudinal wave by a spherical obstacle in an isotropically elastic solid. J. Appl. Phys. 27(9):1086-1097.

ACKNOWLEDGMENTS

Don Thompson suggested that I work on this fruitful project. I am grateful for the support he has provided. I am thankful to everyone in the NDE group for their help and friendship. I am especially thankful to Tim Gray, Jim Rose, David Hsu, and Bruce Thompson and to Sam Wormley for his ever accommodating approach and for his help in the lab. My association with Don and the rest of the group has been a valuable experience which will aid me throughout my career. I would also like to acknowledge the support of the Engineering Science and Mechanics Department.

I want to thank Grover Brown for his consultation. Many thanks to Leo Peters and Bill Riley for their support and guidance over the years. A very special thanks to Joe Tevis for his friendship, for his sense of humor, and for sharing his family.

As in anything I do, I am most thankful for the friendship and love of my wife and the rest of our family.